Growth and Characterization of Ga(As,N) and (In,Ga)(As,N)

DISSERTATION

zur Erlangung des akademischen Grades
doctor rerum naturalium
(Dr. rer. nat.)
im Fach Physik

eingereicht an der
Mathematisch-Naturwissenschaftlichen Fakultät I
der Humboldt-Universität zu Berlin

von
Herrn Dipl.-Phys. Gregor Mußler
geboren am 18. Oktober 1974 in Berlin

Präsident der Humboldt-Universität zu Berlin:
Prof. Dr. J. Mlynek

Dekan der Mathematisch-Naturwissenschaftlichen Fakultät I:
Prof. T. Buckhout, PhD

Gutachter:

1. Prof. Dr. Klaus H. Ploog
2. Prof. Dr. Thomas Elsässer
3. Prof. Dr. Enrique Calleja

eingereicht am:	08. November 2004
Tag der mündlichen Prüfung:	09. Februar 2005

Abbreviations

AFM	Atomic Force Microscopy
BAC	Band Anticrossing Model
BEP	Beam Equivalent Pressure
CM	Center of Mass
cw-PL	Continuous Wave Photoluminescence
FWHM	Full Width at Half Maximum
LVM	Local Vibrational Mode
MBE	Molecular Beam Epitaxy
MOCVD	Metal-Organic Chemical Vapor Deposition
μPL	Micro Photoluminescence
MQW	Multi Quantum Well
PL	Photoluminescence
QW	Quantum Well
rf	Radio Frequency
RHEED	Reflection High-Energy Electron Diffraction
RMS	Root Mean Square
RSM	Reciprocal Space Mapping
RT	Room Temperature
RTA	Rapid Thermal Annealing
SIMS	Secondary Ion Mass Spectrometry
SML	Strain Mediating Layer
SNOM	Scanning Near-Field Optical Microscopy
SQW	Single Quantum Well
TEM	Transmission Electron Microscopy
TR-PL	Time-Resolved Photoluminescence
UHV	Ultra High Vacuum
VCSEL	Vertical Cavity Surface Emitting Laser
XRD	X-Ray Diffraction

Parts of this work have already been published:

G. Mussler, L. Däweritz, and K. H. Ploog, *Thickness dependent roughening of Ga(As,N)/ GaAs MQW structures with high nitrogen content*, J. Cryst. Growth **251**, 399 (2003).

G. Mussler, L. Däweritz, K. H. Ploog, J. W. Tomm, and V. Talalaev, *Optimized annealing conditions identified by analysis of radiative recombination in dilute Ga(As,N)*, Appl. Phys. Lett. **83**, 1343 (2003).

G. Mussler, J.-M. Chauveau, A. Trampert, M. Ramsteiner, L. Däweritz, and K. H. Ploog, *Nitrogen-dependent optimum annealing temperature of Ga(As,N)*, J. Cryst. Growth **267**, 60 (2004).

Conference contributions:

Nitrogen-dependent optimum annealing temperature of Ga(As,N), German MBE Workshop, Munich, October 16 – 17, 2003.

Optimized annealing conditions identified by analysis of radiative recombination in dilute Ga(As,N), International Workshop on GaAs based lasers for the 1.3 to 1.5 μm wavelength range, Wroclaw, April 24 – 26, 2003.

Investigations of compositional fluctuations in dilute Ga(As,N) by means of micro photoluminescence, German MBE Workshop, Freiburg im Breisgau, October 21 – 22, 2002.

Thickness dependent roughening of Ga(As,N)/ GaAs MQW structures with high nitrogen content, International Conference on Molecular Beam Epitaxy, San Francisco, September 15 – 20, 2002.

Co-author contributions:

H. Ch. Alt, Y. V. Gomeniuk, and G. Mussler, *Influence of indium-nitrogen interactions on the local mode frequency of nitrogen in GaAs-based dilute nitrides*, to be published in Proceedings of the 27th Int. Conf. on the Phys. of Semicond. (ICPS27).

S. Sinning, T. Dekorsy, M. Helm, G. Mussler, L. Däweritz, and K. H. Ploog, *Reduced sub-picosecond electron relaxation in* GaN_xAs_{1-x}, submitted to Appl. Phys. Lett.

D. S. Jiang, L. F. Bian, X. G. Liang, Y. H. Qu, G. Mussler, M. Ramsteiner, and K. H. Ploog, *Influence of thermal treatment on compositional fluctuations and clustering in GaNAs epilayers*, submitted to J. Cryst. Growth.

Zusammenfassung

Das Thema dieser Dissertation ist das MBE-Wachstum und die Charakterisierung von Ga(As,N) und (In,Ga)(As,N). Die Arbeit beginnt mit der Optimierung des Wachstums von Ga(As,N) bezüglich verschiedener Wachstumsparameter. Aufgrund der hohen Mischbarkeitslücke von GaAs und GaN ist die Substrattemperatur entscheidend für das Wachstum von Ga(As,N). Das heißt, der Einbau von Stickstoff in GaAs bei hohen Substrattemperaturen führt zu einer strukturellen Degradation der Ga(As,N)-Proben. Niedrige Substrattemperaturen sind deshalb notwendig, um den gleichmäßigen Einbau von Stickstoff in GaAs zu gewährleisten. Die Parameter der Plasmaquelle sind entscheidend für die optischen Eigenschaften von Ga(As,N). Niedrige Leistungen der Plasmaquelle und geringe Stickstoff-Flüsse erhöhen die Photolumineszenz-Intensität und verringern die Halbwertsbreite der Photolumineszenz-Spektren.
Ein weiterer Schwerpunkt dieser Arbeit ist die Untersuchung des Übergangs von glatten zu rauen Grenz- und Oberflächen von Ga(As,N)-Multiquantentöpfen (MQWs) in Abhängigkeit von der Stickstoffkonzentration und der Quantentopf-Dicke. Eine strukturelle Degradation erfolgt, wenn eine bestimmte Quantentopf-Dicke überschritten wird. Diese strukturelle Degradation manifestiert sich in einem Aufrauen der Oberflächen und der Grenzflächen der MQWs. Es wird gezeigt, daß in rauen Ga(As,N)-MQWs keine Versetzungen in der Wachstumsebene existieren.
Aufgrund der niedrigen Substrattemperaturen und der Benutzung einer Stickstoff-Plasmaquelle sind Punktdefekte im Ga(As,N)-Materialsystem unvermeidlich. Diese Punktdefekte haben einen schädlichen Einfluß auf optische Eigenschaften der Ga(As,N)-Proben. Eine thermische Behandlung verringert die Konzentration dieser Punktdefekte. Dies geht mit einer Steigerung der Photolumineszenz-Intensität einher. Punktdefekte sind zum Beispiel Stickstoff-Dimere, die sich in Gallium- oder Arsen-Vakanzen einbauen. Darüberhinaus bewirkt das Anlegen eines externen Magnetfeldes während des Wachstums eine Verbesserung optischer Eigenschaften der Ga(As,N)-Proben. Diese Beobachtung kann man durch Ionen erklären, die von der Plasmaquelle generiert werden. Es wird außerdem gezeigt, daß die thermische Behandlung das Konzentrationsprofil von Stickstoff selbst bei hohen Temperaturen weitgehend unverändert lässt. Allerdings bewirkt eine thermische Behandlung bei hohen Temperaturen eine strukturelle Degradation im Ga(As,N)-Materialsystem. Dies verursacht eine Abnahme der Photolumineszenz-Intensität. Es wird gezeigt, daß die Temperatur der thermischen Behandlung, die die höchste Photolumineszenz-Ausbeute erzielt, von der Stickstoffkonzentration abhängig ist.
Die strahlende Rekombination in verdünntem Ga(As,N) wird in Abhängigkeit von der Temperatur der thermischen Behandlung untersucht. Es zeigt sich, daß Exzitonen entweder in Potentialfluktuationen oder in Defekten räumlich lokalisiert sind. Eine Erhöhung der Anregungsdichte und/oder eine Erhöhung der Temperatur bewirkt einen Übergang von lokalisierten zu delokalisierten Exzitonen. Mit Zunahme der Temperatur der thermischen Behandlung verschwindet der Einfluß der Defekte. Dennoch sind Exzitonen in ausgeheilten Ga(As,N)-Proben in Potentialfluktuationen gefangen. Eine Abschätzung der Konzentration dieser Potentialfluktuationen wird durchgeführt.
Bezüglich des Wachstums von (In,Ga)(As,N) sind niedrige Substrattemperaturen aufgrund der Mischbarkeitslücke von (In,Ga)As und (In,Ga)N ebenfalls entscheidend für die strukturelle Qualität von (In,Ga)(As,N). Auch im quaternären Materialsystem ist eine thermische Behandlung essentiell für die Verbesserung optischer Eigenschaften. Es wird außerdem gezeigt, daß die thermische Behandlung von (In,Ga)As eine Indiumdiffusion verursacht, die durch den Einbau von Stickstoff gestoppt wird. Diese Beobachtung wird mit dem Einbau von Stickstoff in Gallium-Vakanzen erklärt.
(In,Ga)As kantenemittierende Laser mit Indiumkonzentrationen zwischen 13 und 38% werden charakterisiert. Die Wellenlänge der Emission verschiebt sich von 939 zu 1147 nm mit Zunahme der Indiumkonzentration. Hohe Indiumkonzentrationen verursachen aufgrund der hohen Verspannung eine strukturelle Degradation, die sich in einer Zunahme der Schwellstromdichte dieser Laser widerspiegelt. Die Charakterisierung von (In,Ga)(As,N) kantenemitterenden Lasern mit 35% Indium und Stickstoffkonzentrationen zwischen 1 und 3% zeigt eine Verschiebung der Emissionswellenlänge von 1250 nach 1366 nm. Mit dem Einbau von Stickstoff ist ein Anstieg der Schwellstromdichte und ein Abfall der Emissionsleistung verbunden.

Abstract

This dissertation deals with the MBE growth and characterization of Ga(As,N) and (In,Ga)(As,N). The work commences with the optimization of the Ga(As,N) growth. Owing to a large miscibility gap of GaN in GaAs, the substrate temperature is the most crucial growth parameter. We will show that growing Ga(As,N) at high substrate temperatures leads to a roughening of surfaces and interfaces. Low substrate temperatures are therefore mandatory to warrant the morphological quality of Ga(As,N). The parameters of the nitrogen plasma source have an important impact upon the optical properties of Ga(As,N). We will demonstrate that a lowering of the plasma source power and nitrogen flow yields an improvement of optical properties, namely an increase of the photoluminescence intensity and a decrease of the halfwidths of the photoluminescence spectra.

Another topic of this work will be the investigation of surface and interface roughening of Ga(As,N) with respect to the nitrogen concentration and the quantum well thickness. Experimental results will be presented that show a clear transition from smooth to rough surfaces and interfaces if a certain Ga(As,N) roughening thickness is exceeded. We will demonstrate that rough Ga(As,N) samples show regions of higher nitrogen concentrations within the Ga(As,N) quantum wells, whereas no misfit dislocations are detected.

Owing to low substrate temperatures and the use of a nitrogen plasma source, point defects are inevitable in the Ga(As,N) material system. A thermal treatment of Ga(As,N) reduces the concentration of these point defects. This leads to a substantial improvement of optical properties. We will show that nitrogen split interstitials that incorporate into gallium and arsenic vacancies may be attributed to these point defects. Growing Ga(As,N) in an external magnetic field also causes an improvement of optical properties. This observation will be elucidated by the existence of ions generated by the nitrogen plasma source. We will also present experimental evidence that a thermal treatment of Ga(As,N) leaves the nitrogen concentration profile almost unchanged. A thermal treatment of Ga(As,N) at high temperatures results in a creation of extended defects which are detrimental to optical properties. We will show that the temperature of the thermal treatment that yields the highest photoluminescence intensity is nitrogen concentration-dependent.

Investigations on radiative recombination in Ga(As,N) will be performed. We will provide experimental evidence of localized excitons, either trapped in potential fluctuations or defects. An increase of the excitation density and/or the temperature causes a transition from localized to delocalized excitons. A thermal treatment of Ga(As,N) reduces the concentration of these defects. Still, for healed out Ga(As,N) samples, excitons are localized in potential fluctuations. An estimate of the potential fluctuation concentration in dilute Ga(As,N) will be drawn.

We will demonstrate that the growth of (In,Ga)(As,N) is similar with respect to Ga(As,N). Again, one has to face a high miscibility gap of (In,Ga)N in (In,Ga)As. Consequently, low substrate temperatures are mandatory to ensure smooth surfaces and interfaces of the quaternary material system. A thermal treatment of (In,Ga)(As,N) is also beneficial for improving optical properties. We will show that a thermal treatment of (In,Ga)As results in an indium interdiffusion that is suppressed by the incorporation of nitrogen. We will explain this observation with an incorporation of nitrogen into gallium vacancies.

(In,Ga)As edge emitting lasers with indium concentrations between 13 and 38% will be characterized. With an increase of the indium concentration, the emission wavelengths shift from 939 to 1147 nm. For high indium concentrations, there is a strain-induced structural degradation that is manifested by an increase of the threshold current density and a decrease of the slope efficiency. (In,Ga)(As,N) edge emitting lasers comprising 35% indium and nitrogen concentrations between 1 and 3% will be characterized. The emission wavelengths shift from 1250 to 1366 nm with higher nitrogen concentrations. Concomitantly, there is an increase of the threshold current density and a decrease of the output power.

Contents

Chapter 1

Introduction

The internet is becoming an increasingly versatile medium in our information society. More and more people are going online to conduct day-to-day activities, such as personal correspondence, e-commerce and money transfer, research and information-gathering, as well as job searches. With more and more people using the internet, the amount of data being transferred is growing rapidly. In order to deal with larger amounts of data, there has been a transition from copper cable to glass fibre because of distinct advantages. First, glass fibre provides a higher bandwidth, thus being more suitable for backbone networks. Second, light is not affected by electromagnetic interference induced by radio frequency. Third, copper media require amplifiers every hundred meters. Nowadays, the manufacturing process of glass fibre makes the conducting core pure enough to carry high speed signals for tens of kilometers before a repeater is required. Fourth, there are no electrical components, thus there is no danger of electrical shock and power consumption is minimized.

However, using glass fibre for data communication, one is restricted to a wavelength range between 1.3 – 1.55 μm due to optical fibre losses. To generate emission at these wavelengths, semiconductor infrared lasers are being used, mainly based on (In,Ga)(As,P)/InP. Recently, (In,Ga)(As,N)/GaAs has emerged as an alternative material system to accomplish infrared lasers. The key feature of (In,Ga)(As,N) is that the incorporation of nitrogen into GaAs and (In,Ga)As causes a tremendous band gap bowing leading to a strong reduction of the band gap [1, 2, 3]. One percent of nitrogen reduces the band gap by 150 meV. Thus, one can control the band gap in a range of 1.4 – 0.8 eV, suitable of long wavelength light emitting devices. Recently, successful operations of (In,Ga)(As,N)/GaAs-based laser diodes have been demonstrated [4, 5, 6, 7, 8]. As a matter of fact, even a commercial production of (In,Ga)(As,N)/GaAs laser diodes has already started.

There are several major advantages of using (In,Ga)(As,N)/GaAs for light emitting devices with respect to (In,Ga)(As,P)/InP. First, (In,Ga)(As,N)/GaAs-based devices are thermally more stable due to higher band alignment offsets. Second, the use of large-area GaAs wafers reduces the cost of light emitting devices since it offers the possibility of vertical cavity surface emitting lasers (VCSELs), based on the high refractive index contrast of GaAs/(Al,Ga)As. Unlike edge emitting lasers, VCSELs are grown by thousands on a single wafer with significant advantages in the areas of lower manufacturing, packaging, alignment, and testing costs, as well as lower power dissipation and higher reliability.

The growth of Ga(As,N) and (In,Ga)(As,N) on GaAs can be accomplished by two growth techniques, either metal-organic chemical vapor deposition (MOCVD) or molecular-beam epitaxy (MBE). In MOCVD, gases such as arsine or trimethylgallium react in the vicinity of the substrate; the growth rates are determined by controlling the gas flows. MBE growth is accomplished by the heating of source materials in effusion cells to create evaporated molecular or atomic beams in an ultrahigh vacuum (UHV) chamber. These molecular or atomic beams travel through the UHV chamber to finally impinge on a substrate. With both techniques, high quality (In,Ga)(As,N) material has been grown. Nevertheless, there are significant differences between MOCVD and MBE. One major drawback of MOCVD with respect to MBE is a nonlinear dependence of the GaAs growth rate and the nitrogen incorporation, thus making a control of the nitrogen concentration difficult[9]. Moreover, in case of MOCVD grown samples, there is higher concentration of impurities, such as hydrogen or carbon[10], which is detrimental to laser applications. Another shortcoming of MOCVD with respect to MBE is the high expense of dimethylhydrazine that is used as a metalorganic nitrogen compound. So far, the best device characteristics have been demonstrated for lasers grown by the MBE growth technique.

Even miniscule amounts of nitrogen alter the energy structure of the GaAs host matrix. Nitrogen concentrations of less than 0.001% show narrow recombination lines in the emission spectra with energies below the band gap by virtue of electronic levels of nitrogen pairs and/or clusters[11, 12, 13]. With a further increase of nitrogen (up to 0.1%), the band gap starts redshifting. When reaching the alloy regime (nitrogen concentration higher than 0.1%), the band gap resumes to redshift to energies below these nitrogen-induced levels, causing the sharp lines to disappear into a single broad emission line. In addition, a conceivable increase of the electron effective mass[14, 15] and a different temperature dependence of the band gap is observed[16, 17, 18].

Even though the commercial production of (In,Ga)(As,N)/GaAs-based laser diodes has just started, the ternary and the quaternary material system still pose quite a number of questions. The nature of defects that are associated with the incorporation of nitrogen into GaAs and (In,Ga)As is still contentious. Investigations are being made to explore the issue of potential fluctuations in Ga(As,N) and (In,Ga)(As,N), particularly concerning size and density. The matter of an increased effective mass with higher nitrogen concentration and the impact of a confinement on it is still under scrutiny. Great efforts are being made to survey the influence of an ex-situ thermal treatment concerning diffusion processes in Ga(As,N) and (In,Ga)(As,N). The roughening mechanisms of Ga(As,N) and (In,Ga)(As,N) as well as the lattice sites of nitrogen and indium in Ga(As,N) and (In,Ga)(As,N) before and after annealing are still being studied.

The aim of this work is to clarify a few of the aforementioned questions. In chapter 2, some aspects of semiconductor heterostructures are discussed that are beneficial to understand the following chapters. Chapter 3 deals with Ga(As,N) related issues, such as the MBE-growth of Ga(As,N), the roughening of this material system, the matter of rapid thermal annealing (RTA) to improve light emitting properties, the analysis of the nature of radiative recombination in Ga(As,N), and the investigation of nitrogen-induced potential fluctuations. Chapter 4 discusses details related to (In,Ga)(As,N), such as the optimization of the (In,Ga)(As,N) growth by MBE and RTA-induced diffusion processes in this material system. The findings of chapter 3 and 4 are subsequently used to develop (In,Ga)As and (In,Ga)(As,N) edge emitting lasers which is subject of chapter 5. Important questions, such as the optimum nitrogen and indium concentration to reach an emission wavelength of 1.3 μm, are discussed. Conclusions of this work and an outlook are given in chapter 6.

Chapter 2

Some Aspects of Semiconductor Heterostructures

In the following chapters, details about the growth and characterization of the Ga(As,N) and (In,Ga)(As,N) material system will be discussed. For the sake of comprehending these chapters, this chapter is dedicated to fundamental properties of semiconductor heterostructures, as well as details about the MBE growth technique.

2.1 Band Gap-Related Issues

The two most fundamental properties of a semiconductor for device applications are the band gap and the lattice constant. The band gap refers to the energy difference between the conduction band minimum and the valence band maximum. For semiconductors with a zinc-blende structure, the lattice constant is defined by the spatial extent of the face-centered cubic sub-lattices. Figure 2.1 depicts the band gaps and lattice constants of several elementary and binary semiconductors with a zinc-blende structure. The lines represent the band gaps and lattice constants of semiconductor alloys that comprise the pertinent semiconductor materials. Thus, by controlling the concentrations of the constituent semiconductors, one can tailor the band gap and the lattice constant of semiconductor alloys. Interestingly, for some semiconductor alloys, the band gap does not linearly depend upon the lattice constant (and thus upon the constituent semiconductor concentrations) but there is a so called band gap bowing. For example, the incorporation of nitrogen into GaAs reduces the band gap, even though GaN is a wide band gap material.

There are two competing models that explain the nitrogen-induced band gap reduction. The band anticrossing (BAC) model accounts for an interaction of a nitrogen induced level and the conduction band that causes a splitting of the conduction band into an E_+ and an E_- band[19, 20, 21, 22]. The band gap reduction is thus attributed to the E_- band. On the contrary, ab-initio calculations explain the band gap reduction with a symmetry breaking of the host crystal by the incorporation of nitrogen into GaAs[23, 24, 25, 26, 27]. There are advantages and drawbacks for each model. For example, ab-initio calculations are beneficial to determine the change of the energy structure of Ga(As,N) from impurity-like nitrogen concentration to heavily doped Ga(As,N). In these calculations, single nitrogen impurities, pairs, and clusters are taken

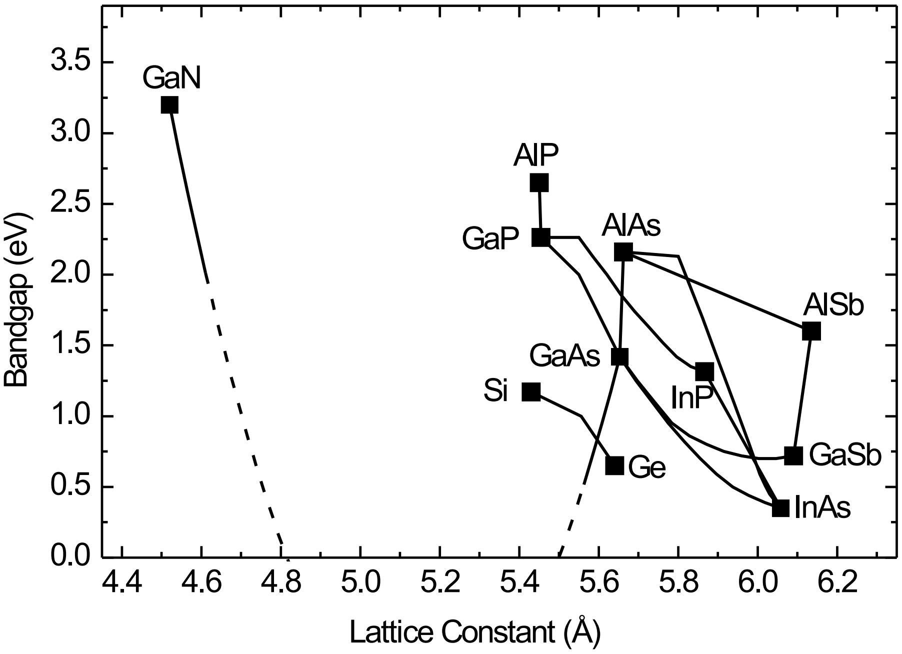

Figure 2.1: Lattice constants and band gaps of several elementary and binary semiconductors with a zinc-blende structure. The lines that connect different semiconductors denote the band gaps and lattice constants of the pertinent semiconductor alloys.

into account which are excluded from the BAC model. Moreover, ab-initio calculations do not require any fitting parameters to run the simulation, whereas the BAC model needs two fitting parameters to calculate the band gap reduction. On the other hand, the BAC model has several advantages with respect to ab-initio calculations. For example, this model is based upon analytical calculations that are facile to reproduce. Ab-initio calculations originate from supercell calculations that require huge computational efforts to simulate the band gap reduction. Moreover, ab-initio calculations determine the band gap reduction for fixed nitrogen concentrations only. The BAC model, on the contrary, yields an analytical equation. Thus, one can calculate the band gap reduction for any desired nitrogen concentration. Based on this analytical expression, one can also derive analytical equations that describe the nitrogen-induced increase of the effective electron mass[28, 14], as well as the different band gap temperature behavior of Ga(As,N) with respect to GaAs [16, 17].

According to the BAC model, the conduction band splitting into the E_+ and E_- band is determined through:

$$E_{\pm} = \frac{1}{2}\left(E_N + E_M \pm \sqrt{(E_N - E_M)^2 + 4V_{NM}^2}\right) \tag{2.1}$$

where E_N is the energy of the nitrogen-induced level and E_M stands for the conduction band edge of the host matrix (either GaAs or (In,Ga)As). The band gap of Ga(As,N) or (In,Ga)(As,N) is represented by the E_- band. V_{NM} denotes the interaction term between E_M and E_N. This interaction term is, on the other hand, nitrogen-concentration dependent: $V_{NM} = C_{NM}\sqrt{x}$. C_{NM} is a constant, whereas x represents the nitrogen concentration. The (experimentally determined) nitrogen-induced level E_N is located 1.65 eV above the valence band edge. C_{NM} amounts to 2.7 eV. The E_- band of Ga(As,N) derived from equation 2.1 is plotted in figure 3.8.

The reason of tailoring the band gap of semiconductors lies in the fact that the wavelength of radiative recombination is mainly determined by the band gap. To experimentally investigate radiative recombination, one can employ photoluminescence (PL) measurements. In PL experiments, a laser beam that is focused on the sample creates electrons in the conduction band and holes in the valence band. These electrons and holes undertake ultrafast intraband transitions to the conduction band edge and valence band edge, respectively, where they subsequently radiatively recombine under the emission of photons. In case of such band edge transition, the energy of these photons (from which the wavelength is deduced) equals the band gap. However, for determining the band gap from PL measurements, one has to act with caution, as defects in the band gap may falsify experimental results. Instead of band edge transitions, electrons and holes may drop into these defects where they radiatively recombine. Hence, the energy of the photons is not determined by the band gap but by the energy states of these defects. Still, if one warrants the absence of defects in the probed semiconductor, it is feasible to measure the band gap via PL. A way to remove defects in Ga(As,N) is RTA. This issue will be discussed in section 3.3. In semiconductor alloys, the band gap allows to determine the concentrations of the constituent semiconductors. In addition, the full width at half maximum (FWHM) value[1] of the PL spectrum represents the spatial uniformity of the band gap (and thus the spatial uniformity of the constituent semiconductor concentrations). An inhomogeneous spatial distribution of the constituent semiconductor concentrations results in an increase of the FWHM value. The area of the inhomogeneous spatial distribution is defined by the spatial extent of bound excitons. Excitons are interacting electron-hole pairs with a lateral extent of the exciton Bohr radius. In case of GaAs, it amounts to 11.8 nm. Hence, the FWHM values of PL spectra reveal information of spatial concentration inhomogeneities with a lateral extent of approximately 10 nm.

Spatial inhomogeneities regarding the concentration of the constituent semiconductors also change the nature of excitons. Spatial concentration inhomogeneities cause dips in the band alignment, so called potential fluctuations, in which excitons are trapped. If the lateral extent of these potential fluctuations is smaller or in the same range as the exciton Bohr radius, these excitons are spatially localized in all three dimensions by virtue of a confining potential. Apart from potential fluctuations, excitons may also be spatially localized by defects. Defects generate confining Coulomb potentials in which excitons are trapped.

Localized excitons have a substantially different behavior in comparison to delocalized excitons. Delocalized excitons may move freely within the semiconductor crystal, whereas localized excitons are trapped in confining potentials. Owing to these confining potentials, localized excitons may solely occupy discrete energy states. Thus, if the spatial resolution of the PL setup is sufficient to resolve a single or just a few localized excitons, ultranarrow spikes in the emission spectra are discernable. Micro photoluminescence (μPL) or scanning near-field optical microscopy (SNOM) setups have spatial

---

[1] The FWHM value refers to the spectral difference between PL data points with an intensity that amounts to 50% of the maximum value.

resolutions of 1 μm and 0.2 μm, respectively. These spatial resolutions are high enough to observe discrete energy states of localized excitons. μPL and SNOM results will be presented in section 3.4 and 3.5, respectively.

Another feature of localized excitons is the low spatial density of the confining potentials. Consequently, excitation density-dependent PL might reveal the nature of the probed excitons. These confining potentials may be easily saturated with excitons for higher excitation densities. Hence, with all confining potentials filled at low energies, confining potentials at higher energies are occupied. This leads to a PL blueshift. In contrast, one cannot observe this phenomenon for delocalized excitons. Experimental results of excitation density-dependent PL will be presented in section 3.4.

Apart from spatially-resolved PL and excitation density-dependent PL, time-resolved PL (TR-PL) is another experiment to distinguish between localized and delocalized excitons. Localized excitons show a long decay time, typically in the nanosecond range, whereas delocalized excitons in quantum wells (QWs) have short decay times in the picosecond range. Thus, a spectral dependence of the decay time with long decay times on the low-energy side and short decay times on the high-energy side serves as a signature of the existence of localized and delocalized excitons. To explain this phenomenon, one can argue of a reduced center of mass (CM) exciton wavefunction in case of localized excitons. Consequently, by employing Fermi's Golden Rule, one can find that the recombination probability is lower in case of localized excitons. The transition probability is inversely proportional to the decay time, thus, causing a higher decay time in case of localized excitons[29]. This phenomenon is even more pronounced in case of excitonic transfers from high-energy to low-energy localized states. Gourdon *et al.* [30] have developed a model in which an exponential decrease of the density of localized states for higher energies is assumed. By employing this model, the authors have derived an equation that explains the spectral dependence of the decay time. Experimental evidence of localized and delocalized excitons determined by means of TR-PL is provided in section 3.5.

As pointed out in the preceding paragraphs, the wavelength of radiative recombination in a semiconductor is mainly determined by the band gap. However, apart from the exciton binding energy, corrections need to be made in case of a strong carrier confinement. In semiconductor heterostructures, a strong carrier confinement is accomplished by thin QWs of a narrow band gap semiconductor surrounded by barriers of a wide band gap semiconductor. A strong carrier confinement causes an increase of the bound energy states of electrons and holes in the QWs. Thus, the emission wavelength is determined by the sum of the band gap and the confinement energy. For GaAs, the carrier confinement effect becomes eminent if the QW thickness is below 20 nm. To quantitatively determine the carrier confinement effect, one has to solve the Schrödinger equation for a particle in a QW[31]:

$$-\frac{\hbar^2}{2m^*}\frac{\partial^2\Psi(x)}{\partial x^2} + V(x)\Psi(x) = E\Psi(x) \tag{2.2}$$

where $\Psi(x)$ represents the wavefunction, $V(x)$ the potential, m^* the effective mass, and E the energy states of the particle. Assuming a quantum well of the thickness $2W$ and barrier heights V_0, the ground state energy of equation 2.2 is solved through:

$$\alpha \tan(W\alpha) = \beta \tag{2.3}$$

where $\alpha = (2m^* E/\hbar^2)^{1/2}$ and $\beta = (2m^* (V_0 - E) /\hbar^2)^{1/2}$. This transcendental equation has to be solved numerically to obtain the ground state energy. Qualitatively spoken, there is an increase of the ground state energy for smaller quantum well thicknesses.

Summary The two most important parameters of a semiconductor are the band gap and the lattice constant. In case of semiconductor alloys, one can tailor the band gap by controlling the concentration of the constituent semiconductors. In case of band edge transitions, the band gap can experimentally be determined by PL measurements. However, corrections need to be made in case of a strong carrier confinement. In addition, PL measurements provide information about the spatial concentration homogeneity and carrier localization.

2.2 Lattice-Mismatched Heterostructures

As pointed out in the last section, one can tailor the lattice constant of semiconductor alloys by controlling the concentrations of the constituents. To calculate the lattice constant of an unstrained semiconductor alloy, Vegard's law is usually employed. It states that the lattice constant of a semiconductor alloy is calculated by a linear interpolation between the lattice constants of the constituent semiconductors. For example, the lattice constant of Ga(As,N) is:

$$\begin{aligned} a_{Ga(As,N)} &= a_{GaAs} + (a_{GaN} - a_{GaAs}) \cdot x \\ a_{Ga(As,N)} &= 5.65325\ \text{Å} + (4.52\ \text{Å} - 5.65325\ \text{Å}) \cdot x \end{aligned} \tag{2.4}$$

where x stand for the nitrogen concentration. However, the validity of Vegard's law is contentious in case of Ga(As,N). Spruytte *et al.* [32, 33], report a deviation from Vegard's law leading to an underestimation of the nitrogen concentration from x-ray diffraction (XRD) measurements. On the other hand, Li *et al.* [34] state a deviation from Vegard's law that causes a overestimation of the nitrogen concentration derived from XRD. Apart from that, Uesugi *et al.* [35] claim no deviation from Vegard's law. Nonetheless, even though there might be slight deviations, Vegard's law provides a good estimate of the lattice constant of Ga(As,N).

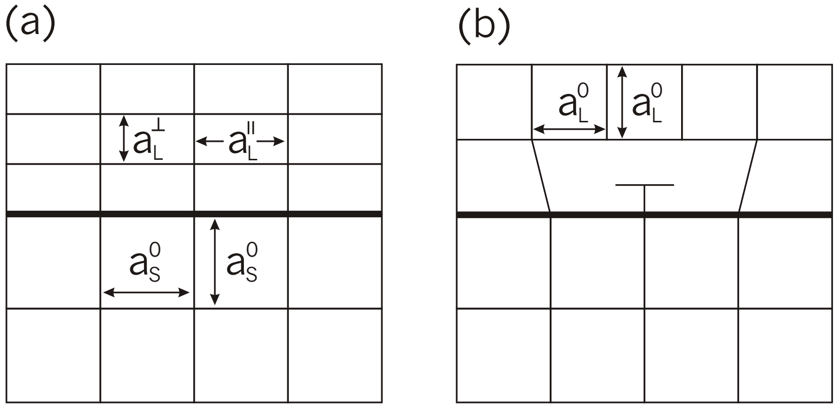

Figure 2.2: Fully strained (a) and fully relaxed (b) semiconductor layer with a smaller lattice constant than the substrate.

A semiconductor layer with a lattice constant a_L^0 that is deposited on a substrate with a lattice constant a_S^0 is either fully strained, partly relaxed, or fully relaxed. Figure 2.2 illustrates the two limiting cases of a fully strained (a) and a fully relaxed (b) semiconductor layer that has a smaller lattice constant than the substrate: $a_L^0 < a_S^0$. For fully strained semiconductors, one has to distinguish between two lattice constants: the in-plane and out-of-plane lattice constant. The in-plane lattice constant $a_L^{||}$ lies in the plane that is perpendicular to the growth direction, whereas the out-of-plane lattice constant $a_L^\perp$ refers to the lattice constant parallel to the growth direction. In case of fully strained semiconductors, the in-plane lattice constant of the deposited material $a_L^{||}$ equals the one of the substrate a_S^0. Consequently, the out-of-plane lattice constant of the deposited semiconductor $a_L^{\perp}$ changes according to the following equation:

$$a_L^{\perp} = \frac{C_{11} + 2C_{12}}{C_{11}} \left(a_L^0 - a_S^0 \right) + a_S^0 \tag{2.5}$$

where C_{11} and C_{12} are the elastic constants. For GaAs, C_{11} and C_{12} amount to 118 GPa and 53.5 GPa [36]. By combining equation 2.4 and equation 2.5 with $a_{Ga(As,N)} = a_L^0$ and $a_{GaAs} = a_S^0$, one can now calculate the fully strained out-of-plane lattice constant of Ga(As,N) $a_{Ga(As,N)}^{\perp}$ grown on GaAs:

$$a_{Ga(As,N)}^{\perp} = 5.65325\ \text{Å} - 2.16086\ \text{Å} \cdot x \tag{2.6}$$

Hence, from the analysis of the out-of-plane lattice constant, one can deduce the nitrogen concentration. In case of a fully relaxed heterostructure [figure 2.2 (b)], the deposited semiconductor retains its unstrained lattice constant a_L^0. As a result, owing to different lattice constants of substrate and deposited semiconductor, misfit dislocations are prevalent. Dislocations refer to lines of defects that result when a part of the crystal slips relative to another part. In case of misfit dislocations, these lines of defects lie in the interface.

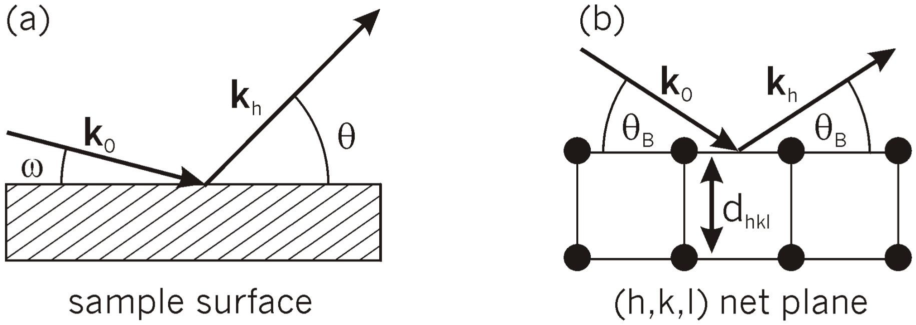

Figure 2.3: The geometry of an XRD setup (a). ω and θ refer to the angles between the sample surface and the incident and diffracted x-ray beams, respectively. The hatched pattern denotes the lattice planes. The Bragg condition is satisfied if the angles between lattice plane and incident x-ray beam as well as diffracted x-ray beam equal the Bragg angle θ_B, as depicted in (b).

XRD is a powerful tool to examine the in-plane and out-of-plane lattice constant of semiconductors. In XRD measurements, parallel x-ray beams of a well-defined wavelength λ are focused on the sample under a certain angle ω with respect to the sample surface. The diffracted beam is measured by a detector under an angle θ. Figure 2.3 (a) illustrates the geometry of an XRD setup. Let us consider an XRD measurement around the (h,k,l) reflection. (h,k,l) stand for the Miller indices that represent a reciprocal lattice point. The set of parallel lattice planes with a spacing d and a vector $\mathbf{h}$ normal to these lattice planes is defined by the lattice constant and the Miller indices. The vector normal to the lattice planes simply equals the Miller indices, $\mathbf{h} = (h,k,l)$, whereas the spacing is defined by: $d_{hkl} = a/(h^2 + k^2 + l^2)^{1/2}$. The Bragg angle of the deposited layers θ_B depends upon the lattice plane spacing d_{hkl} via the Bragg condition:

$$\lambda = 2d_{hkl} \sin\theta_B \tag{2.7}$$

Hence, if the incident and diffracted x-ray beam – represented by wavevectors $\mathbf{k}_0$ and $\mathbf{k}_h$, respectively – are aligned to fulfill the Bragg condition 2.7, as depicted in figure 2.3 (b), the intensity of the diffracted x-ray beam is at a maximum. One possible way to accomplish XRD measurements is to scan along the ω axis while moving the detector angle θ at twice the speed. As θ changes twice as fast as ω, these scans are called $\omega/2\theta$ scans. On the contrary, in ω scans, solely ω is altered, whereas θ remains fixed. These scans move along in a different direction of the reciprocal space with respect to $\omega/2\theta$ scans. Scanning in different directions of the reciprocal space will be discussed in the following paragraph. To determine ω and θ, one has to distinguish between symmetric and asymmetric scans. Figure 2.4 illustrates symmetric (a) and asymmetric XRD scans (b). For symmetric scans, the vector normal to the lattice planes $\mathbf{h}$ coincides with the vector that is normal to the sample surface $\mathbf{n}$. In this case, $\omega = \theta = \theta_B$. Symmetric scans are useful to study the out-of-plane lattice constant. In case of asymmetric scans, the lattice planes are tilted with respect to the sample surface. Its inclination angle ϕ amounts to:

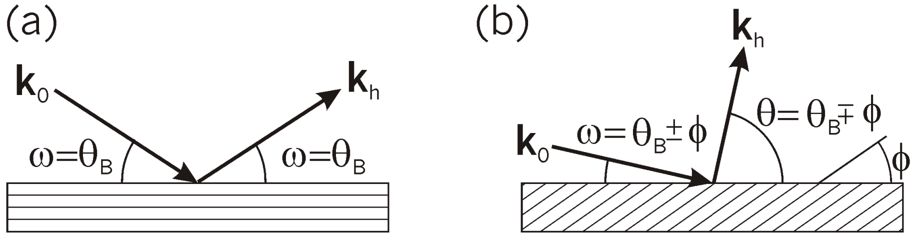

Figure 2.4: Symmetric (a) and asymmetric XRD scans (b).

$$\phi = \arccos\left(\frac{\mathbf{h}\cdot\mathbf{n}}{|\mathbf{h}|\cdot|\mathbf{n}|}\right) \tag{2.8}$$

In this case, $\omega = \theta_B \pm \phi$, whereas $\theta = \theta_B \mp \phi$. Asymmetric scans reveal information of both, in-plane and out-of-plane lattice constant.

A very elegant way to determine in-plane and out-of-plane lattice constants is to employ asymmetric reciprocal space mapping (RSM). RSM refers to two-dimensional scans of the reciprocal space. As mentioned in the last paragraph, the $\omega/2\theta$ and the ω scans move along in different directions of the reciprocal space. Thus, by accomplishing $\omega/2\theta$ scans in dependence of ω, one obtains a two-dimensional map of the reciprocal space. Figure 2.5 depicts the reciprocal space around the (224) lattice point. Let us assume a semiconductor with a smaller lattice constant deposited on a (001) substrate. In this case, the [001] and [100] directions are related to the in-plane and out-of-plane lattice constant, respectively. Moving up the [001] ([100]) direction refers to a decrease of the out-of-plane (in-plane) lattice constant and vice-versa. The black point in figure 2.5 denotes the reciprocal lattice point of the substrate, whereas the gray points denote the reciprocal lattice points of the deposited semiconductor material. Two cases have to be distinguished. First, the deposited semiconductor is fully strained. Second, the deposited layer is relaxed. In the first case, the in-plane lattice constant equals the one of the substrate (cf. figure 2.2). Hence, the reciprocal lattice points of substrate and deposited semiconductor have the same position with respect

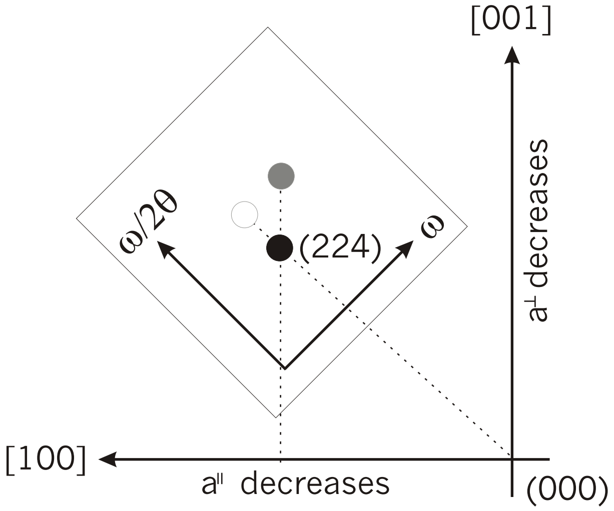

Figure 2.5: RSM of a semiconductor layer with a smaller lattice constant grown on a (001) substrate. The black point denotes the substrate peak, whereas the gray points refer to the fully strained (filled) and relaxed (hollow) semiconductor layer.

to the [100] direction. So they are aligned along the [001] direction. This case is illustrated by the filled gray point. In case of a relaxed heterostructure, the in-plane lattice constant is smaller with respect to the substrate. In addition, the out-of-plane lattice constant is larger compared to the fully strained heterostructure (cf. figure 2.2). This case is denoted by the hollow gray point. Consequently, the reciprocal lattice point of substrate and deposited semiconductor deviate from the [001] direction. Thus, by determining the reciprocal lattice points of a heterostructure, RSM provides information about the strain status of the deposited semiconductor. RSM may also serve as a signature of the presence/absence of misfit dislocations. Experimental results of RSM will be presented in section 3.2.

Apart from studying relaxation processes, XRD is also beneficial for assessing the structural quality of a multi-quantum well (MQW) structure. MQWs refer to an intermittent

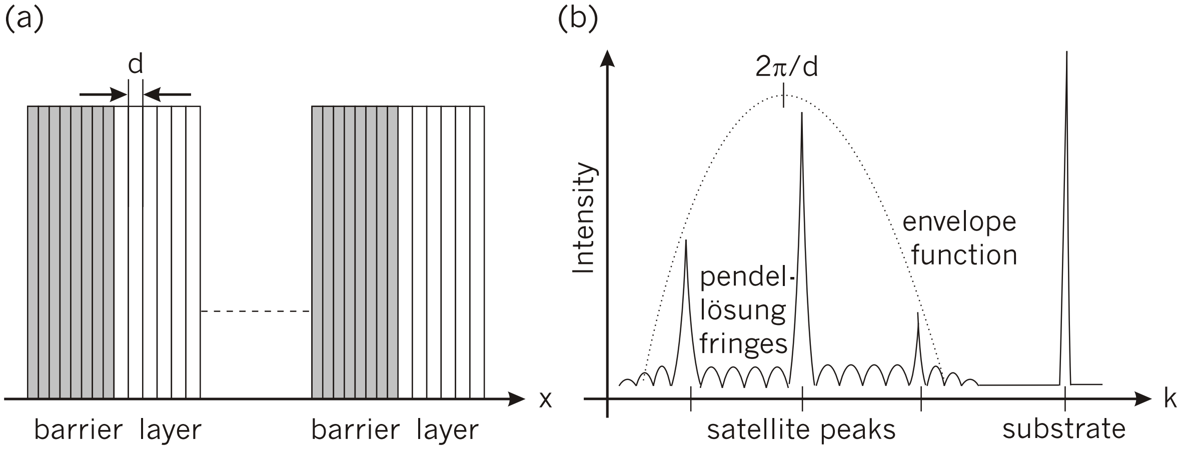

Figure 2.6: A schematic of a MQW structure in real space (a) and the pertinent XRD curve (b).

array of semiconductor layers that are surrounded by a barrier material. The structural quality is determined by the smoothness of the interfaces and the abruptness of the concentration profile of the constituent semiconductors. Figure 2.6 shows a schematic of a MQW structure in real space (a) as well as its XRD curve (b). There are three features in the XRD curves of MQWs from which the structural quality may be assessed: satellite peaks, pendellösung fringes, and the envelope function. Satellite peaks and pendellösung fringes reveal information about the smoothness of the interfaces. Smooth interfaces are manifested by narrow satellite peaks and the presence of pendellösung fringes. Rough interfaces result in a breaking of the translational symmetry of the periodic array of layers and barriers. As a result, there is a broadening of the satellite peaks and a vanishing of the pendellösung fringes. In section 3.3, the structural quality will be assessed by means of XRD. Besides, the envelope function may provide information regarding the abruptness of the concentration profile. If d is the spacing of the deposited layer's probed lattice planes, the maximum of the envelope function is located at $2\pi/d$. As pointed out in the preceding paragraphs, the out-of-plane lattice constant depends upon the concentration of the constituent semiconductors (equation 2.6). Hence, XRD scans may reveal information of the concentration profile within the semiconductor layers. For example, a thermal treatment might result in interdiffusion processes within the layer/barrier stack. Consequently, there is a change of the lattice constant within the semiconductor layer that leads to a shift of the envelope function. Experimental evidence of interdiffusion processes determined by means of XRD is given in section 4.2.

As pointed out in the preceding paragraph, the structural quality of a semiconductor heterostructure may be assessed by means of several features in XRD curves. A simulation of XRD curves is therefore a beneficial tool for these assessments. The dynamical theory, based on the Takagi-Taupin equations, provides a mathematical framework to accomplish such simulations[37]. These equation take into account the change of the amplitude of incident and diffracted XRD beam with respect to the penetration depth. In addition, material parameters of different semiconductor layers are taken into consideration. In fact, nowadays the dynamical theory is implemented in most XRD simulation programs. However, many of these programs rely on a linear dependence between the lattice mismatch and the change of Bragg angles of substrate and layer. This assumption is valid for small angles only. Hence, for highly strained semiconductor heterostructures, these programs fail to find an agreement between the experimental and simulated XRD curves. To solve this problem, Brandt *et al.* [38] have developed a model that accurately determines the change of the Bragg angles with respect to the lattice mismatch. Consequently, the simulations based on this model match the experimental XRD curves even of highly strained semiconductor heterostructures. The simulated XRD curves presented in the following chapters originate from a computer program that is based on this model.

Summary Lattice-mismatched heterostructures are either fully strained, partly relaxed, or fully relaxed. In case of fully strained heterostructures, in-plane and out-of-plane lattice constant differ. To examine these lattice constants, XRD is employed. It is also beneficial to assess the structural quality of MQWs.

2.3 Molecular Beam Epitaxy

MBE is a versatile growth technique to deposit atomically abrupt layers of semiconductor materials on a substrate. A schematic of an MBE system is depicted in figure 2.7. The main component is a vacuum chamber equipped with effusion cells which are filled with different materials. The MBE system, used to grow the samples of this work, is equipped with gallium, indium, and aluminum as group III elements, arsenic and nitrogen as group V elements, and silicon and beryllium for n-type and p-type doping, respectively. By increasing the temperature of these effusion cells, thermally-induced atomic or molecular beams of the constituent elements are created. These atomic or molecular beams impinge on the substrate surface which is also kept at elevated temperature. The growth rate is determined by the arrival rates of the group III elements which is a function of the effusion cell temperatures. The growth rate, typically 1 μm per hour, is low enough to assure sufficient surface migration of the impinging species. Thus, one can achieve atomically smooth surfaces of MBE-grown layers. The incorporation of a specific element is controlled by simple mechanical shutters placed in front of the effusion cells that interrupt the atomic or molecular beams. Thus, one can accomplish abrupt interfaces between layers of different compositions on an atomic scale.

Apart from effusion cells, nitrogen is supplied by a radio frequency (rf) plasma source. Microwave radiation with a frequency of 13.56 MHz is coupled to a cavity to convert an ultrapure molecular nitrogen flow into atomic nitrogen. The nitrogen flow is regulated with a mass flow controller which is optimized for dilute nitride growth. The applied microwave power is controlled by a power supply. For minimizing the reflected microwave power, a matching unit is employed to assure resonance conditions of the microwave radiation in the cavity. An important feature of growing GaAs-related materials by means of MBE is the arsenic overpressure, or beam equivalent pressure (BEP) ratio. The BEP ratio is defined by the ratio between the partial pressure of As and the partial pressure of group III elements. For growing GaAs based materials, the partial pressure of As usually exceeds the one of the group III elements. A typical BEP ratio for growing Ga(As,N) is 20.

MBE growth takes place under UHV conditions in the 10^{-10} mbar range . To accomplish such pressures, ion-getter pumps are employed that have a working range of $10^{-6} - 10^{-10}$ mbar. In addition, a cryoshroud encompasses the entire inner surface of the growth chamber. This cryoshroud is filled with liquid nitrogen that causes a freezing out of remaining particles in the growth chamber. Hence, a further improvement of the vacuum conditions is accomplished. However, during the growth of Ga(As,N) and (In,Ga)(As,N), the pressure inside the growth chamber increases up to 10^{-5} mbar because of high partial pressures of nitrogen and arsenic. Therefore, a cryopump is employed during growth runs that has a working range of $10^{-3} - 10^{-10}$ mbar.

To in-situ monitor the growth, reflection high-energy electron diffraction (RHEED) is employed. In RHEED measurements, an electron beam impinges on the sample surface at a grazing angle, thus penetrating only the topmost atomic layers of the sample. From the diffraction pattern, one retrieves information about the surface morphology, e.g. two-dimensional or three-dimensional growth. If the diffraction pattern is streaky, two-dimensional growth occurs, whereas a spotty diffraction pattern indicates three-dimensional growth. In addition, from RHEED one also obtains information of the

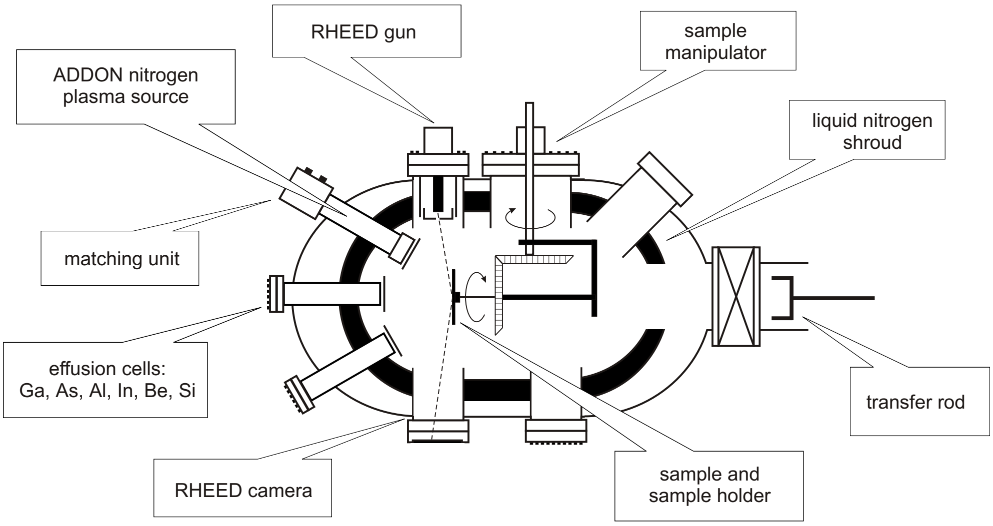

Figure 2.7: A schematic of an MBE growth chamber.

substrate temperature. The substrate temperature is a crucial parameter, even though it is a delicate issue. Different substrates (doped or undoped) and different substrate holders have different substrate temperatures with the same heating power applied. Therefore, one has to distinguish between the real substrate temperature and the temperature displayed in the MBE control panel (Eurotherm control display). Nevertheless, RHEED can be employed to determine the real substrate temperature by observing the transition of surface reconstructions as well as determining the temperature of oxide desorption. The oxide desorption temperature of GaAs is a well defined at 580°C [39]. For a given BEP ratio, the transition of surface reconstructions is also well defined[36]. Thus, there are several fixed temperatures to find the desired real substrate temperature. Figure 2.8 shows the correlation of the Eurotherm control display and the real substrate temperature for doped and undoped GaAs substrates using the same substrate holder. Apparently, there is a strong deviation between these different types of substrates. Determining the substrate temperature is crucial for optimizing the growth of Ga(As,N) and (In,Ga)(As,N). This issue will be discussed in section 3.1 and 4.1.

An important feature of the MBE growth technique is the growth rate. The growth rate stands for what amount of material in terms of layer thickness is deposited per unit time. It is essential for tailoring the composition and thickness of the deposited layers. The measurement of the RHEED intensity oscillation of the specular beam is a very accurate way to determine the growth rate. For GaAs (001) substrates, the period of such oscillation corresponds exactly to the growth of a single monolayer (half a lattice constant). The physical origin of the RHEED intensity oscillations lies in the fact that the maxima of intensity always occur for smooth surfaces when a monolayer is completely deposited. In case the deposition of a monolayer is not complete, the surface is atomically rough, causing a higher diffuse scattering. Hence, there is a reduction of the RHEED intensity. The growth rates are important for controlling the concentrations of the constituent elements. This issue will be discussed in section 3.1 and 4.1.

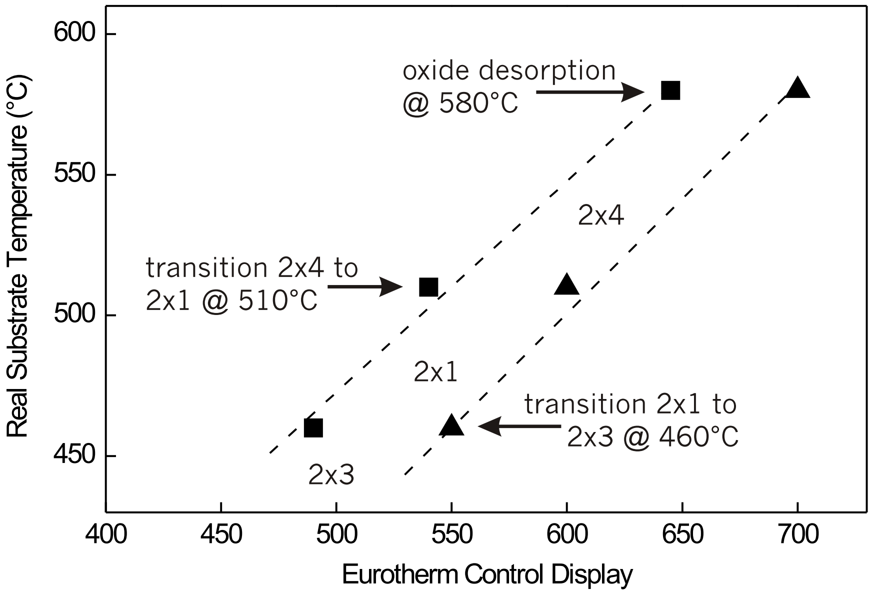

Figure 2.8: Real substrate temperature versus Eurotherm control display for undoped (triangles) and doped GaAs (001) substrate (squares). The same sample holder was used for this analysis. The BEP ratio was kept at 20.

Summary MBE is a versatile growth technique to deposit atomically abrupt semiconductor layers on a substrate. MBE systems consist of a ultrahigh vacuum chamber equipped with effusion cells. The deposition of material is accomplished by thermally-induced molecular or atomic beams that impinge on the substrate surface. The ultrahigh vacuum is generated by either ion getter pumps or cryopumps. RHEED is employed to observe the sample surface during growth. It also gives information about the substrate temperature and growth rates.

Chapter 3

Ga(As,N): Growth and Properties

3.1 MBE-Growth of Ga(As,N)

Comprehending the growth of Ga(As,N) is an essential prerequisite to harness this material system for light emitting devices. In addition, it is of utmost importance to understand the ternary Ga(As,N) material system before investigating the substantially more complex quaternary (In,Ga)(As,N) material system. Hence, this section deals with the optimization of the Ga(As,N) growth, strategies of controlling the nitrogen incorporation into GaAs, and techniques to determine the nitrogen concentration.

The optimization of Ga(As,N) growth A vital issue and a wide field of investigation is the optimization of Ga(As,N) growth as there are numerous parameters that influence the incorporation of nitrogen into GaAs. Most important are the substrate temperature, the BEP ratio, and the nitrogen plasma source parameters. To assess the impact of theses growth parameters, structural and optical properties were analyzed. Structural properties refer to smooth surfaces and interfaces, determined by in-situ RHEED, as well as ex-situ atomic force microscopy (AFM), and XRD. Optical properties are determined through the PL intensity, FWHM value, and the wavelength of the PL emission.

Among numerous growth parameters, the substrate temperature is most important for growing Ga(As,N) by virtue of a large miscibility gap of GaN in GaAs. Ho *et al.* [40] have theoretically investigated the miscibility gap, calculating a maximum nitrogen concentration of 10^{-10} at a temperature of 600°C. Higher nitrogen concentrations result in a roughening of surfaces and interfaces in this material system. This roughening is observable by the in-situ RHEED pattern. If the RHEED pattern appears streaky, a two-dimensional growth occurs. In contrast, a roughening causes a three-dimensional growth that is discernable by a spotty RHEED pattern. In addition, the structural degradation is ascertained by means of ex-situ XRD and AFM. The roughening is manifested by smeared out XRD curves without the presence of pendellösung fringes. For these samples, AFM images show rough surfaces with a root mean square (RMS) value that amounts to several nanometers. For smooth Ga(As,N) samples, the RMS value is less than 1 nm. This roughening also causes a degradation of optical properties that is seen by a diminishing of the PL intensity and an increase of the FWHM value. A way to avoid a roughening of surfaces and interfaces is to grow under nonequilibrium conditions, i.e. low substrate temperatures[41, 42]. Hence, the substrate temperature is crucial for growing Ga(As,N). Figure 3.1 demonstrates the impact of the substrate temperature on the growth of Ga(As,N). Several Ga(As,N)/GaAs MQWs with different nitrogen concentrations have been grown at different substrate temperatures. The samples consist of a 10-period (10/20) nm Ga(As,N)/GaAs MQW structure. The samples are classified in samples that show streaky RHEED patterns – symbolized by blank squares – and samples that reveal spotty RHEED patterns – represented by filled squares. Evidently, at high substrate temperatures (e.g. 550°C), it is barely possible to incorporate even small amounts of nitrogen into GaAs without causing a roughening of the samples. On the contrary, growing at lower substrate temperatures (e.g. 450°C), one can incorporate larger amounts of nitrogen into Ga(As,N) without causing a roughening. In this case, samples maintain the streaky RHEED pattern. In order to illustrate the transition from streaky to spotty RHEED pattern, figure 3.2 shows the $[110]$ and $[1\bar{1}0]$ RHEED patterns of a Ga(As,N) sample with 2.2% nitrogen grown at 550°C (sample 2 in figure 3.1). By increasing the amount of the deposited Ga(As,N), there is a clear trend from streaky to spotty RHEED patterns. During the growth of the first Ga(As,N) layer, the RHEED pattern appears streaky, whereas it gradually becomes spotty during the growth of subsequent Ga(As,N) layers. To gain further insight into the impact of the roughening of Ga(As,N)/GaAs MQWs, XRD as well as AFM have been accomplished. Figure 3.3 shows RHEED pattern, XRD curves, and AFM images of Ga(As,N) samples with different nitrogen concentrations grown at the same substrate temperatures (sample 1 and 3 in figure 3.1) as well as Ga(As,N)

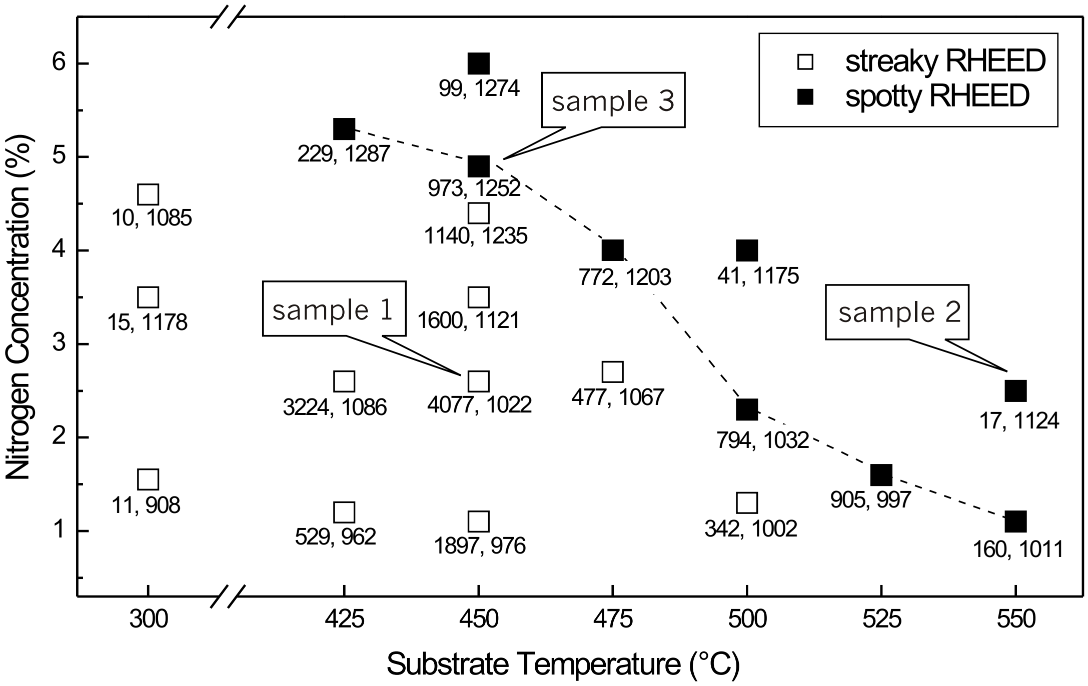

Figure 3.1: Properties of 10-period Ga(As,N)/GaAs MQWs with 10 nm Ga(As,N) surrounded by 20 nm GaAs with different nitrogen concentrations grown at different substrate temperatures. The first number underneath the squares denotes the PL intensity for the samples annealed at 800°C for 60 s (see chapter 3.3). The second number stands for the spectral positions of the PL maxima in nm. The PL measurements were carried out at 10 K.

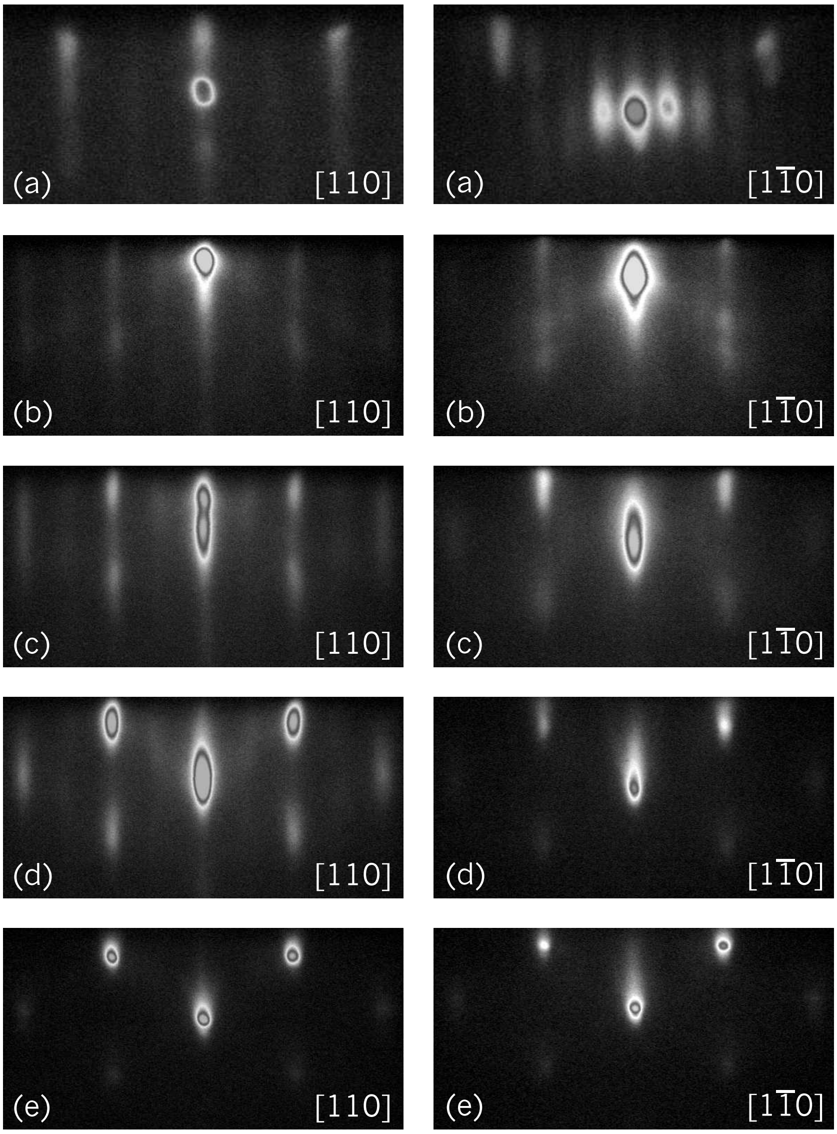

Figure 3.2: [110] and $[1\bar{1}0]$ RHEED patterns of sample 2 in figure 3.1; during the growth of the GaAs buffer layer at 580°C with a BEP ratio of 20 (a), growth interruption prior to growth of Ga(As,N) at 550°C (b), first Ga(As,N) layer (c), second Ga(As,N) layer (d), and third Ga(As,N) layer (e).

samples with the same nitrogen concentration but grown at different substrate temperatures (sample 1 and 2 in figure 3.1). Univocally, there is a structural degradation of the samples that show a spotty RHEED pattern. In case of these samples, one can discern rough surfaces by means of AFM. Besides, the satellite peaks of the XRD curves are broadened without the presence of pendellösung fringes. Apart from a degradation of structural properties, there is also a degradation of optical properties in case of Ga(As,N) samples that show a spotty RHEED pattern, such as a diminishing of the PL intensity. The PL intensity – taken relative to a reference sample[1] – is denoted by the first number underneath the squares in figure 3.1. Interestingly, the highest PL intensi-

---

[1] For the sake of comparison, the same reference sample has been employed for all PL measurements throughout this work.

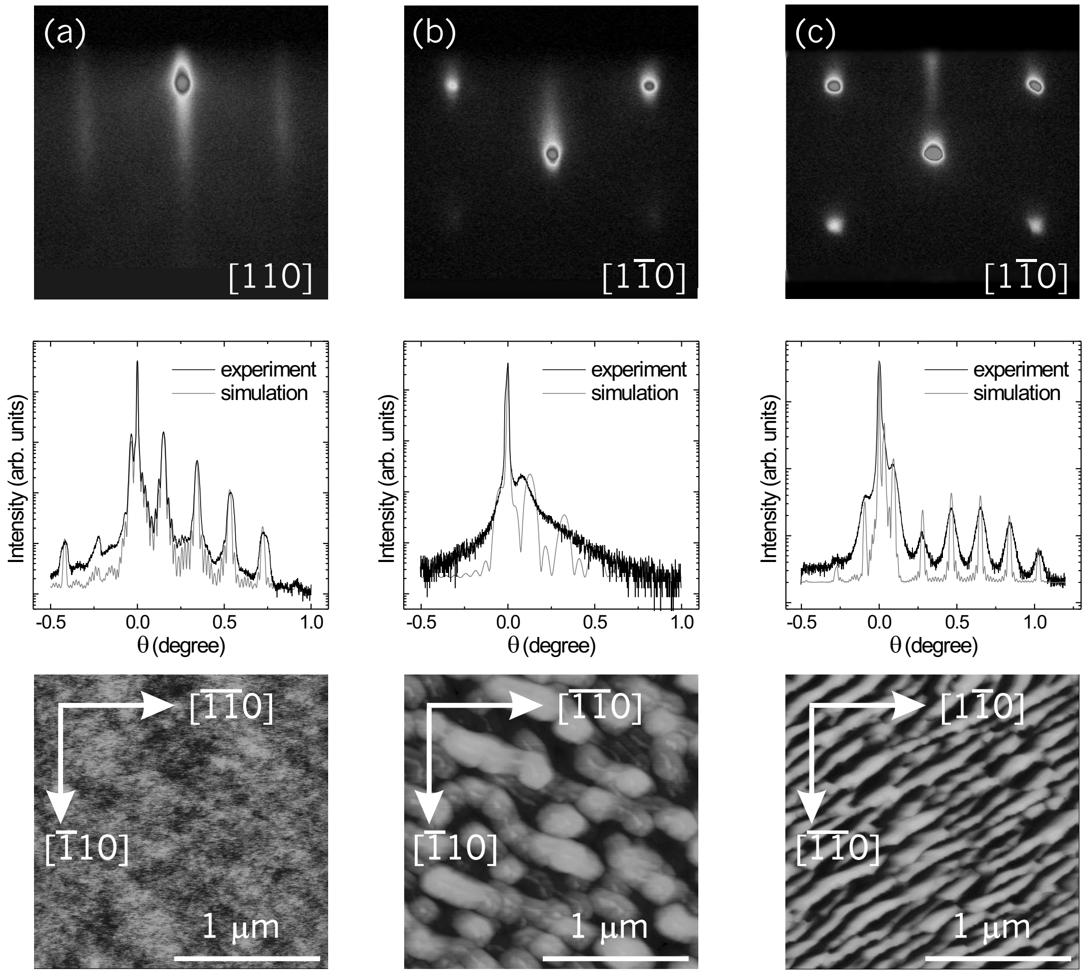

Figure 3.3: RHEED pattern, XRD curves around the (004) reflection, and AFM images of sample 1 (a), 2 (b), and 3 (c) in figure 3.1. The RMS values of the AFM images amount to 0.2 nm (a), 16 nm (b), and 17 nm (c).

ties are not obtained from Ga(As,N) samples with the smallest amount of nitrogen that are expected to have the lowest concentrations of defects (see section 3.3). This can be elucidated with a smaller band alignment offset, especially in the valence band. For example, the valence band offset of Ga(As,N)/GaAs with 3% nitrogen amounts to solely 11 meV[43]. For lower nitrogen concentrations, it is even smaller. Thus, these low energy barriers can be easily overcome even at cryogenic temperatures. As a result, holes are thermally activated out of the Ga(As,N) QWs, which leads to a diminishing of the PL intensity. Figure 3.1 also depicts Ga(As,N) samples grown at 300°C. Obviously, growing at very low substrate temperatures also causes a degradation of optical properties. This is possibly due to a higher point defect concentration that is well known for GaAs grown at low temperatures[44, 45, 46]. Hence, regarding the substrate temperature of growing Ga(As,N), one has to find a compromise between structural and optical properties. Obviously, a substrate temperature of 450°C seems to be suitable for incorporating up to 4% nitrogen into GaAs.

Another major parameter regarding the growth of Ga(As,N) is the BEP ratio. To investigate the impact of the BEP ratio upon the incorporation of nitrogen into GaAs, four

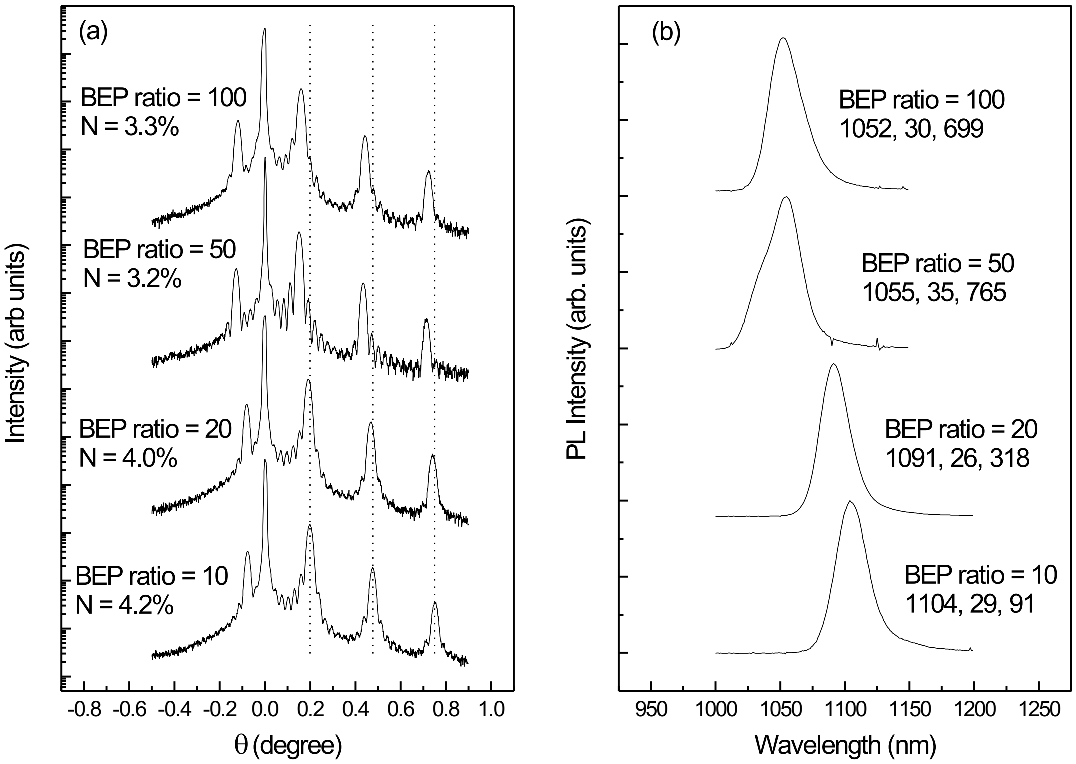

Figure 3.4: XRD curves around the (004) reflection (a) and PL spectra (b) of four 10-period (10,20) nm Ga(As,N)/GaAs MQWs grown with different BEP ratios. PL measurements were accomplished on Ga(As,N) samples annealed at 800°C for 60 s. The measurements were carried out at 10 K. The numbers in figure (b) refer to the spectral position of the PL maximum, the FWHM value, and the PL intensity.

10-period (10/20) nm Ga(As,N)/GaAs MQW samples have been grown with a BEP ratio in a range between 10 and 100. Figure 3.4 shows XRD curves as well as PL spectra of these samples. In figure 3.4 (a), the XRD curves show a shift of the satellite peaks towards the GaAs substrate peak for higher BEP ratios. This shift can be exemplified with a lower nitrogen incorporation for higher BEP ratios. The nitrogen concentrations is deduced from the positions of the satellite peaks, yielding values from 3.3% nitrogen (BEP ratio = 100) to 4.2% nitrogen (BEP ratio = 10). To bear out the observation of a reduced nitrogen incorporation for higher BEP ratios, PL measurements were carried out. Figure 3.4 (b) shows PL spectra of these four samples. Unequivocally, there is a PL redshift for lower BEP ratios. This PL redshift affirms the assumption of a higher nitrogen incorporation for lower BEP ratios. With a higher nitrogen concentration, the band gap decreases resulting in a shift of the position of the PL maxima towards longer wavelengths. To explain this phenomenon of a lower nitrogen incorporation for higher BEP ratios, one might think of a lattice site competition between arsenic and nitrogen. Both species regularly incorporate into the arsenic lattice site. With a lower amount of arsenic in the growth chamber, there is a higher probability of nitrogen atoms to incorporate into arsenic lattice sites, resulting in an increase of the nitrogen concentration. Nonetheless, regarding structural properties of Ga(As,N) samples grown at different BEP ratios, no trend is observed by means of RHEED, AFM, and XRD. In figure 3.4 (a), all XRD curves show narrow satellite peaks as well as pendellösung fringes. Concerning optical properties, there is a diminishing of the PL intensity with higher BEP ratios. This phenomenon might be attributed to the higher nitrogen concentration that is concomitant with a higher concentration defects (see also section 3.3).

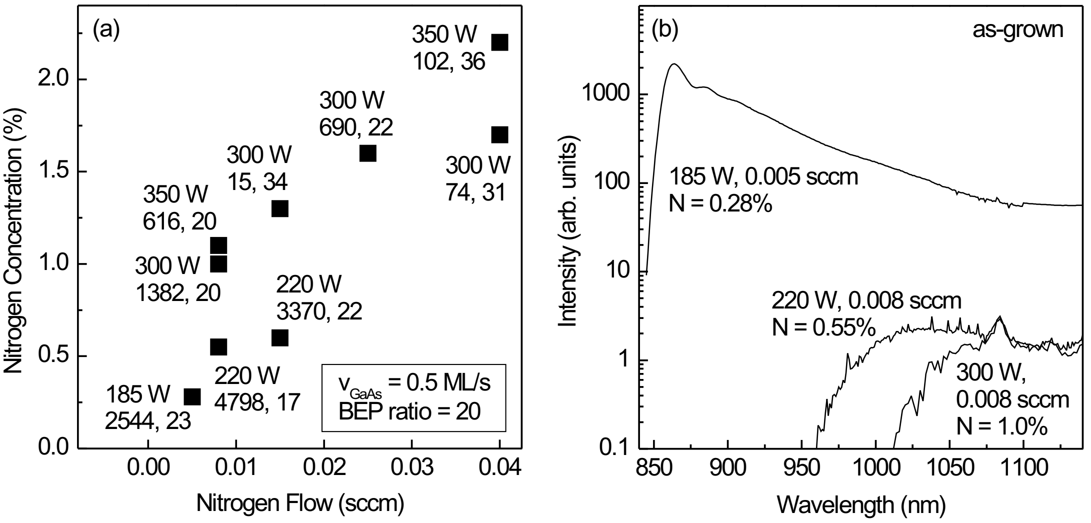

Figure 3.5: Nitrogen concentration versus the nitrogen flow of 10-period Ga(As,N)/GaAs MQWs samples grown with different plasma source parameters (a). The numbers refer to the plasma source power, the PL intensity, and the FWHM value (for samples annealed at 800°C for 60 s). PL spectra of as-grown Ga(As,N)/GaAs MQWs grown with different plasma source parameters (b). A strong enhancement of the PL is achieved by growing at low plasma source powers and nitrogen flows. All PL measurements were carried out at 10 K.

Another critical issue are the plasma source parameters, namely the plasma source power and the nitrogen flow. Figure 3.5 (a) depicts the nitrogen incorporation of Ga(As,N)/GaAs MQW samples with respect to different nitrogen flows. The GaAs growth rate was kept constant at 0.5 ML/s. In addition, the plasma source power was altered which is denoted by the upper number; the lower numbers represent the PL intensity and the FWHM value for samples annealed at 800°C for 60 s. Evidently, there is a higher nitrogen incorporation with higher plasma source power and/or higher nitrogen flow. Concerning optical properties, there is a strong enhancement with a lower nitrogen flow and plasma source power because of a higher PL intensity and a lower FWHM value. To illustrate the enhancement of optical properties for lower plasma source powers and nitrogen flows, figure 3.5 (b) shows PL spectra of as-grown Ga(As,N) samples that were grown with different plasma source parameters. Obviously, a weak PL signal is observed from the samples grown with high plasma source power and high nitrogen flow. Moreover, the spectral position of the PL signal lies deep in the band gap, stemming from defect-related radiative recombination. On the contrary, the PL signal of the sample grown with low plasma source power and nitrogen flow (185 W, 0.005 sccm) shows a strong signal where the band gap is expected. Hence, we conclude a lower concentration of defects created by the plasma source which serve as nonradiative recombination centers as well as radiative recombination centers in the band gap. These issues will be discussed in section 3.3 and 3.4.

To control the nitrogen concentration, two strategies can be employed. First, one can control the amount of atomic nitrogen produced by the rf-plasma source [see figure 3.5

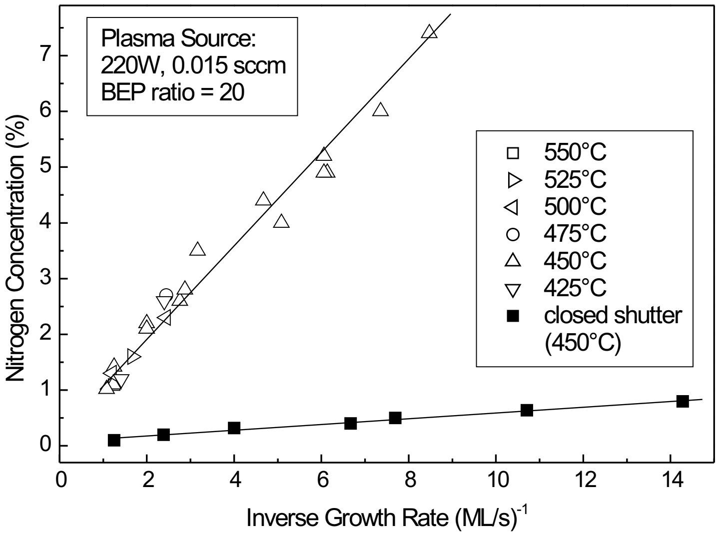

Figure 3.6: Nitrogen concentration versus the inverse GaAs growth rate for different substrate temperatures with open and closed nitrogen shutter.

(a)]. Second, one can control the GaAs growth rate. The main drawback of the first strategy lies in the fact of a strong degradation of optical properties with higher nitrogen flows and plasma source powers. Therefore, one should keep the plasma source power and nitrogen flow as low as possible. On the other hand, by changing the GaAs growth rate under a constant BEP ratio, one can control the nitrogen incorporation owing to a unity sticking coefficient of nitrogen[33, 47, 48, 49, 50]. As a result, a constant fraction of the amount of atomic nitrogen that impinges on the substrate surface incorporates into GaAs. With this knowledge, it is facile to control the nitrogen incorporation as the nitrogen concentration N is proportional to the inverse GaAs growth rate v_{GaAs}:

$$N \propto 1/v_{GaAs} \tag{3.1}$$

Therefore, theoretically one Ga(As,N) sample suffices to calibrate the nitrogen incorporation. For this analysis, 28 Ga(As,N) samples have been investigated. Figure 3.6 shows the correlation between the inverse GaAs growth rate and the nitrogen concentration for different substrate temperatures with constant plasma source parameters. One can clearly see a linear dependence. One can also observe nitrogen incorporation with a closed nitrogen shutter (solid squares). From the slopes of both lines, the nitrogen concentration on/off ratio amounts to 11. That means even with a closed shutter, there is a nitrogen incorporation with a concentration of 1/11 with respect to an open shutter. Hence, with a closed nitrogen shutter, one can grow ultradilute (bulk) Ga(As,N) samples with nitrogen concentrations of less than 0.02%. Several authors have made use of the closed shutter nitrogen incorporation[51, 52, 53].

Another important issue about the incorporation of nitrogen into GaAs is the homogeneity of the nitrogen concentration throughout the sample. For this analysis, two 10-period Ga(As,N)/GaAs MQWs were grown with a nominal nitrogen concentration of 3% and a Ga(As,N) well thickness of 10 nm. The samples were subsequently cleaved

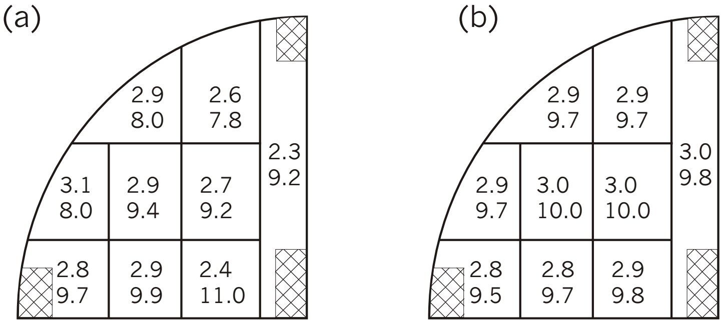

Figure 3.7: Investigation concerning the homogeneity of the nitrogen concentration (upper number, in percent) and the well thickness (lower number, in nm) of two Ga(As,N)/GaAs MQWs samples grown without (a) and with substrate rotation (b).

into 9 pieces to analyze the nitrogen concentration and the Ga(As,N) well thickness. Figure 3.7 shows the nitrogen concentration (upper number) and the Ga(As,N) well thickness (lower number) of all 9 pieces for the samples grown without (a) and with substrate rotation (b). In case of the sample grown without substrate rotation, a strong deviation of the nitrogen concentration and Ga(As,N) well thickness is found because of an inhomogeneous spatial distribution of the gallium and nitrogen atomic beams that impinge on the substrate surface. On the contrary, the Ga(As,N) sample grown with substrate rotation shows a homogeneous nitrogen concentration and well thicknesses throughout the sample. Thus, the substrate rotation is vital for growing homogeneous Ga(As,N) samples regarding the nitrogen concentration and the well thickness. The spatial homogeneity of the nitrogen concentration is an important issue, as in the following sections, samples will be cleaved into several pieces for a subsequent characterization. Thus, one has to warrant the same nitrogen concentration of all pieces.

Determination of the nitrogen concentration The above description about the nitrogen incorporation requires the accurate knowledge of the nitrogen concentration. There are two independent techniques that can be applied to measure the amount of nitrogen in Ga(As,N): XRD and PL. As discussed in section 2.2, the out-of-plane lattice constant depends linearly upon the nitrogen concentration (equation 2.6). Therefore, by determining the out-of-plane lattice constant of Ga(As,N) via XRD, one can deduce the nitrogen concentration. However, the precision declines if samples of low structural quality are investigated. Such structural degradation leads to broadened XRD peaks. Consequently, it is difficult to analyze XRD curves of samples with a low structural quality. Thus, for determining the nitrogen concentration from XRD measurements, samples have to be of high structural quality.

Another independent technique to determine the nitrogen concentration is PL. As discussed in section 2.1, the position of the PL maximum depends upon the band gap. The band gap of Ga(As,N) is a well-defined function of the nitrogen concentration (equation 2.1). However, this technique is not reliable in case of defects. RTA helps to heal out these defects resulting in a blueshift of the PL spectra. Thus, the spectral position of the PL maximum changes with different RTA conditions (see section 3.3). Therefore, one has to assure to remove defects by means of RTA to deduce the nitrogen

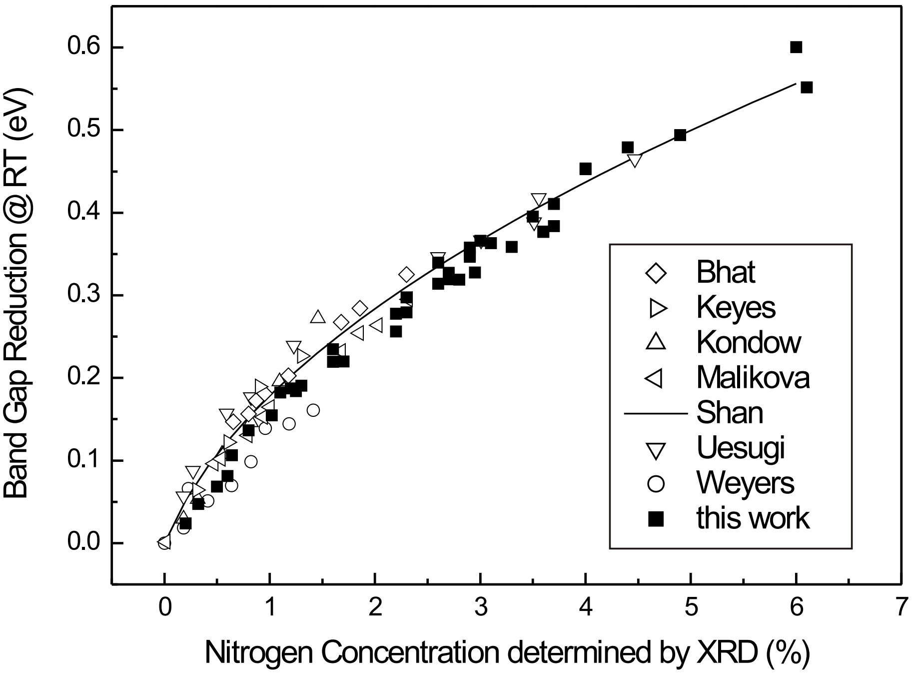

Figure 3.8: Band gap reduction at RT derived from PL measurements versus the nitrogen concentration determined from XRD measurements. Literature values are given for comparison. The solid line represents the E_- band calculated from equation 2.1. The authors in the legend refer to the following citations: Bhat[54], Keyes[55], Kondow[56], Malikova[57], Shan[19], Uesugi[35], and Weyers[3].

concentration from PL.

In order to obtain an insight into the nitrogen-induced band gap reduction, figure 3.8 shows the room temperature (RT) band gap reduction derived from low temperature PL measurements of annealed Ga(As,N) samples[2] versus the nitrogen concentration determined from XRD measurements. Roughly spoken, for low nitrogen concentrations between 0 and 1%, the band gap reduction amounts to 150 meV per percent nitrogen. For higher nitrogen concentrations, it values approximately 100 meV per percent nitrogen. In addition, literature values from several authors have been added to the figure. The solid line refers to the BAC model (equation 2.1). Indeed, the band gap reduction derived from Ga(As,N) samples of this work is in good agreement with literature values.

Summary For optimizing the growth of Ga(As,N), there are several parameters, such as the BEP ratio, nitrogen plasma source parameters, GaAs growth rate, and substrate

---

[2] To determine the band gap reduction at room temperature by means of low temperature PL measurements, two corrections have to be made. First, for Ga(As,N)/GaAs MQWs, the confinement energy has to be taken into account (equation 2.3) that depends on the barrier height and the effective mass. As the incorporation of nitrogen mainly affects the conduction band offset, solely the electron confinement energy was taken into consideration. The barrier height was determined according to equation 2.1. The effective electron mass m_e^* is also nitrogen concentration-dependent. To determine m_e^*, we have used the equation by Skierbiszewski *et al.* [28]. Second, Ga(As,N) shows a different band gap temperature behavior with respect to GaAs. Chtourou *et al.* [17] have developed an equation to calculate this deviation that has been employed for our analysis.

temperature. A low substrate temperature is essential for avoiding a roughening of surfaces and interfaces by virtue of a large miscibility gap. The BEP ratio influences the nitrogen incorporation rate. The plasma source parameters are crucial to minimize the amount of defects generated by the plasma source. Because of a unity nitrogen sticking coefficient, one can control the nitrogen concentration by changing the GaAs growth rate with constant plasma source parameters. To measure the nitrogen concentration of Ga(As,N), XRD or PL measurements can independently be employed.

3.2 Roughening Thickness of Ga(As,N) MQW Structures

In the previous section, the growth of Ga(As,N) has been discussed. We have found that there is a roughening of surfaces and interfaces for high nitrogen concentrations and/or high substrate temperatures. This section deals with the roughening of Ga(As,N)/GaAs MQWs in dependence of the QW thickness and the nitrogen concentration.

Thickness-dependent roughening The samples investigated for this analysis comprise a 10-period $(d, 2d)$ Ga(As,N)/GaAs MQWs (d = well thickness) with nitrogen concentrations ranging from 3 to 7.4% and well thicknesses in between 20 and 2 nm. Three criteria are employed to distinguish between smooth and rough samples. RHEED gives qualitative information about the surface morphology during growth. Samples are considered smooth if the RHEED pattern remains streaky, rough samples are indicated by a spotty RHEED pattern. Ex-situ experiments to analyze the samples smoothness are XRD and AFM. In case of smooth samples, XRD spectra show narrow satellite peaks with pendellösung fringes. In contrast, rough samples show broad satellite peaks without the presence of pendellösung fringes. In order to quantitatively analyze the sample smoothness, AFM has been employed. In case of smooth samples, the RMS value is lower than 1 nm. If roughening occurs, the RMS value abruptly increases to several nanometers. Thus, one can categorize rough samples by defining a certain RMS threshold value. We have found that a threshold value of 2 nm is suitable to classify the Ga(As,N)/GaAs MQWs into smooth and rough samples. Figure 3.9 shows smooth samples (denoted by blank squares) and rough samples (symbolized by filled squares) with respect to the nitrogen concentration and Ga(As,N) well thickness. An abrupt transition between a smooth and a rough morphology is found. The experimentally determined roughening thickness is represented by a dashed line, having a value of 17 nm in case of 4% nitrogen and 3 nm in case of 7.4% nitrogen. The dotted line refers to the Matthews-Blakeslee model[58] (see next paragraphs).
To illustrate the abrupt transition between smooth and rough samples, figure 3.10 shows XRD curves, transmission electron microscopy (TEM), and AFM images of the smooth and rough Ga(As,N) sample with 7.4% nitrogen (sample 1 and 2 in figure 3.9). The smooth sample consists of a Ga(As,N) well thickness of 2 nm, whereas the rough sample comprises 4 nm Ga(As,N) well thickness. Regarding XRD measurements, the smooth sample shows narrow satellite peaks with pendellösung fringes. There is an agreement between experimental data and the simulation. On the contrary, in the XRD curve of the rough sample, satellite peaks are broadened without the presence of pendellösung fringes. From the composition-sensitive (002) TEM image of the smooth sample, one can see coherently grown layers with abrupt interfaces. In contrast, the (002) TEM image of the rough sample shows no coherently strained layers but regions of higher nitrogen concentrations (dark areas). Interestingly, these regions do not necessarily occur at the first Ga(As,N) layer but also start emerging from subsequently grown Ga(As,N) layers. The AFM image of the rough sample shows three dimensional islands with a lateral distance of 150 nm between neighboring islands. The RMS value amounts to 3.6 nm. In case of the smooth sample, the AFM image does not reveal three dimensional islands. In this case, the RMS value is 0.5 nm.

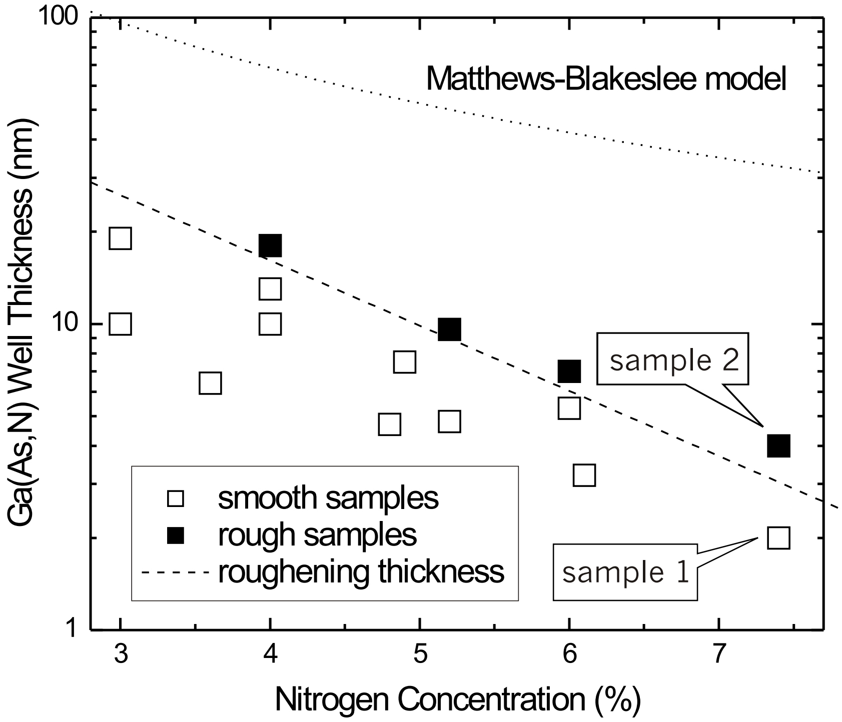

Figure 3.9: Determination of the experimental roughening thickness. Samples have been grown at 450°C under a BEP ratio of 20 and plasma source parameters of 220 W and 0.008 sccm. The nitrogen concentration was controlled by changing the GaAs growth rate. The dotted line refers to the Matthews-Blakeslee model.

Discussion To obtain further insight into the roughening mechanism, we have compared the experimentally determined roughening thickness with a model proposed by Matthews and Blakeslee that calculates the thickness of MQWs when relaxation by formation of misfit dislocation commences[58]. In this model, the critical thickness h_c is given by the recursive equation:

$$h_c = \frac{b}{2\pi f} \frac{\left(1 - \nu \cos^2 \alpha\right)}{(1+\nu)\cos\lambda} \left(\ln \frac{h_c}{b} + 1\right) \tag{3.2}$$

where ν is the Poisson ratio, b is the magnitude of Burger's vector, λ is the angle between slip direction and film plane, α the angle of the dislocation line and Burger's vector, and f the lattice mismatch. Assuming the energetically most favorable 60° misfit dislocations ($\cos\lambda = 0.5$, $\cos\alpha = 0.5$, $b = 4$ Å), one can employ equation 3.2 to iteratively determine h_c. The dotted line in figure 3.9 shows the critical thickness of MQWs with respect to the nitrogen concentration. Univocally, the experimentally determined roughening thickness is substantially lower than the critical thickness determined by the Matthews-Blakeslee model even though h_c refers to the onset when relaxation by creation of misfit dislocations takes place. Experimentally determined critical thicknesses usually exceed the critical thickness determined by the Matthews-Blakeslee model[59, 60, 61]. Consequently, the roughening mechanism of the Ga(As,N) samples cannot be attributed to a relaxation by formation of misfit dislocations. This assumption is further corroborated by the absence of misfit dislocations determined by (004) TEM measurements (not shown here).

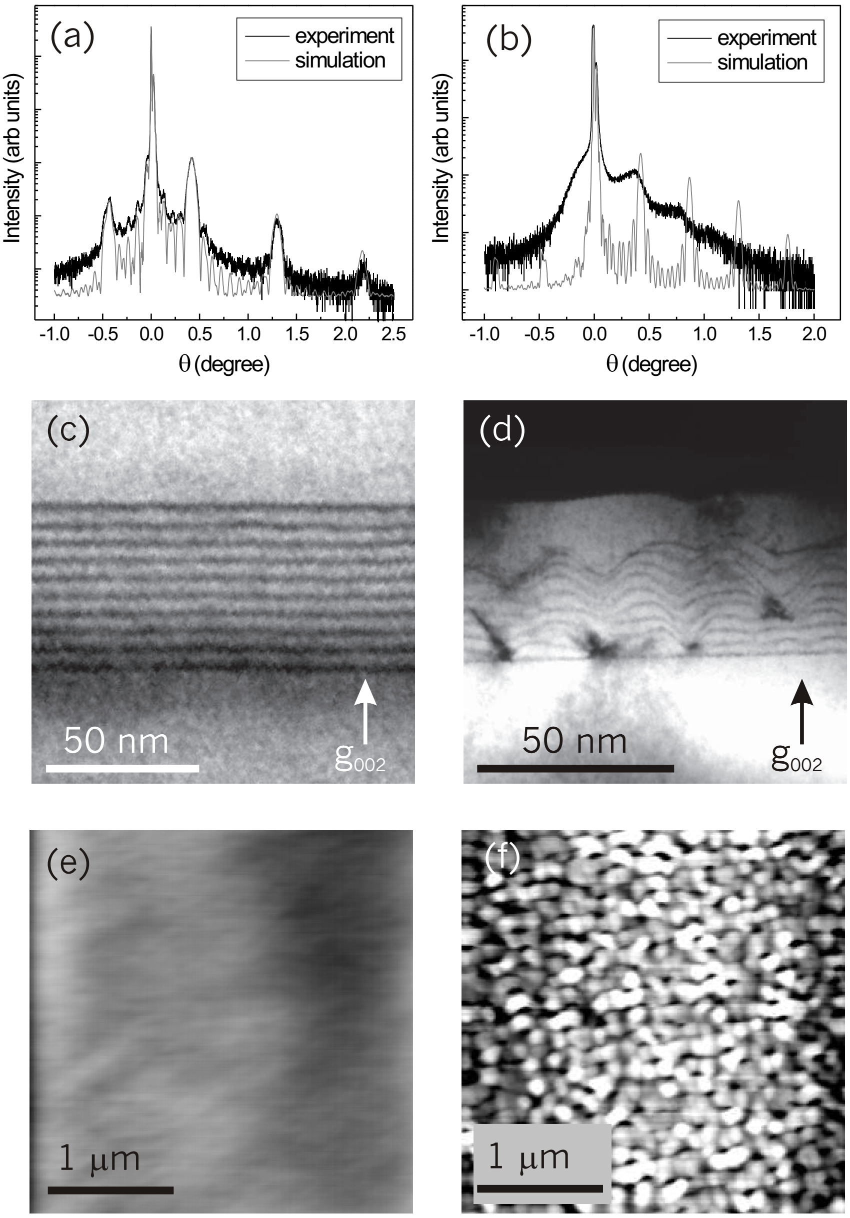

Figure 3.10: (004) XRD curves, (002) TEM, and AFM images of the smooth (left column) and rough (right column) Ga(As,N) sample containing 7.4% nitrogen (sample 1 and 2 ind figure 3.9). The RMS values of the AFM images amount to 0.5 nm (smooth) and 3.6 nm (rough). (TEM taken by A. Trampert.)

To bear out the assumption of a roughening process without the formation of misfit dislocations, RSM was carried out. As depicted in section 2.2, RSM provides information about the the presence/absence of misfit dislocations. Figure 3.11 shows RSM around the (224) reflection of the smooth and rough Ga(As,N) sample with 7.4% nitrogen (sample 1 and 2 in figure 3.9). In case of the smooth sample in figure 3.11 (a), one can clearly see that the zero-order and minus-first-order satellite peak are aligned in the [001] direction, thus indicating no change in the in-plane lattice constant of Ga(As,N) with respect to GaAs (cf. figure 2.5). Consequently, no misfit dislocations are expected in this sample. However, even in case of the rough sample – shown in figure 3.11 (b)

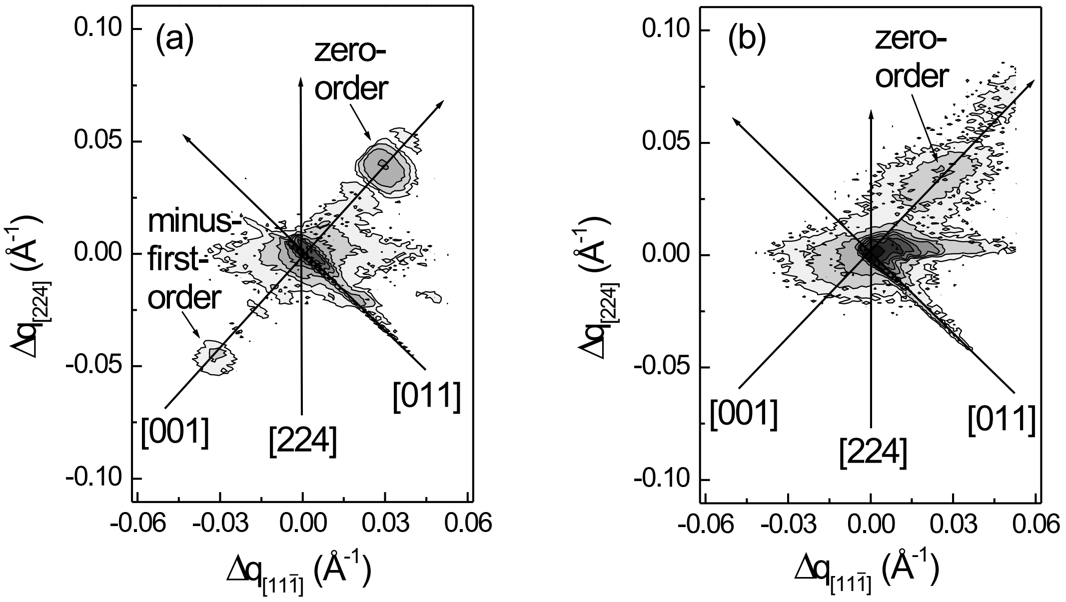

Figure 3.11: RSM around the (224) reciprocal lattice point of the smooth (a) and rough (b) Ga(As,N) sample with 7.4% nitrogen (sample 1 and 2 ind figure 3.9). Even in case of the rough sample, the zero-order satellite peak is aligned in the [001] direction, indicating no change of the in-plane lattice constant.

– the zero-order satellite peak lies in the [001] direction hinting at the absence of misfit dislocations in the rough sample. Therefore, we conclude that the roughening of Ga(As,N)/GaAs MQWs is not mediated by a creation of misfit dislocations.

Roughening processes in Ga(As,N) have also been investigated by other authors. Suemune *et al.* [62, 63] report on roughening of Ga(As,N) samples examined by means of RSM and AFM. According to their investigations on Ga(As,N) with nitrogen concentrations between 2 – 5%, a formation of a wire-like structure is observed when a certain thickness is exceeded. Similar results, a transition from two-dimensional to three-dimensional growth with higher nitrogen concentration in Ga(As,N), are also reported by Adamcyk *et al.* [41, 64]. In their TEM images, no misfit dislocations but threading dislocations were discerned.

Summary Growing Ga(As,N)/GaAs MQWs above a certain thickness leads to a roughening of the samples. The roughening thickness has been investigated by means of RHEED, XRD, AFM, TEM, and RSM measurements. It values 17 nm in case of 4% nitrogen and 3 nm in case of 7.4% nitrogen. TEM images show that there are regions of higher nitrogen concentrations within the Ga(As,N) layers. According to TEM and RSM measurements, one can conclude the absence of misfit dislocation. Thus, the roughening is not mediated by a formation of misfit dislocations.

3.3 Rapid Thermal Annealing of Ga(As,N)

A major drawback of the nitrogen incorporation into GaAs is the high concentration of defects. These defects diminish the PL intensity. One can reduce the concentration of these defects by operating the plasma source at low power and low nitrogen flow. As an alternative, RTA heals out these defects which leads to a substantial increase of the PL intensity. Therefore, this section deals with the optimization of RTA parameters with respect to increasing the PL intensity of Ga(As,N), as well as analyzing the nature of these defects.

Optimization of RTA parameters The optimization of RTA processes is a complex issue by virtue of numerous RTA parameters, such as the (maximum) RTA temperature, the RTA time, the temperature ramp, and the atmosphere in which the RTA processes are accomplished. In this work, Ga(As,N) samples have been annealed under a nitrogen atmosphere with a constant temperature ramp of 20°C/s. Regarding the RTA time, values reported in the literature vary remarkably. Some authors report on annealing at low temperatures for long times between 10 – 60 minutes[52, 65, 66, 67, 68, 69, 70, 71, 72, 73], whereas other authors anneal at high temperatures for very short times between 10 seconds and 3 minutes[17, 74, 75, 76, 77, 78, 79, 80, 81, 82, 83]. Some authors claim that annealing Ga(As,N) samples at high temperatures for long times yields the same results as annealing at low temperatures for short times[33, 84, 85]. From the analysis of a set of at different times annealed Ga(As,N) samples in a range from 30 s to 240 s with RTA temperatures ranging from 650°C to 900°C, the annealing time does not have a major impact on enhancing optical properties. We have found that an annealing time of 60 s causes the most substantial increase of the PL intensity. Thus, samples presented in this work have been annealed for 60 s. Consequently, the only remaining, most crucial parameter is the RTA temperature.

Figure 3.12 shows PL spectra of a 10-period (10/20) nm Ga(As,N)/GaAs MQW sample with 1% nitrogen, as-grown and at different temperatures from 650°C to 950°C annealed (sample 2 in figure 3.13). No PL signal is observed from the as-grown sample, whereas the annealed samples emit a PL signal. For these samples, one can see a tremendous blueshift with higher RTA temperature. Moreover, for the samples annealed at low RTA temperatures, the spectral position of the PL signal lies in the band gap, originating from growth-induced defects. These defects serve as radiative recombination centers. The blueshift hints at a gradual removal of these defects. With a lower defect density, energy states related to these defects are saturated and higher lying states are occupied. Apart from that, there is a substantial increase of the PL intensity by more than one order of magnitude with higher RTA temperature which is seen in the inset of figure 3.12. Again, this phenomenon can be explained with a removal of growth-induced defects that also serve as nonradiative recombination centers. On the contrary, at RTA temperatures above 800°C, there is a decrease of the PL intensity. This degradation occurs, albeit the PL spectra still shift to higher energies. Evidently, there are two different mechanisms induced by RTA. First, there is a removal of growth-induced defects at lower temperatures indicated by a blueshift and an increase of the PL intensity. Second, there is an RTA-induced creation of defects at higher temperatures that is manifested by a diminishing of the PL intensity. The nature

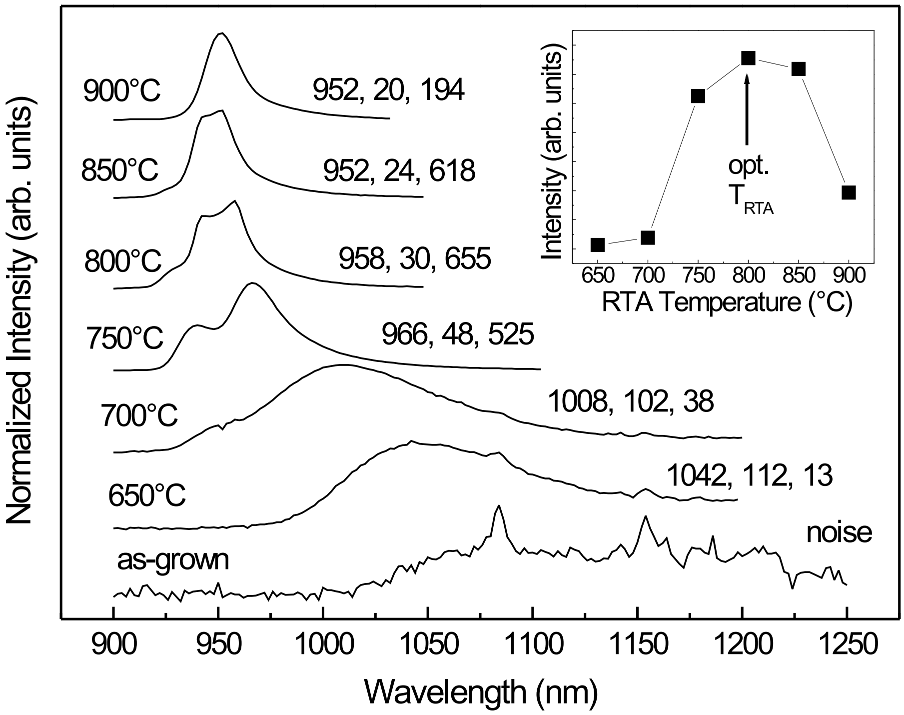

Figure 3.12: PL spectra of a 10-period (10/20) nm Ga(As,N)/GaAs MQW sample with 1% nitrogen annealed at different RTA temperatures for 60 s (sample 2 in figure 3.13). The numbers refer to the spectral position of the PL signal, the FWHM value, and the relative PL intensity. The inset shows the relative PL intensity with respect to the RTA temperature. PL measurements were carried out at 10 K.

of growth-induced and RTA-induced defects will be discussed in the next paragraphs. In case of Ga(As,N) with 1% nitrogen, the highest PL intensity is obtained from the sample annealed at a temperature of 800°C that is now defined as the optimum annealing temperature.

Interestingly, the optimum annealing temperature is not a constant but nitrogen concentration dependent. Figure 3.13 shows the correlation of the optimum annealing temperature with respect to the nitrogen concentration deduced from the analysis of fifteen Ga(As,N) samples. Two types of samples have been analyzed. The samples consist of either 100 nm Ga(As,N) capped with 50 nm GaAs or comprise a 10-period $(d, 2d)$ MQW structure capped with 20 nm GaAs. All samples have been annealed at various RTA temperatures in 50°C steps. From the PL intensity, the optimum annealing temperature is determined. One can clearly see a sizeable decrease of the optimum annealing temperature with higher nitrogen concentration. Moreover, two different regimes are ascertained. From 0.06 – 1.6% nitrogen, the optimum annealing temperature declines drastically from 1000°C to 750°C. For higher nitrogen concentrations, it levels off at 750°C. Besides, for the optimum annealing conditions, there is a decrease of the PL intensity by two orders of magnitude for samples with higher nitrogen concentrations. This can be understood in terms of the two aforementioned competing mechanisms. Presumably, the creation of RTA-induced defects is nitrogen concentration-dependent and occurs at lower temperatures for high nitrogen concentrations. Consequently, one can explain the lower PL intensity with higher nitrogen

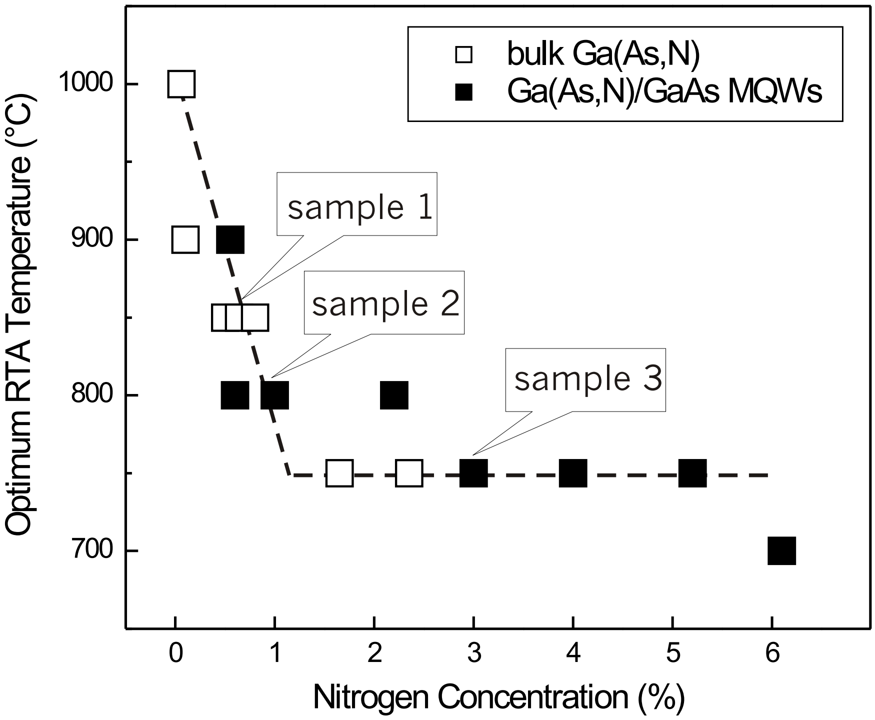

Figure 3.13: The optimum RTA temperature in dependence of the nitrogen concentration. The optimum RTA temperatures represents the temperature that yields the highest PL intensity. All PL measurements were carried out at 10 K.

concentrations: the process of RTA-induced creation of defects takes over the mechanism of the removal of growth-induced defects by RTA before the Ga(As,N) samples are healed out completely.

Growth-induced defects Many authors claim a plasma source-induced generation of ions that cause the above-postulated growth-induced defects[42, 86, 87, 88]. To investigate this issue, the influence of a magnetic field upon the growth of Ga(As,N) has been investigated. Several Ga(As,N) samples were grown with a permanent magnet mounted at different external positions of the MBE system in the vicinity of the plasma source. The strength of the permanent magnet – measured by means of a Hall probe – has a maximum value of 0.07 mT at a distance of 10 cm. Figure 3.14 (a) shows PL spectra of as-grown Ga(As,N)/GaAs MQWs with a permanent magnet mounted at different positions. For all the as-grown Ga(As,N) samples that were grown in an external magnetic field, we observe a substantial increase of the PL intensity. Moreover, the PL signal is blueshifted closer to where the band gap is expected. Consequently, we conclude a lower density of growth-induced defects in the Ga(As,N) sample grown in a magnetic field. Hence, these observations hint at the existence of ions generated by the plasma source which cause ion-induced point defects, such as gallium or arsenic vacancies (see next paragraphs). A magnetic field deflects these ions causing a lower rate of ionized nitrogen that impinges on the sample surface. Consequently, the concentration of ion-induced point defects is diminished, resulting in an increase of the PL intensity. Figure 3.14 (b) shows the RTA temperature dependence of the Ga(As,N)

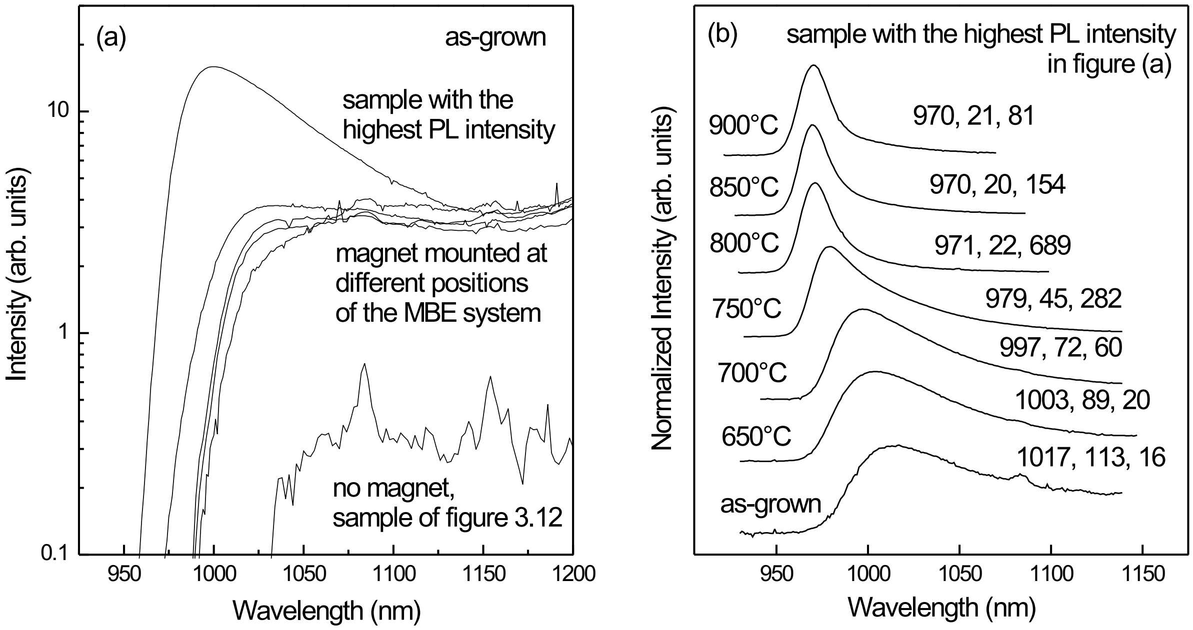

Figure 3.14: (a) PL spectra of as-grown Ga(As,N) samples without and with a permanent magnet mounted at different positions of the MBE system. (b) RTA temperature-dependent PL of sample that shows the highest PL intensity in figure (a). The numbers refer to the wavelength, FWHM value, and the intensity. PL measurements were carried out at 10 K.

sample that shows the highest PL intensity in figure 3.14 (a). Univocally, there is a sizable increase of the PL intensity for higher RTA temperatures. Thus, growth-induced defects are still prevalent in this sample. Hence, even for Ga(As,N) grown with a magnetic field applied, RTA is mandatory to improve optical properties. The comparison with figure 3.12 shows that the optimum RTA temperature of both samples amounts to 800°C, whereas no major change of the PL intensity is observed at these RTA conditions. We assume that the influence of the external magnetic field upon the ion-induced point defect concentration is rather low – having a pronounced effect upon the as-grown sample, only. Solely a small portion of the plasma source-generated ions are deflected by the magnet. One might think of avoiding a post-growth thermal treatment on Ga(As,N) by applying a magnetic field strong enough to deflect all ions generated by the plasma source. Unfortunately, the interaction between the electromagnetic radiation coupled into the plasma source cavity and the external magnetic field has an adverse effect upon the plasma source functionality. Thus, we were not able of run the plasma source with a magnetic field that is strong enough to deflect all ions. RTA is therefore indispensable to remove the ion-induced point defects even when a magnetic field is applied.

As a lowering of the plasma source power and nitrogen flow also leads to an improvement of optical properties [cf. figure 3.5 (b)], we assume a correlation between the plasma source parameters and the amount of ions generated by the plasma source: there is a reduction of the ion concentration by lowering the plasma source power and nitrogen flow. The same finding has been reported by Carrère *et al.* [89] who investigated the plasma source characteristics for different nitrogen flows and plasma source powers. According to their work, the amount of ionized nitrogen increases with higher

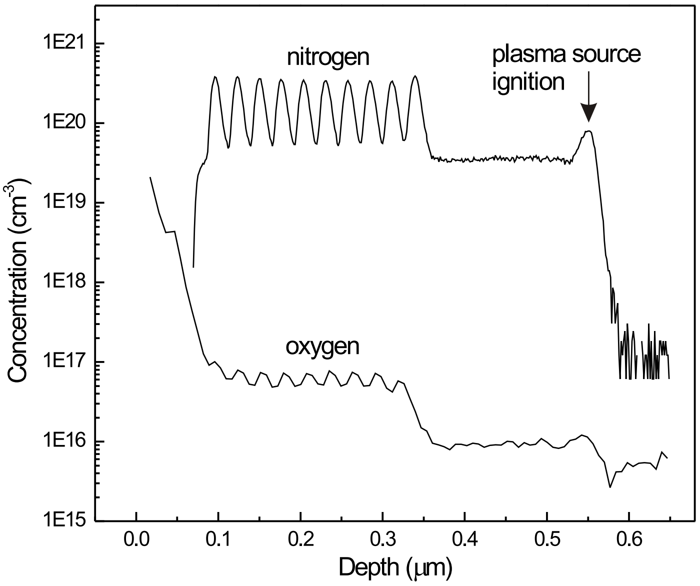

Figure 3.15: Nitrogen and oxygen SIMS profile of a Ga(As,N)/GaAs MQW sample (sample 3 in figure 3.13). The sample consists of a 10-period (10/20) nm Ga(As,N)/GaAs MQW structure with 3% nitrogen.

plasma power and higher nitrogen flow. In addition, Carrère *et al.* report on oxygen incorporation into Ga(As,N). Such impurities may originate from the residual gas in the nitrogen bottle. Oxygen impurities serve as nonradiative recombination centers that deteriorate optical properties[90, 91, 92]. Such nonradiative recombination centers degrade the performance of lasers diodes[93]. Figure 3.15 shows a secondary ion mass spectrometry (SIMS) nitrogen and oxygen concentration profile of a 10-period Ga(As,N)/GaAs MQW sample (sample 3 in figure 3.13). Indeed, there is a higher oxygen concentration when the nitrogen plasma source is in use. The oxygen concentration increases from 5×10^{15} cm^{-3} to 6×10^{16} cm^{-3}. Hence, the deterioration of optical properties is attributed to two different kinds of defects: ion-induced point defects and oxygen.

Figure 3.16 (a) shows two Raman spectra of a Ga(As,N)/GaAs MQW with 3% nitrogen (sample 3 in figure 3.13). The upper spectrum stands for the as-grown sample, whereas the lower spectrum represents the sample annealed at 850°C for 60 s. In case of the as-grown sample, there are two local vibrational modes (LVMs) at 409 and 427 cm^{-1}. These LVMs do not appear in the spectrum of the at 850°C annealed sample. Figure 3.16 (b) shows the integrated intensities of these Raman lines with respect to the annealing temperature. Obviously, there is a smooth decrease of these Raman lines with higher RTA temperatures. In addition, the PL intensities are depicted in this figure. Interestingly, the intensities of the two Raman lines start to decline as the PL intensity begins to ascend. The same observations have been reported by Ramsteiner *et al.* [94]. The authors attribute these LVMs to nitrogen split interstitials in Ga(As,N) that are incorporated into gallium and arsenic vacancies . These split interstitials serve as nonradiative recombination centers and are removed during the annealing procedure. The presence of gallium and arsenic vacancies is possibly related to ion-induced defects created by the plasma source.

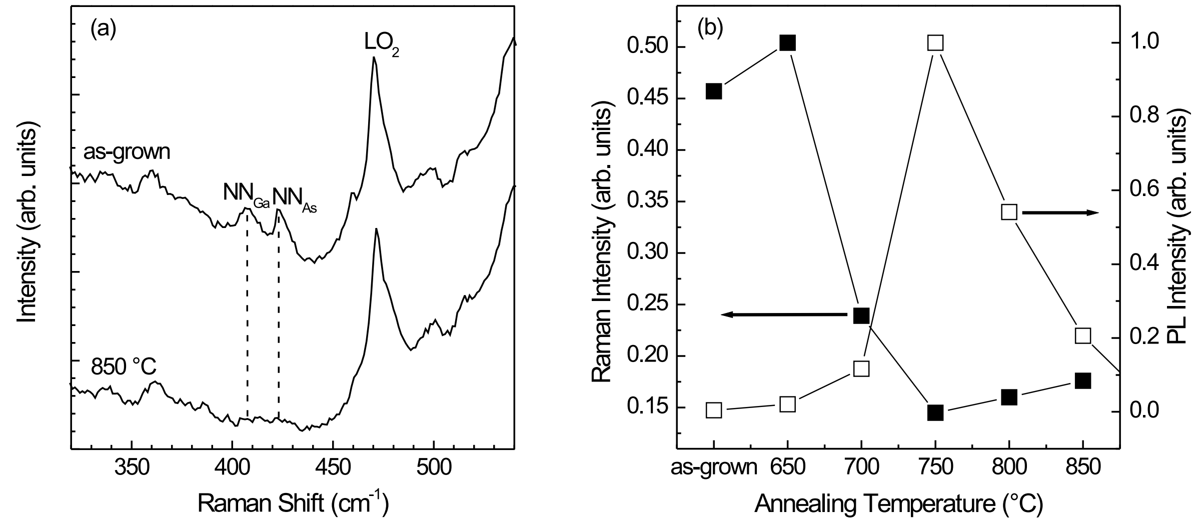

Figure 3.16: Raman spectra of the as-grown and annealed Ga(As,N)/GaAs MQW sample with 3% nitrogen (sample 3 in figure 3.13) (a). Integrated intensities of the two vibrational modes with respect to the RTA temperature (b). In addition, the PL intensities are plotted. (Raman spectra taken by M. Ramsteiner.)

Point defects in Ga(As,N) have also been reported by several authors. For example, Toivonen *et al.* have detected gallium vacancies in Ga(As,N) by means of nuclear reaction analysis[95]. According to the authors, a thermal treatment reduces the concentration of these vacancies. Ahlgren *et al.* employed positron annihilation spectroscopy to detect interstitial nitrogen in Ga(As,N)[96]. The same finding has been reported by Spruytte *et al.*, based upon combined channeling and nuclear reaction analysis measurements[32, 33]. The authors state a deviation of Vegard's law owing to the existence of these point defects. Point defects, detected by means of deep level transient spectroscopy, have also been reported by Krispin *et al.* [97, 98]. The authors state the existence of N-N and N-As split interstitials. A thermal treatment removes the N-N split interstitials – in concordance to the above-presented results.

RTA-induced defects Figure 3.17 shows XRD curves of the as-grown and annealed Ga(As,N) sample with 3% nitrogen (sample 3 in figure 3.13). One can clearly see a transition towards broadened satellite peaks with higher RTA temperature. In case of the as-grown sample, narrow satellite peaks as well as pendellösung fringes are discernable, indicating smooth Ga(As,N)/GaAs interfaces. The lowest curve in figure 3.17 represents the simulation. At the optimum temperature of 750°C (cf. figure 3.13), one can still observe pendellösung fringes, albeit the satellite peaks appear to be slightly broadened. For the sample annealed at 900°C, the satellite peaks are substantially broadened without the presence of pendellösung fringes. Apparently, there is a structural degradation of Ga(As,N) samples caused by RTA. Nevertheless, the intensities of the satellite peaks remain constant. Thus, there is no change of the XRD envelope function. Consequently, as discussed in section 2.2, we assume no pronounced nitrogen diffusion in the Ga(As,N) samples during the annealing process.
To obtain further insight about the issue of a nitrogen diffusion, the composition profiles of nitrogen were determined along the growth direction by a quantitative analysis

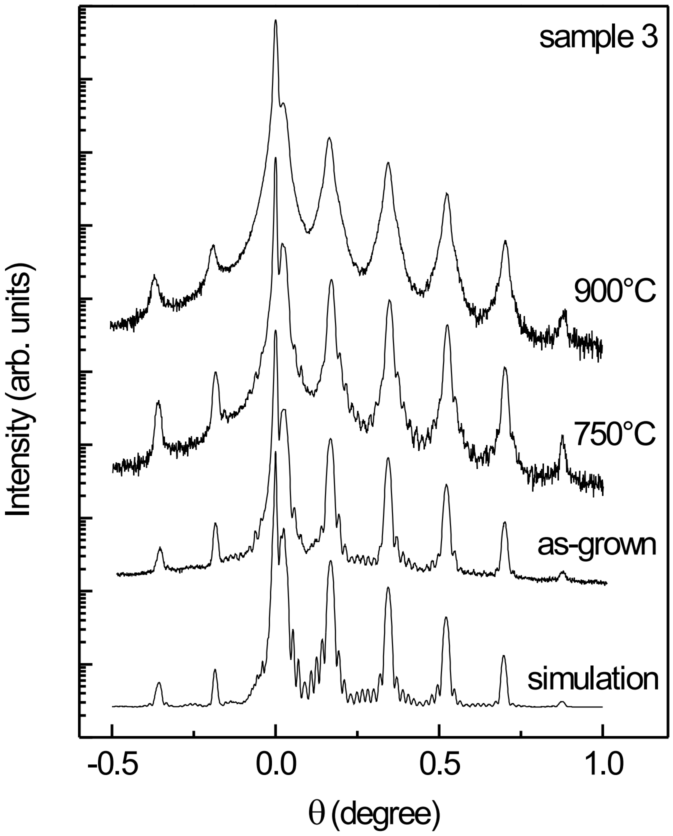

Figure 3.17: (004) XRD curves of the as-grown and annealed Ga(As,N)/GaAs MQW sample with 3% nitrogen (sample 3 in figure 3.13)

of the (002) TEM dark-field contrast. Figure 3.18 shows (002) dark-field TEM images of the as-grown (a) and annealed (b) Ga(As,N) sample with 3% nitrogen (sample 3 in figure 3.13). The contrast observed in the micrographs is directly related to the chemical composition[99]. The Ga(As,N) QWs exhibit a lower intensity (dark bands) than the GaAs barriers (bright contrast). For the as-grown sample, one can clearly discern abrupt Ga(As,N)/GaAs interfaces, confirming the good structural quality detected by XRD. However, even after annealing at 900°C [figure 3.18 (b)], the QWs appear to have smooth Ga(As,N)/GaAs interfaces. In order to quantify the nitrogen concentration profiles across the QW, the measured intensity was averaged on a lateral length of 100 nm and normalized to the intensity of the GaAs barriers. The residual nitrogen concentration in the barriers – caused by nitrogen incorporation even when the shutter is closed (cf. figure 3.6) – was given by complementary SIMS experiments (figure 3.15). The nitrogen profiles are shown in figure 3.18 (c). Indeed, a nitrogen interdiffusion occurs in the annealed sample. This clearly leads to a more gaussian-like profile. Nevertheless, the maximum broadening of the interfaces is limited to $\sim$ 2 nm, even at this high annealing temperature[3]. Consequently, we cannot ascribe the structural degradation solely to nitrogen diffusion processes out of the Ga(As,N) QWs.

However, extended defects were observed in the annealed sample. Apart from the

---

[3] The maximum broadening was determined by measuring the FWHM values of the as-grown and annealed Ga(As,N) QW composition profiles.

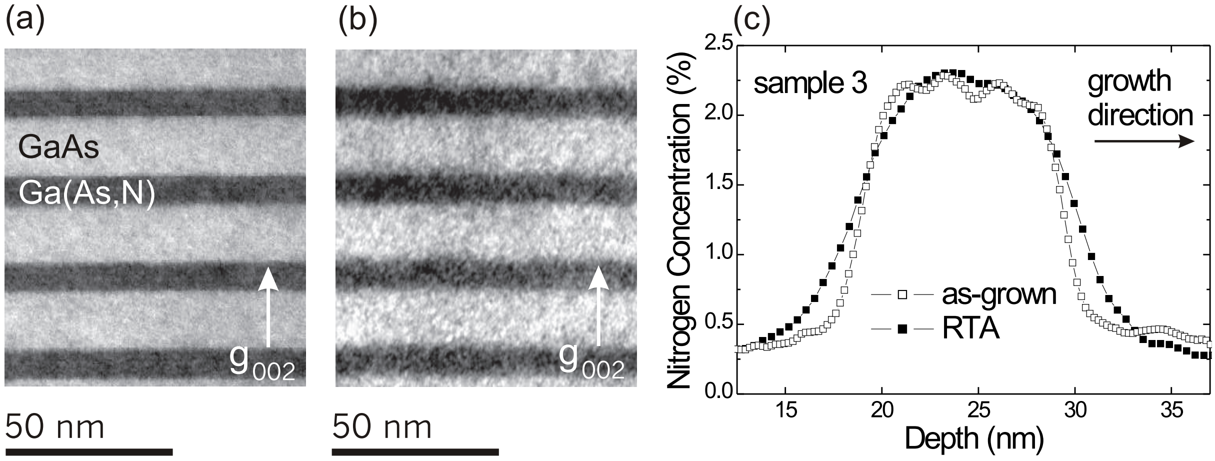

Figure 3.18: (002) TEM images of the as-grown (a) and annealed (b) Ga(As,N)/GaAs MQW sample with 3% nitrogen (sample 3 in figure 3.13). Nitrogen profiles of the as-grown and annealed sample derived from the TEM images (c). (TEM taken by A. Trampert.)

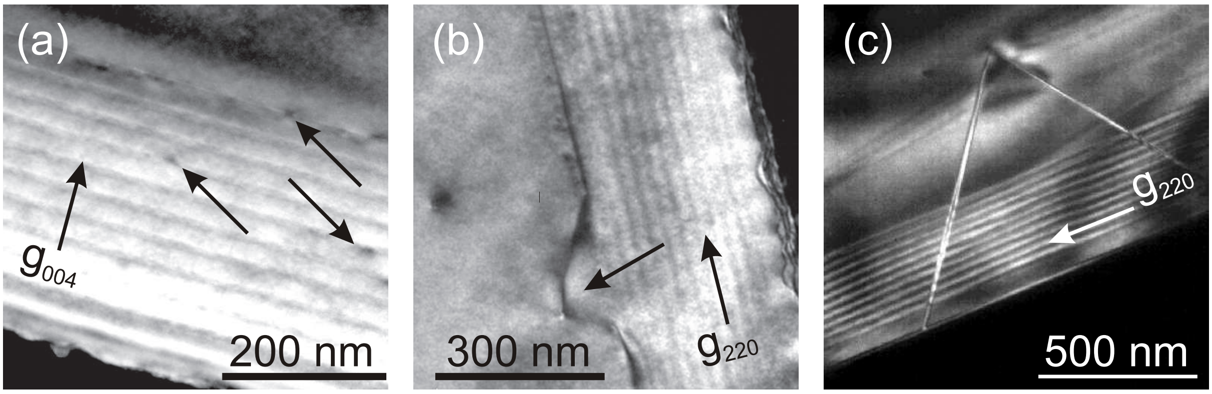

Figure 3.19: (004) and (220) TEM images of the at 900°C annealed Ga(As,N) sample (sample 3 in figure 3.13). Figure (a) shows lateral changes within the Ga(As,N) QW, denoted by the arrows. Figure (b) displays a dislocation induced by the thermal treatment. In figure (c), stacking faults are seen. (TEM taken by A. Trampert.)

composition-sensitive (002) TEM dark-field contrast, strain-sensitive (004) and (220) dark-field TEM has been performed. Figure 3.19 shows (004) and (220) dark-field TEM images of the at 900°C annealed sample. Apparently, lateral changes within the Ga(As,N) QWs are discernable in figure 3.19 (a) that are attributed to the annealing process. In addition, figure 3.19 (b) shows a dislocation that is induced by the thermal treatment procedure. Figure 3.19 (c) depicts stacking faults. These extended defects cause a further structural degradation that may be deemed an explanation of the satellite peak broadening in the XRD curves as well as the diminishing of the PL intensity for high RTA temperatures. They may also explain the correlation of the optimum RTA temperature with respect to the nitrogen concentration in figure 3.13: the formation of extended defects depends upon the point defects concentration. An accumulation of point defects promotes the formation of extended defects. Increasing the nitrogen concentration leads to a higher concentration of point defects in Ga(As,N). Consequently, the formation of extended defects occurs at lower RTA temperatures for Ga(As,N) with high nitrogen concentrations. This leads to a reduction of the optimum RTA temperature with higher nitrogen concentrations.

Summary Rapid thermal annealing is essential to improve the optical properties of Ga(As,N). RTA heals out growth-induced defects that leads to a blueshift of the PL spectra and a sizeable increase of the PL intensity. Growth-induced defects may be ion-induced point defects created by the plasma source, nitrogen split interstitials, and oxygen. Annealing at very high RTA temperatures results in a decrease of the PL intensity due to RTA-induced creation of defects, such as lateral changes within Ga(As,N), dislocations, and stacking faults. The optimum RTA temperature is nitrogen concentration-dependent and decreases with higher nitrogen concentrations.

3.4 Analysis of Radiative Recombination in Ga(As,N)

In the previous section, the optimization of RTA parameters to enhance optical properties and the origin of growth-induced and RTA-induced defects have been discussed. For accomplishing light emitting devices, it is important to understand the nature of radiative recombination, such as PL related to growth-induced defects versus band edge transitions or the recombination via spatially localized and delocalized excitons. Thus, this section is attributed to analyze the nature of radiative recombination in Ga(As,N).

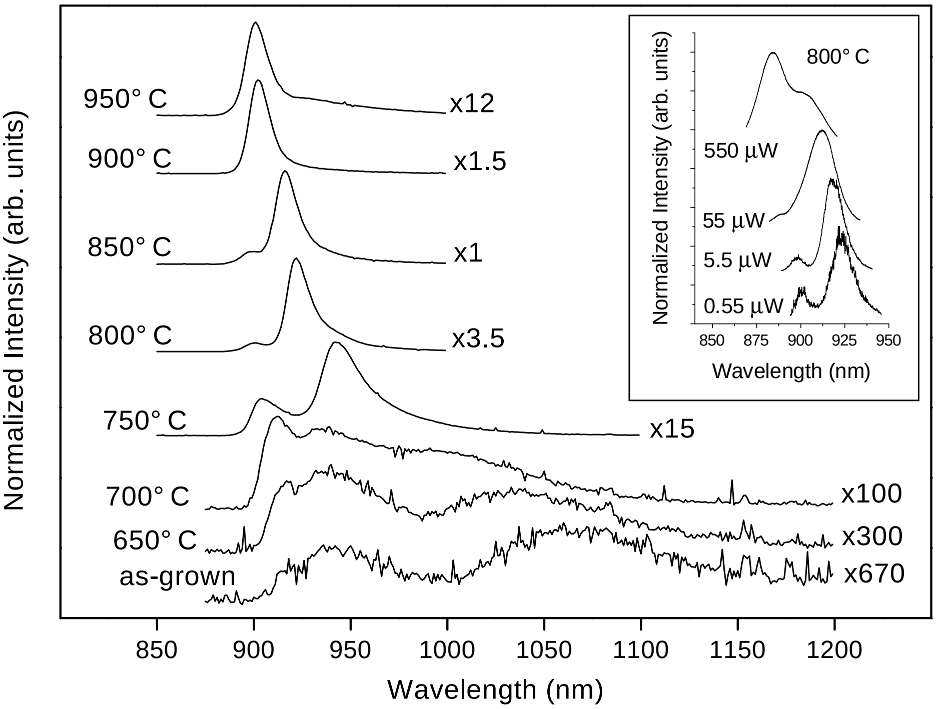

Figure 3.20: Cw-PL of a Ga(As,N) sample with 0.5% nitrogen (sample 1 in figure 3.13), annealed at different temperatures. The inset shows excitation density-dependent PL spectra of the sample annealed at 800°C. All PL measurements were carried out at 10 K.

For this analysis, a single Ga(As,N) sample with 0.5% nitrogen has been investigated by means of continuous-wave photoluminescence (cw-PL), μPL, and TR-PL (sample 1 in figure 3.13). The sample has been cleaved into several pieces for subsequent annealing processes. The annealing temperature was varied in between 650°C and 950°C. Prior to annealing, XRD has been performed to assure a homogeneous nitrogen concentration of all pieces. Figure 3.20 shows cw-PL spectra of this sample annealed at different temperatures. One can clearly see a blueshift and an increase of the PL intensity that can be elucidated with a removal of growth-induced defects (see section 3.3). For the sake of brevity, these growth-induced defects are henceforth called defects in this section. The inset in figure 3.20 shows PL spectra of the sample annealed at 800°C with excitation densities ranging over 3 orders of magnitude. A blueshift occurs for higher excitation densities owing to a saturation of these defects-related states. As the position of the PL maxima remains unchanged for the samples annealed at high temperatures (900°C, 950°C), one can assume that these samples are healed out completely. However, the PL maxima of these samples are still slightly lower in energy than the band gap, which lies at 896 nm according to equation 2.1. This is possibly due to the existence of potential fluctuations in Ga(As,N) which will be considered in section 3.5.

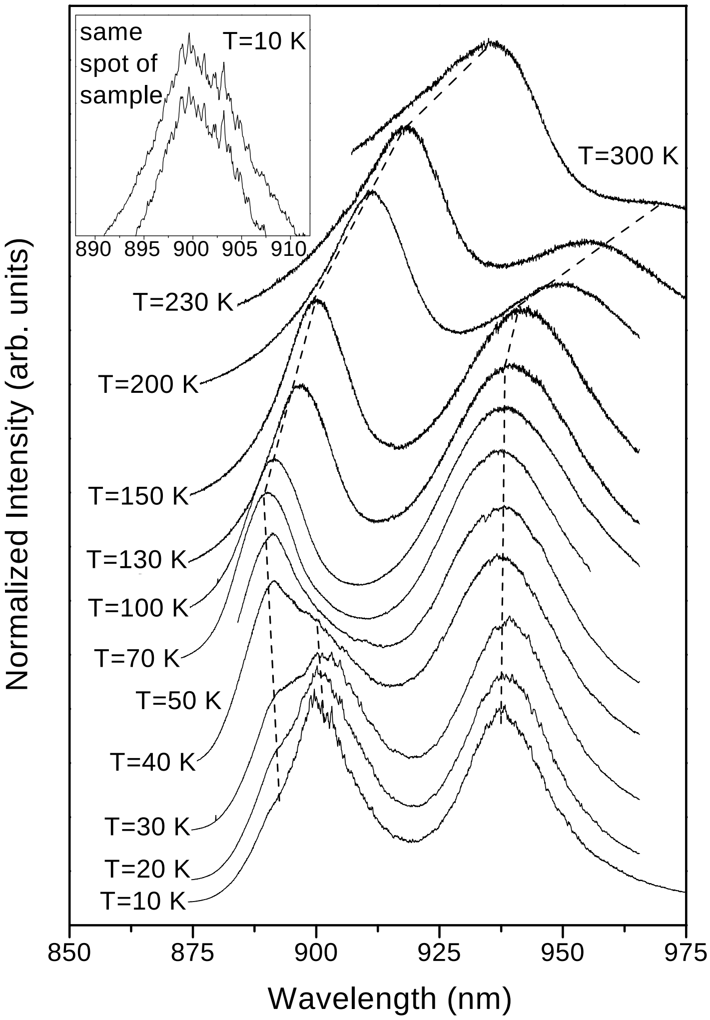

Figure 3.21: Temperature-dependent μPL of the Ga(As,N) sample annealed at 800°C. The spatial resolution amounts to 1 μm in diameter. The inset shows two PL spectra of the same spot.

To get further insight into the nature of radiative recombination, μPL has been employed. In μPL setups, the laser beam is focused onto a very small area, typically 1 μm in diameter. Thus, one can investigate the microscopic structure of samples, e.g. distinguishing between spatially localized and delocalized excitons. As discussed in section 2.1, localized excitons, such as excitons trapped in potential fluctuations or defects, are characterized by ultranarrow spikes with linewidths less than 0.1 nm[100, 101, 102]. Thus, by employing μPL, one can distinguish between band edge transitions (delocalized excitons) and radiative recombination via defects or potential fluctuations (localized excitons). Figure 3.21 shows temperature-dependent μPL of the sample annealed at 750°C (cf. figure 3.20). A pronounced double peak feature is seen. At low temperatures (10 K), ultranarrow spikes are prevalent in both peaks which clearly identify the localized nature of these excitons. The inset in figure 3.21 shows two subsequently

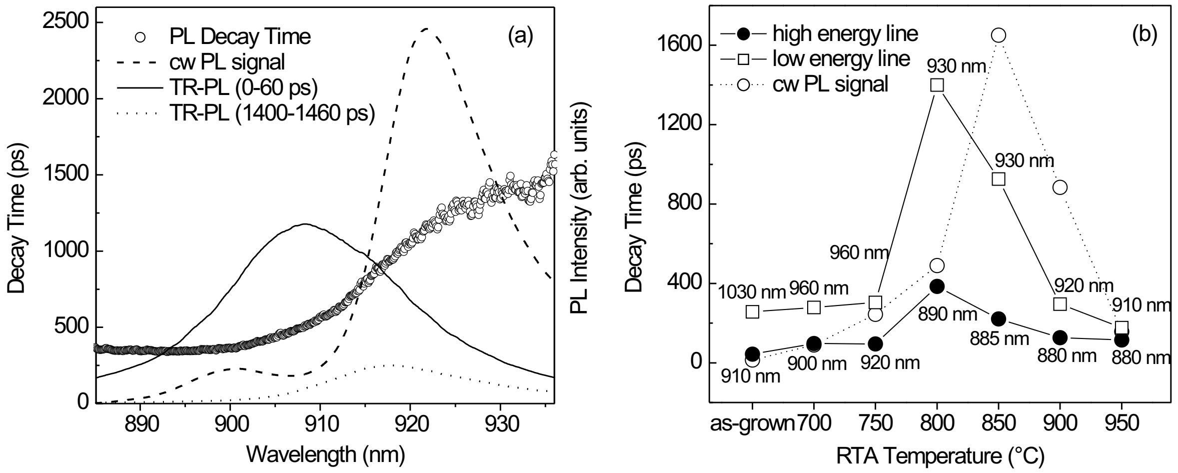

Figure 3.22: The spectral dependence of the decay time concerning the Ga(As,N) sample annealed at 800°C (a). The transient spectra between 0 – 60 ps (solid line) and 1400 – 1600 ps (dotted line) are displayed (a). In addition, the cw-PL intensity is plotted (dashed line). The open circles show the spectral dependence of the decay time. Figure (b) depicts the decay times on the high- and low-energy side with respect to the annealing temperature. The numbers denote the wavelength for which the decay times were ascertained. The open circles stand for the cw-PL intensity (cf. figure 3.20). All measurements were accomplished at 10 K. (TR-PL measurements accomplished by V. Talalaev.)

measured PL spectra of the same spot of the sample. Apparently, these ultranarrow spikes are reproducible, thus arising from the sample. Therefore, we assume these excitons to be localized, either trapped in potential fluctuations or by defects. Possibly, the high-energy peak is related to potential fluctuations, whereas the low-energy peak is related to defects. At slightly higher temperatures (20 K – 40 K), there is a third peak emerging at the high energy side that does not contain any ultranarrow spikes. Apparently, these excitons are spatially delocalized and result from a thermal activation of excitons out of these potential fluctuations. This peak becomes dominant with higher temperatures and illustrates the transition from localized to delocalized excitons. The blueshift of this peak that continues up to 70 K mirrors the thermal activation process out of these potential fluctuations. For higher temperatures (70 K – 300 K), this peak redshifts due to the normal temperature dependence of the band gap[103]. The low-energy peak also loses its ultranarrow spikes with higher temperatures. This is likely to be caused by an energy band formed by these defects. Thus, these defects get activated by thermal emission, too, leaving defect-related states and becoming freely moving within this band. At ambient temperature, this peak vanishes because of a thermal activation of these excitons out of this defect-related band.

Furthermore, the existence of localized and delocalized excitons can be corroborated by means of TR-PL measurements. As depicted in section 2.1, spatially localized excitons are characterized by long decay times, typically in the nanosecond range. On the contrary, delocalized excitons show short decay times in the picosecond range. In addition, defect-related nonradiative recombination channels expedite decay processes. Figure 3.22 (a) shows the spectral-dependent decay time of the sample annealed at 800°C (open circles). Apparently, there is a correlation between wavelength and decay time with short decay times on the high-energy side and long decay times on the low-energy side. Again, this can be understood in terms of a transition from localized to delocalized excitons. On the low-energy side, excitons are localized in potential fluctuations, thus having long decay times. On the high energy side, excitons are delocalized showing short decay times. Figure 3.22 (b) shows the decay times of all annealed samples. The samples that are annealed at low temperatures show short decay times, even though radiative recombination is defect-related and therefore occurs via localized excitons. Nonetheless, there are defect-induced nonradiative recombination channels that accelerate recombination processes. With higher RTA temperatures, there is a removal of defects, thus reducing the impact of the nonradiative recombination channels. Consequently, the decay time increases, as it is seen in the sample annealed at 800°C. At RTA temperatures above 800°C, there is a transition from localized to delocalized excitons which causes a decrease of the decay time. At very high RTA temperatures, RTA-induced defects might serve as nonradiative recombination channels that cause a further reduction of the decay time.

Summary Radiative recombination in Ga(As,N) occurs via spatially localized or delocalized excitons. Localized excitons are either trapped in potential fluctuations or defects. Even in healed out samples, excitons are still localized in potential fluctuations. An increase of temperature and/or excitation density leads to a transition from localized to delocalized excitons.

3.5 Potential Fluctuations in Ga(As,N)

In the previous section, the nature of radiative recombination in Ga(As,N) has been investigated. Experimental results give clear indication of excitons localized in potential fluctuations of healed out Ga(As,N) samples. This section is dedicated to investigate properties of potential fluctuations in Ga(As,N), such as its density as well as the spatial and spectral distribution.

Potential Fluctuations The optimization of the Ga(As,N) growth has been discussed in section 3.1. However, even for Ga(As,N) samples grown at optimized growth conditions, there are slight spatial inhomogeneities of the nitrogen concentration. As already mentioned, the incorporation of nitrogen causes a tremendous decrease of the band gap. Consequently, slight deviations from the nominal nitrogen concentration cause dips in the band alignment, so called potential fluctuations. These potential fluctuations are expected to have a spatial extent of 10 – 20 nm[101, 102]. Excitons trapped in these potential fluctuations are spatially localized, showing ultranarrow spikes if the spatial resolution is high enough. SNOM setups may achieve a spatial resolution of 200 nm – sufficient to resolve these ultranarrow spikes. Thus, the analysis of SNOM spectra gives valuable information on potential fluctuations.

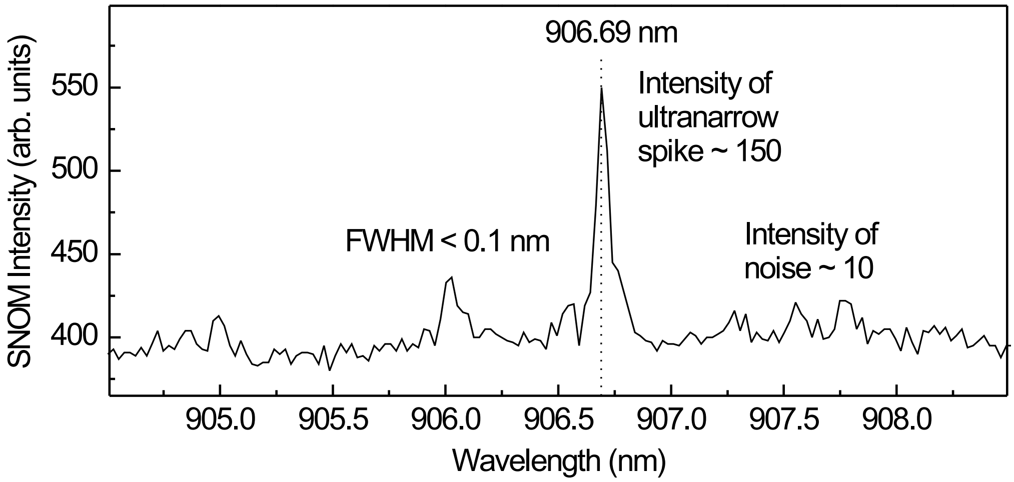

Figure 3.23: SNOM spectrum of the Ga(As,N) sample with 0.5% nitrogen (sample 1 in figure 3.13). The measurement was accomplished at 10 K. (SNOM spectra taken by V. Malyarchuk.)

SNOM Area Scans For this analysis, a SNOM area scan of the 100 nm Ga(As,N) sample with 0.5% nitrogen annealed at 900°C for 60 s has been accomplished (sample 1 in figure 3.13). We assume this sample is healed out from growth-induced defects as there is no blueshift for higher RTA temperatures (see figure 3.20). The area scan comprises 30×30 spectra with a spatial difference of 20 nm. Figure 3.23 shows a SNOM spectrum taken from the area scan. An ultranarrow spike is observed indicating radiative recombination from localized excitons. As the spatial resolution of the SNOM setup is a factor 10 lower than the distance between neighboring spectra, this ultranarrow spike also appears in the neighboring spectra. Its intensity amounts to 150 with respect to the

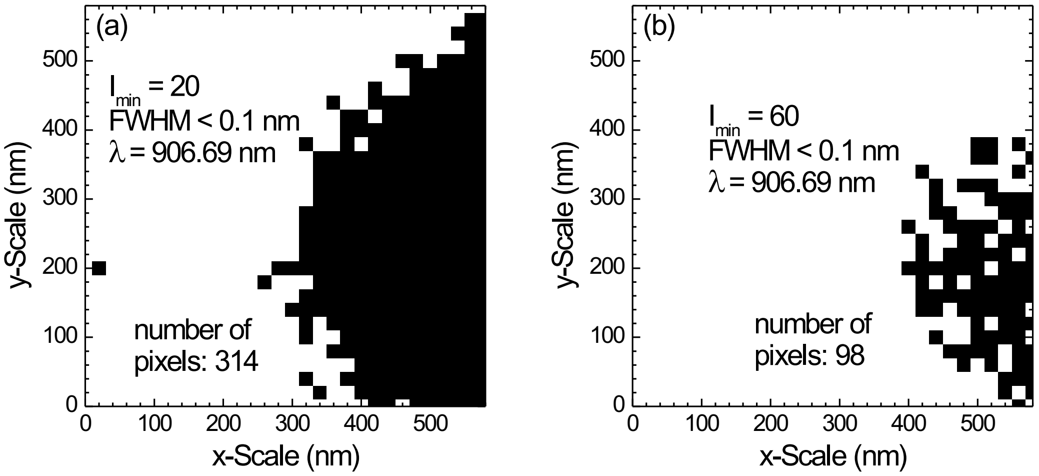

Figure 3.24: Two x-y plots of the ultranarrow spike at 906.69 nm. The black pixel stand for the spectra where this ultranarrow spike appears; the white pixels represent the spectra that do not contain this ultranarrow spike. In figure (a), the minimum intensity to detect an ultranarrow spike amounts to 20; in figure (b) it values 60.

background, whereas the intensity of noise – relative to the background – has a value of approximately 10. The FWHM value of ultranarrow spikes is less than 0.1 nm.

Discussion In order to gain information about potential fluctuations, one can create x-y-plots of a particular ultranarrow spike. Figure 3.24 (a) and (b) show x-y-plots of the ultranarrow spike at a fixed wavelength of 906.69 nm (cf. figure 3.23). The black pixels in the x-y-plots stand for spectra that contain the ultranarrow spike at 906.69 nm, whereas the white pixels represent spectra that do not show this particular ultranarrow spike. However, for this analysis, one needs a criterion to define an ultranarrow spike, namely a minimum intensity. Figure 3.24 (a) shows the x-y-plot the ultranarrow spike at 906.69 nm with a minimum intensity of 20. Obviously, there is quite a number of spectra that comprise this particular ultranarrow spike - denoted by the black pixels in the x-y-plot. These black pixels form a cluster that represents a potential fluctuation. Figure 3.24 (b) shows the x-y-plot of the same ultranarrow spike with a minimum intensity of 60. Evidently, this cluster appears smaller with respect to figure 3.24 (a). Nevertheless, it encompasses a large number of pixels. Hence, detecting such cluster is very insensitive to the minimum intensity applied. It is worth noting that the x-y-plots in figure 3.24 (a) and (b) stand for a fixed wavelength of 906.68 nm. An x-y-plot at a wavelength 0.1 nm above or below this particular wavelength does not contain any cluster. Also, one has to keep in mind that such x-y plot does not provide information about the lateral extent of such potential fluctuations. The spatial resolution of the SNOM setup is one order of magnitude lower than the size of potential fluctuations. Thus, these SNOM area scans solely provide information about the spectral distribution and the density of potential fluctuations.

In order to estimate the density of potential fluctuations, one has to determine the number of clusters integrated over all wavelengths from 901 – 934 nm. The underlying assumption is that each cluster represents a potential fluctuation. Nonetheless,

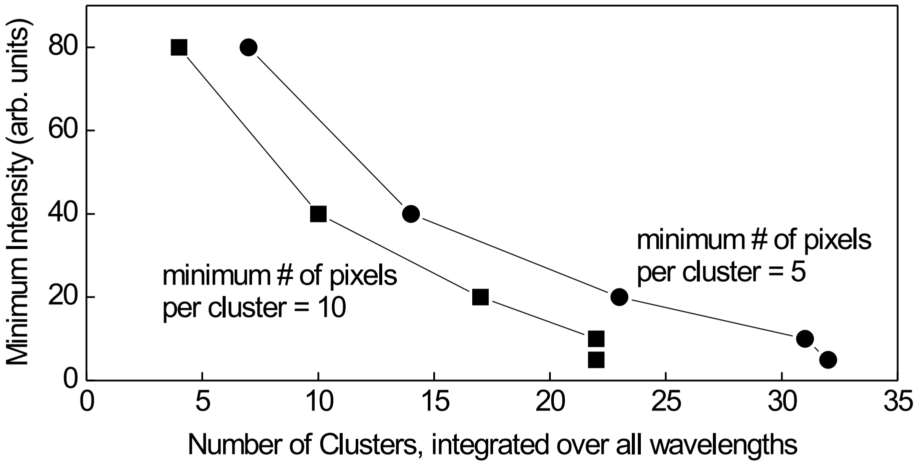

Figure 3.25: Number of clusters, integrated over all wavelengths, with respect to the minimum SNOM intensity for clustersize minima of 5 and 10 pixels.

this analysis depends on the minimum intensity for distinguishing ultranarrow spikes. However, by varying the minimum intensity in a reasonable range, one can obtain an estimate of the number of clusters of the probed area. In order to filter out noise, one can apply a reproducibility test upon the ultranarrow spikes. In case of potential fluctuations, ultranarrow spikes also appear in the neighboring spectra. On the other hand, noise is not reproducible. Therefore, noise-induced ultranarrow spikes do not emerge in neighboring spectra. Consequently, to assure that only potential fluctuation-induced ultranarrow spikes are taken into account, a cluster needs to comprise several neighboring pixels. Figure 3.25 shows the number of clusters, integrated over all wavelengths, with respect to the minimum intensity. The analysis has been accomplished for clustersize minima of 5 and 10 pixels. Apparently, there is an increase of the number of clusters for lower intensity minima. On the other hand, there is a slight decrease of the number of clusters with a higher clustersize minimum. Nonetheless, the number of clusters remains in the same order of magnitude between 5 and 30. In fact, it goes into a saturation for low intensity minima. Thus, the maximum number of clusters in the probed area amounts to approximately 30. With this value, one can draw an estimate of the potential fluctuation density. The lateral extent of the probed area is 0.58×0.58 μm^2; the Ga(As,N) thickness amounts to 0.1 μm. Thus, the volume probed has a value of 0.03 μm^3. As a result, the potential fluctuation density of Ga(As,N) sample with 0.5% nitrogen amounts to approximately 1000 μm^{-3}.

One might think of ultranarrow spikes that stem from the same potential fluctuation by virtue of ground state and first excited state transition. To clear this issue, the CM of each cluster was ascertained. The CM of a cluster refers to the pixels that stands of the spectrum with the highest ultranarrow spike intensity. In case of ground state and first excited state transition, the CM has to have the same spatial position as the emission originates from the same potential fluctuation. However, no spatial overlap of CMs was detected. Therefore, the issue of higher excited state transition can be ruled out. Moreover, the spatial distribution of the detected clusters is entirely random. The clusters are spread throughout the probed area. Regarding the spectral position of the detected clusters, no pronounced trend was discerned. The clusters show a random spectral distribution that represents the integrated SNOM emission. The highest number of potential fluctuations refers to a wavelength of 910 nm. As the band gap is expected to be at 896 nm according to equation 2.1, the potential fluctuations are located approximately 20 meV below the conduction band edge. Hence, employing equation 2.1, one can now calculate the concentration deviation that amounts to approximately 0.1% nitrogen. Concerning a trend of the potential fluctuation density with different nitrogen concentrations, the same analysis has been accomplished on a 100 nm Ga(As,N) sample with 0.1% nitrogen annealed at 900°C for 60 s. Similar results were obtained; the potential fluctuation density amounts to $\sim 1000\ \mu\text{m}^{-3}$. Another question might arise from the FWHM value. So far, the maximum FWHM value for defining an ultranarrow spike was kept constant at 0.1 nm. The analysis shows that increasing the maximum FWHM value to detect an ultranarrow spike yields the same number of clusters in that probed area. Hence, we assume that a FWHM value of 0.1 nm is still too large to describe the linewidths of localized excitons. On the other hand, the spectral resolution of the SNOM setup amounts to 0.025 nm. Thus, a FWHM value of 0.1 nm is in the vicinity of the spectral resolution limit of the SNOM setup.

Summary Potential fluctuations refer to microscopic regions of slightly different nitrogen concentrations. Excitons trapped in potential fluctuations are spatially localized showing ultranarrow spikes in SNOM measurements. Potential fluctuations prevail even in healed out ultradilute Ga(As,N) samples with nitrogen concentration of 0.1 - 0.5%. Its density is estimated $1000\ \mu\text{m}^{-3}$. The spectral distribution of potential fluctuations resembles the integrated SNOM emission. The spatial distribution is completely random.

Chapter 4

(In,Ga)(As,N): Growth and Properties

In the previous chapter, structural and optical properties of the ternary Ga(As,N) material system have been discussed. A strong band gap reduction is achieved by the incorporation of nitrogen into GaAs. Nonetheless, there is a deterioration of structural and optical properties for high nitrogen concentrations. Consequently, it is barely possible to grow Ga(As,N) of high optical quality that emits at 1.3 μm. To solve this problem, one can incorporate indium into Ga(As,N). The aim of adding indium is twofold. First, by virtue of a smaller band gap of InAs with respect to GaAs, the incorporation of indium into Ga(As,N) causes a further band gap reduction. Second, one can control the strain of (In,Ga)(As,N) as the lattice constant of InAs is larger than the one of GaAs, whereas the lattice constant of GaN is smaller with respect to GaAs (cf. figure 2.1). To make use of these advantages, one has to gain knowledge about this quaternary material system. Hence, this chapter is dedicated to growth and properties of (In,Ga)(As,N).

4.1 MBE-Growth of (In,Ga)(As,N)

Optimizing the growth of (In,Ga)(As,N) In section 3.1, the optimization of Ga(As,N) growth has been investigated. Numerous Ga(As,N) samples have been grown with different growth parameters. The samples were subsequently analyzed to optimize the growth with respect to structural and optical properties. We have found that the substrate temperature is the most crucial growth parameter in Ga(As,N). Growing Ga(As,N) at high substrate temperature causes a roughening of surfaces and interfaces by virtue of a large miscibility gap of nitrogen in GaAs. Figure 3.1 refers to Ga(As,N)/GaAs MQWs that were grown at different substrate temperatures and different nitrogen concentrations. The structural quality was assessed by means of in-situ RHEED. In order to investigate the influence of the substrate temperature and the nitrogen incorporation on the quaternary material system, the same procedure has been accomplished on 10-period (7/14) nm (In,Ga)(As,N)/GaAs MQWs with 30% indium. Figure 4.1 illustrates the impact of substrate temperature and nitrogen incorporation upon these (In,Ga)(As,N)/GaAs MQWs. The samples – denoted by blank or filled squares – are classified into samples that show a streaky RHEED and spotty RHEED pattern. In addition, the labels beneath the squares refer to the relative PL intensity, the spectral position of the PL maxima, and the FWHM value. Evidently, similar results

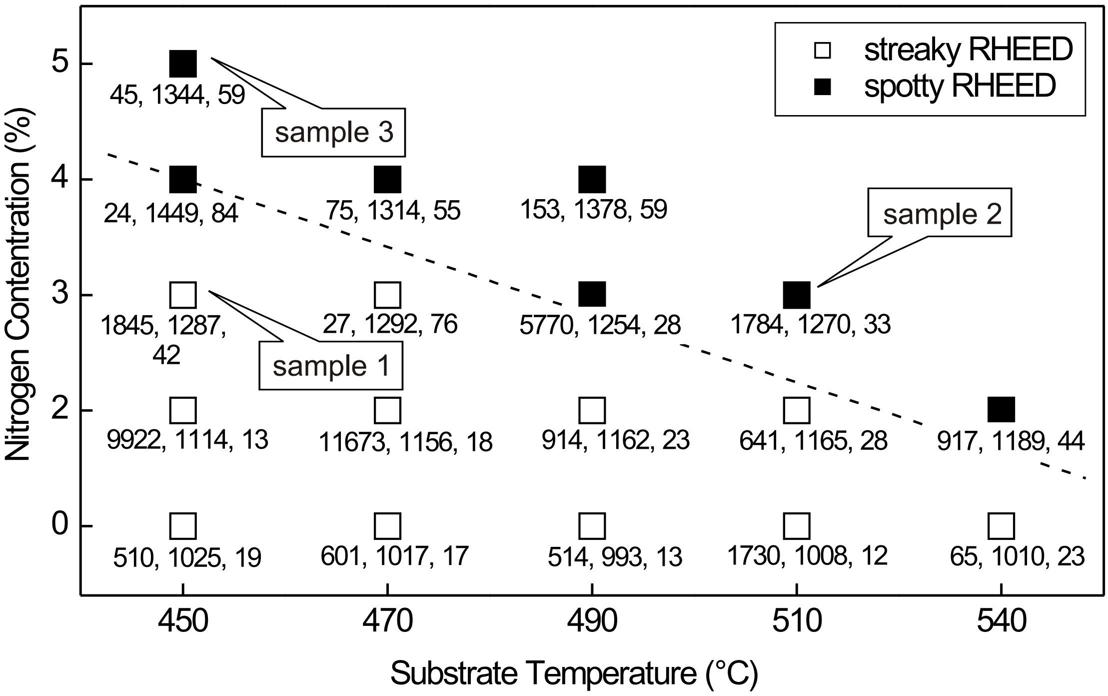

Figure 4.1: 10-period (7/14) nm (In,Ga)(As,N)/GaAs MQWs with 30% indium grown at different substrate temperatures and different nitrogen concentrations. Samples that show a streaky RHEED pattern are denoted by blank squares; samples that show a spotty RHEED pattern are represented by filled squares. The numbers underneath the squares refer to the PL intensity, the spectral position of the PL maximum, and the FWHM value. Samples were grown under a BEP ratio of 20 with plasma source parameters of 300 W and 0.04 sccm. For PL measurements, the samples have been annealed at 800°C for 60 s. The PL measurements were accomplished at 10 K.

with respect to figure 3.3 are observed. The incorporation of nitrogen at high substrate temperatures leads to a roughening of surfaces and interfaces. Interestingly, the roughening of (In,Ga)(As,N) is not strikingly different compared to Ga(As,N), albeit the (In,Ga)(As,N) samples are compressively strained whereas the Ga(As,N) samples are tensile strained. Hence, roughening processes in Ga(As,N) and (In,Ga)(As,N) are not strain-driven but solely depend upon substrate temperature, nitrogen concentration, and QW thickness. In addition, there is a degradation of optical properties, such as a diminishing of the PL intensity, in case of (In,Ga)(As,N) samples that have rough surfaces and interfaces. The comparison with figure 3.1 shows stronger PL intensities of the (In,Ga)(As,N) samples with respect to Ga(As,N), owing to a higher valence band offset. As in case of Ga(As,N), (In,Ga)(As,N) samples have to be grown at low substrate temperatures, such as 450°C, to achieve a high morphological and optical quality.

Figure 4.1 also depicts the impact of the substrate temperature upon the growth of (In,Ga)As. No spotty RHEED pattern is observed, even for samples grown at high substrate temperatures. Concerning optical properties, we have found that 510°C is the optimum growth temperature of the annealed (In,Ga)As, indicated by the highest PL intensity and the lowest FWHM value. The same finding has been reported by other authors[73, 104]. For lower substrate temperatures, there is a deterioration of optical properties, possibly due to a higher concentration of point defects. On the contrary, growing at high substrate temperatures (540°C) also yields a decrease of the

PL intensity and an increase of the FWHM value. Gonzales *et al.* [105] have employed a theoretical model to explain this broadening with a compositional modulation of (In,Ga)As grown at elevated temperatures.

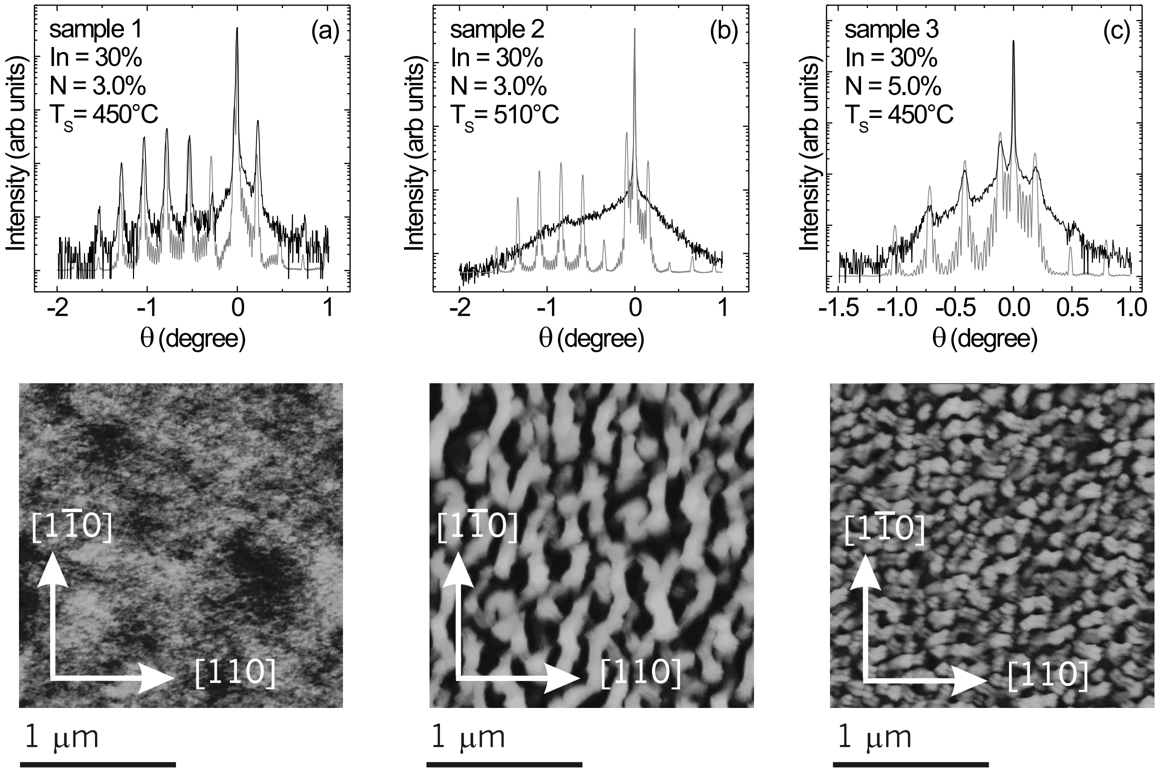

Figure 4.2: XRD curves and AFM images sample 1 (a), 2 (b), and 3 (c) of figure 4.1. The AFM images yield RMS values of 0.3 nm (a), 20 nm (b), and 7 nm (c). XRD measurements were accomplished around the (004) reflection.

In order to affirm the structural degradation of (In,Ga)(As,N) samples grown at elevated substrate temperatures and high nitrogen concentrations, XRD as well as AFM have been carried out. Figure 4.2 shows XRD curves and AFM images of three (In,Ga)(As,N) samples with 30% indium. Two samples (sample 1 and 2 in figure 4.1), that comprise 3% nitrogen, were grown at 450°C (a) and 510°C (b), respectively. The third sample (sample 3 in figure 4.1) contains 5% nitrogen and was grown at 450°C (c). Indeed, a structural degradation occurs for (In,Ga)(As,N) grown at high substrate temperatures and/or high nitrogen concentrations that is observed by rough surfaces in the AFM images as well as broadened and smeared out satellite peaks in the XRD curves.

To investigate the impact of the BEP ratio upon the growth of (In,Ga)(As,N), four 10-period (6/12) nm (In,Ga)(As,N)/GaAs MWQ samples have been grown with different BEP ratios. The nominal indium and nitrogen concentrations amount to 36% and 3%, respectively. Figure 4.3 shows XRD curves and PL spectra of these samples grown with BEP ratios in a range of 10 and 100. Concerning the XRD curves, there is a slight shift of the satellite peaks away from the GaAs substrate peak for higher BEP ratios. This shift manifests a higher compressive strain in case of the samples grown with a

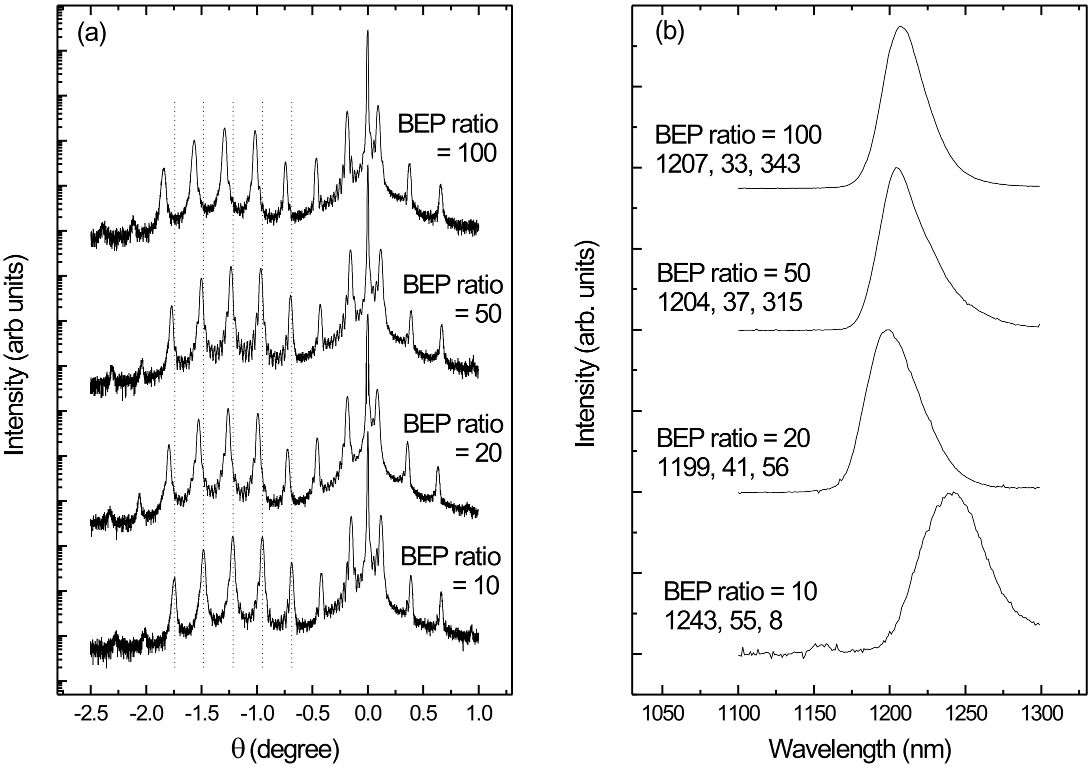

Figure 4.3: XRD curves (a) and PL spectra (b) of four 10-period (6/12) nm (In,Ga)(As,N)/GaAs MQWs grown under different BEP ratios with plasma source parameters of 300 W and 0.008 sccm. The nominal indium and nitrogen concentrations are 36% and 2.8%, respectively. PL measurements were carried out at 10 K. The numbers refer to the spectral position of the PL maxima, the FWHM value, and the PL intensity. XRD measurements were accomplished around the (004) reflection.

high BEP ratio. Thus, from this observation, one can infer a lower nitrogen incorporation and/or a higher indium incorporation for a high arsenic overpressure. Figure 4.4 shows XRD curves and PL spectra of four (In,Ga)As grown under the same conditions as the samples in figure 4.3. No trend regarding a change of the indium concentration in dependence of the BEP ratio is ascertained. In section 3.1, we observed a reduced nitrogen incorporation for higher BEP ratios (figure 3.4). Thus, we exemplify the shift of the satellite peaks in the XRD curves with a lower nitrogen incorporation for higher BEP ratios. Regarding the PL spectra, there is a redshift of the samples grown under a very low BEP ratio. Again, this phenomenon can be elucidated with a higher nitrogen incorporation for lower BEP ratios.

Another critical issue about the quaternary material system is the spatial homogeneity of the indium concentration across the sample. In section 3.1, the homogeneity of the nitrogen concentration throughout the sample has been discussed. The substrate rotation is mandatory to ensure a homogeneous nitrogen concentration (see figure 3.7). Figure 4.5 depicts the homogeneity of the indium concentration throughout the sample grown without (a) and with substrate rotation (b). For this analysis, two 10-period (In,Ga)As/GaAs MQW have been cleaved into 9 pieces to subsequently analyze the indium concentration (upper number) and the (In,Ga)As quantum well thickness (lower number). Evidently, the sample grown without substrate rotation shows quite a change

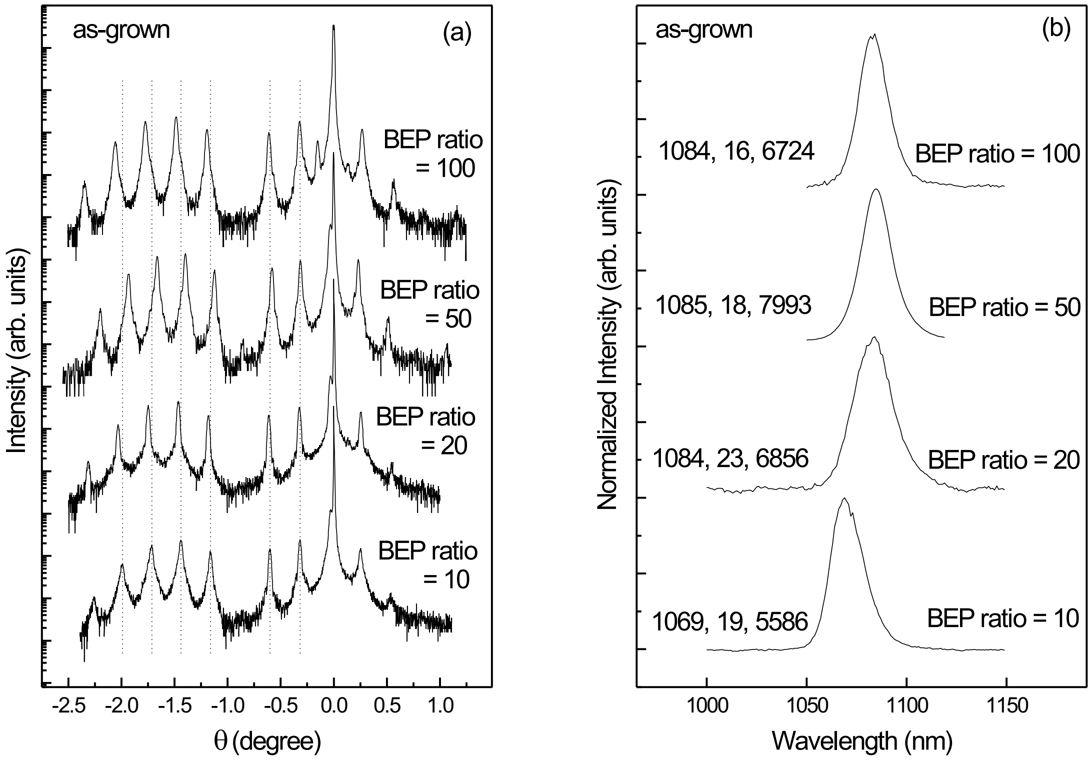

Figure 4.4: XRD curves (a) and PL spectra (b) of four (In,Ga)As/GaAs MQWs grown with the same conditions as the (In,Ga)(As,N)/GaAs MQWs depicted in figure 4.3. No clear trend regarding the indium incorporation is discernable. The numbers in (b) refer to the spectral position of the PL maxima, the FWHM value, and the PL intensity. PL measurements were carried out at 10 K. XRD curves were recorded around the (004) reflection.

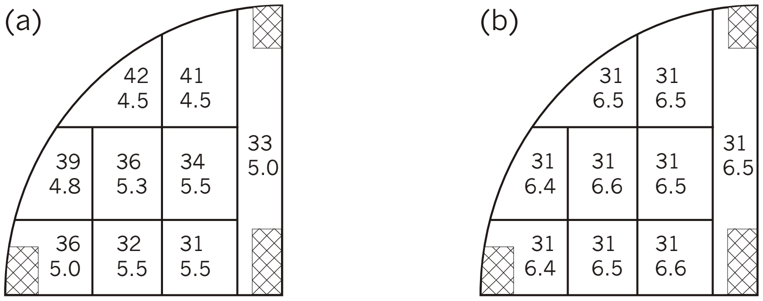

Figure 4.5: The spatial homogeneity of the indium concentration (upper number, in percent) and the QW thickness (lower number, in nm) of an (In,Ga)As/GaAs MQW structure grown without (a) and with substrate rotation (b).

of the indium concentration and the (In,Ga)As well thickness throughout the sample. On the contrary, there is no significant change of the indium concentration and well thickness for different pieces of the sample grown with substrate rotation. Thus, the substrate rotation ensures the spatial homogeneity regarding the indium concentration and the (In,Ga)As well thickness across the sample.

Band gap of (In,Ga)As In comparison to the Ga(As,N) material system, the band gap bowing of (In,Ga)As is less pronounced (cf. figure 2.1). The band gap of (In,Ga)As for a temperature range of 2 - 300 K is well described by the following equation[106]:

$$E_G\left[(In,Ga)As)\right] = E_G\left[GaAs\right] - 1.5\,y + 0.4\,y^2 \tag{4.1}$$

where y represents the indium concentration. A plot of equation 4.1 is depicted in figure 4.6. In addition, experimental data points derived from PL measurements are given for comparison[1]. Roughly spoken, an indium concentration of 1% reduces the band gap of (In,Ga)As by 15 meV.

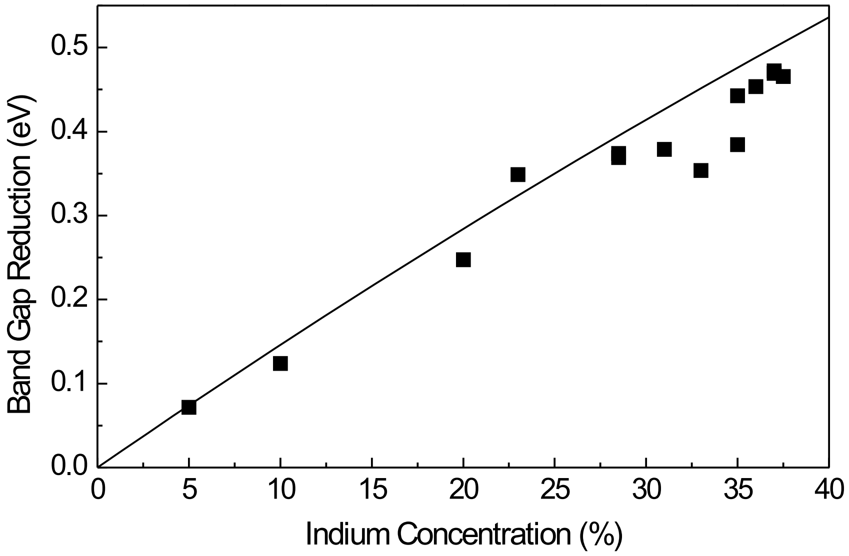

Figure 4.6: Band gap reduction of (In,Ga)As with respect to the indium concentration. The band gap reduction was deduced by means of PL measurements. The solid line refers to equation 4.1.

Control of the indium and nitrogen concentration In case of Ga(As,N), one can control the nitrogen concentration by changing the GaAs growth rate (see chapter 3.1) owing to a unity sticking coefficient of nitrogen. Consequently, the nitrogen incorporation is inversely proportional to the GaAs growth rate (equation 3.1). The same principle can be employed for (In,Ga)(As,N). However, to control the nitrogen concentration, one has to take into account the GaAs and the InAs growth rate. The nitrogen concentration N is then inversely proportional to the sum of the GaAs and InAs growth rates:

$$N \propto \frac{1}{v_{GaAs} + v_{InAs}} \tag{4.2}$$

To control the indium concentration, one has to think of a competition between the incorporation of indium and gallium. The sum of the indium and gallium concentration

---

[1] Again, as in case of figure 3.8, one has to take into consideration the confinement energy to deduce the band gap from PL measurements (equation 2.3). For this analysis, the confinement energy of electrons and holes was taken into account. The barrier height was calculated from equation 4.1, whereas a conduction band/valence band offset of 70/30 was assumed[107].

has to be unity. Consequently, the indium concentration In depends upon the GaAs and InAs growth rate as:

$$In = \frac{v_{InAs}}{v_{GaAs} + v_{InAs}} \tag{4.3}$$

Thus, for a given nitrogen and indium concentration, two steps are required to calculate the GaAs and InAs growth rates (in order to determine the gallium and indium effusion cell temperatures). First, from the nitrogen concentration, one can employ equation 4.2 to calculate the sum of the GaAs and InAs growth rates. Second, equation 4.3 can subsequently be applied to calculate the separate GaAs and InAs growth rates.

Determination of the nitrogen and indium concentration In section 3.1, the determination of the nitrogen concentration by means of PL and XRD has been discussed. Both techniques can independently be employed to estimate the nitrogen concentration. Unfortunately, in case of (In,Ga)(As,N), the determination of the constituent elements is more complex. In fact, one cannot employ XRD or PL independently but one has to combine both characterization techniques in order to detect the indium and nitrogen concentrations. From XRD measurements, the out-of-plane lattice constant of (In,Ga)(As,N) is determined. However, from this value, it is not possible to ascertain the indium and nitrogen concentration directly. For example, one finds the same out-of-plane lattice constant of (In,Ga)(As,N) for different indium and nitrogen concentrations if the indium/nitrogen concentration ratio remains constant. As a result, from the out-of-plane lattice constant of (In,Ga)(As,N), solely the (indium/nitrogen) concentration ratio can be drawn. Nonetheless, the (indium/nitrogen) concentration ratio may be used in PL measurements to determine absolute values of the constituent elements. The underlying assumption is that the band gap reductions induced by the indium and nitrogen incorporation are additive[68]. Hence, it is feasible to obtain an estimate of the indium and nitrogen concentrations from a combination of XRD and PL measurements.

Another approach to measure the indium and nitrogen concentration can be accomplished by growing the ternary and quaternary material system as there is no correlation between the incorporation of indium and nitrogen[108]. For example, one can ascertain the indium and nitrogen concentration by growing (In,Ga)As and (In,Ga)(As,N) with the same growth parameters. From XRD measurements of (In,Ga)As, one can unambiguously determine the indium concentration as well as the InAs and GaAs growth rates. From the sum of InAs and GaAs growth rates, one can subsequently employ equation 4.2 to calculate the nitrogen concentration of (In,Ga)(As,N).

Summary Among numerous parameter to grow (In,Ga)(As,N), the substrate temperature is most crucial. As in case of Ga(As,N), a roughening of surfaces and interfaces occurs for high substrate temperatures. Thus, low substrate temperatures are essential to grow the quaternary material system. The BEP ratio has a slight influence on the nitrogen incorporation, whereas it does not affect the indium incorporation. For determining the nitrogen and indium concentration, one can either combine PL and XRD measurements, or grow the ternary and quaternary material system separately.

4.2 Rapid Thermal Annealing of (In,Ga)(As,N)

In the previous chapter, we have found that RTA of Ga(As,N) is mandatory to improve optical properties. Concomitantly, there are structural changes in the annealed Ga(As,N) samples. This section is dedicated to the issue of RTA-induced structural and optical changes of (In,Ga)(As,N).
For this analysis, three (In,Ga)As/GaAs MQW samples as well as two (In,Ga)(As,N)/GaAs MQW samples have been grown. Sample 1, 2, and 3 refer to 10-period (6/12) nm (In,Ga)As/GaAs MQWs with 5%, 24%, and 36% indium, respectively. Sample 4 and 5 stand for 10-period (6/12) nm (In,Ga)(As,N)/GaAs MQWs with 36% indium as well as 1.5% and 2.8% nitrogen, respectively. All samples have been grown at 450°C with a BEP ratio of 50.

Rapid thermal annealing of (In,Ga)As Figure 4.7 shows XRD curves and PL spectra of three as-grown and annealed (In,Ga)As/GaAs MQWs (sample 1, 2, and 3). Regarding sample 1, no change between the XRD curves of the as-grown and the annealed sample is ascertained. On the contrary, concerning sample 2, there is a broadening of the satellite peaks in case of the annealed sample. Moreover, the envelope function is shifted towards the GaAs substrate peaks. The satellite peak broadening and the shift of the envelope function is even more pronounced in the XRD curves of sample 3. Concerning the PL spectra of sample 1, one can observe a slight blueshift in case of the annealed sample. Again, this trend is more pronounced in case of sample 2. The highest blueshift is observed in the PL spectra of sample 3. These findings can now be understood in terms of a strain-dependent indium interdiffusion induced by the thermal treatment. As discussed in section 2.2, an indium interdiffusion alters the position of the envelope function that is determined by the indium concentration in the (In,Ga)As QWs (cf. figure 2.6). The satellite peak broadening can be exemplified with a breaking of the translational symmetry of the (In,Ga)As QWs. The indium interdiffusion also explains the PL blueshift. Two strategies can be employed to elucidate this phenomenon. First, a lower indium concentration in the (In,Ga)As QWs leads to a lower band gap reduction. As a result, the energy difference between the conduction band edge and valence band edge increases, resulting in a blueshift of the PL spectrum. Second, the indium interdiffusion leads to a lower effective width of the (In,Ga)As QWs, thus causing higher confinement energies of electron and holes (equation 2.3). Consequently, the energy difference between electrons and holes increases, resulting in a PL blueshift. It is worth to emphasize the different nature of the PL blueshifts for Ga(As,N) and (In,Ga)(As,N). In case of Ga(As,N), the blueshift is attributed to an RTA-induced removal of defects, whereas in (In,Ga)As the blueshift is accounted for an RTA-induced indium interdiffusion.
In order to gain further experimental evidence of an indium interdiffusion, the impact of different RTA temperatures upon XRD curves has been investigated. Figure 4.8 shows the XRD curves of sample 3, annealed at different temperatures for 60 s. Univocally, the broadening of the satellite peaks as well as the shift of the envelope function becomes more pronounced with higher RTA temperatures. To quantitatively

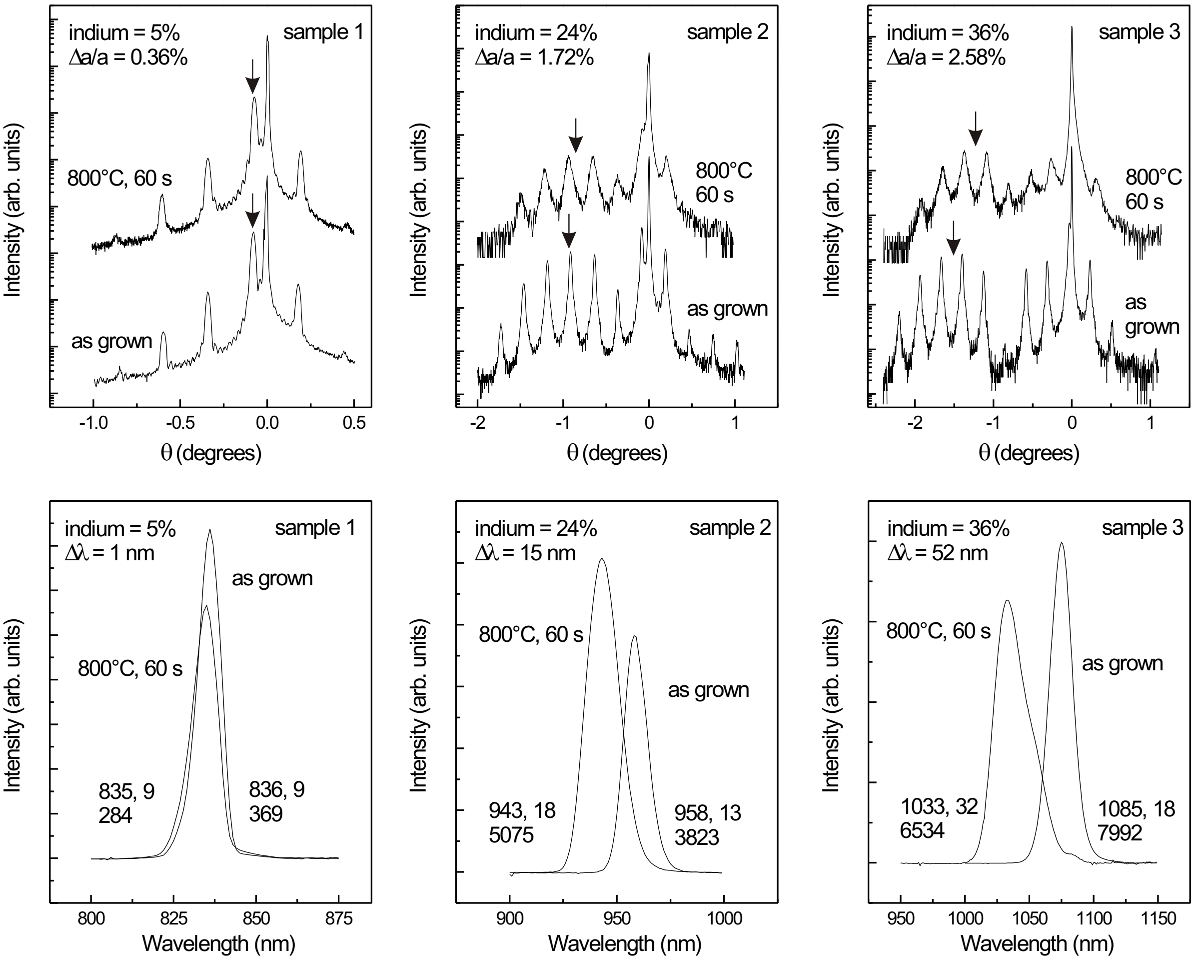

Figure 4.7: XRD curves and PL spectra of three (In,Ga)As/GaAs MQWs with 5%, 24%, and 36% indium (sample 1, 2, and 3). XRD measurements were carried out around the (004) reflection. PL measurements were accomplished at 10 K. The numbers next to the spectra refer to the wavelength, FWHM value, and intensity. The arrows denote the maxima of the envelope functions.

investigate the indium interdiffusion process, one has to solve the diffusion equation:

$$\frac{\partial}{\partial t}C(x,t) = D\frac{\partial^2}{\partial x^2}C(x,t) \tag{4.4}$$

where $C(x,t)$ is the indium concentration profile and D stands for the diffusion coefficient. Assuming that prior to the thermal treatment, the indium concentration profile is rectangular with an indium concentration C_0 inside the quantum well, one can solve equation 4.4 through[109]:

$$C(x,t) = \frac{C_0}{2}\left[\operatorname{erf}\left(\frac{W+2x}{4x_D}\right) + \operatorname{erf}\left(\frac{W-2x}{4x_D}\right)\right] \tag{4.5}$$

where $x_D = \sqrt{Dt}$ is the diffusion length, t is the annealing time, W the width of the (In,Ga)As quantum well thickness, and erf the error function. The diffusion length x_D can now be used as a parameter to describe the indium interdiffusion process. Figure

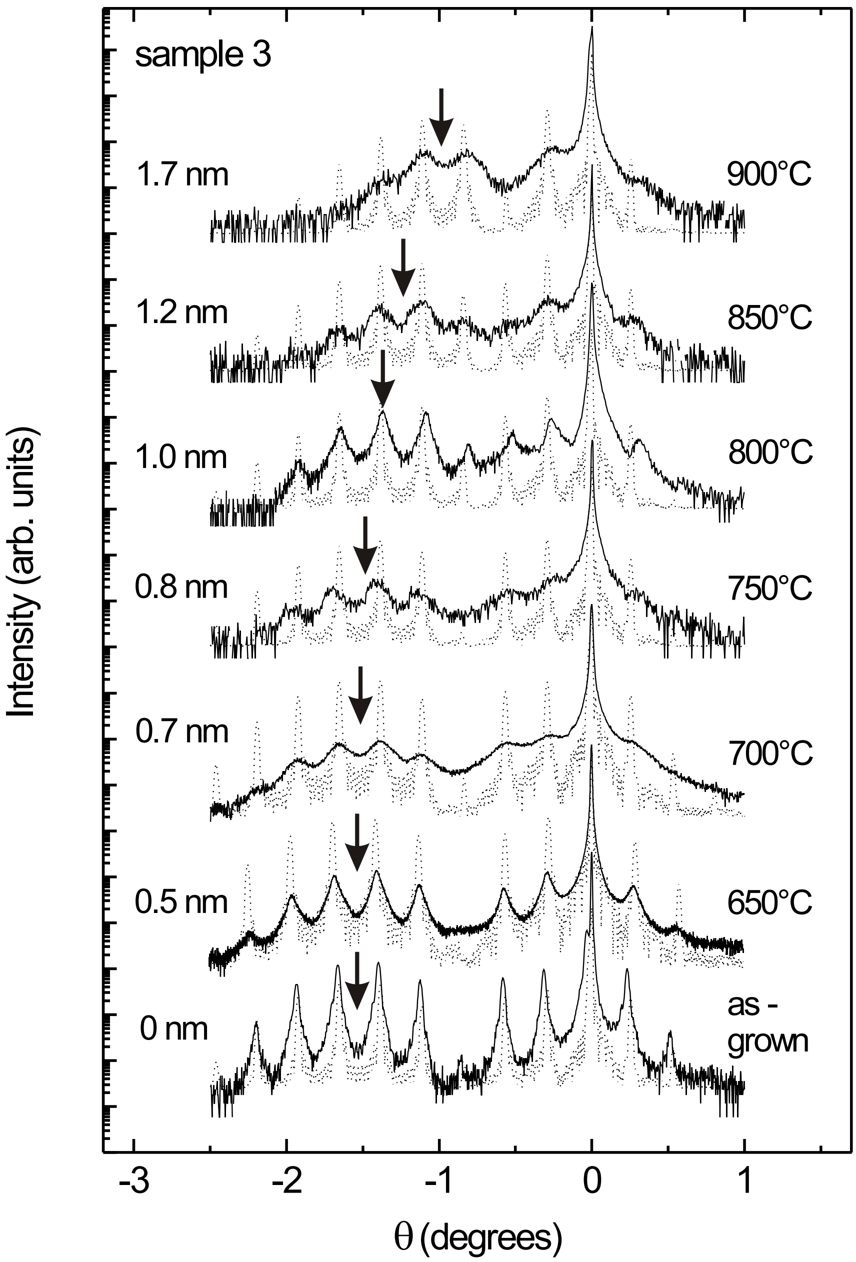

Figure 4.8: XRD curves of the (In,Ga)As/GaAs MQW with 36% indium (sample 3) annealed at different temperatures for 60 s. The measurements were accomplished around the (004) reflection. The arrows indicate the maxima of the envelope functions. The dotted curves refer to the simulations. The left-hand side numbers stand for the diffusion lengths that have been employed in these simulations.

4.9 shows two indium concentration profiles for $x_D = 0$ nm (a) and $x_D = 1.7$ nm (b). Apparently, there is a transition from a rectangular to a smeared out indium concentration profile for larger x_D. It is worth noting that the integrated indium concentration remains constant irrespective of the diffusion length. The indium concentration profile determined from equation 4.5 can now be loaded into the XRD computer simulation. By varying the diffusion length x_D, one can find concordance between the simulation and the experimental data. The dotted lines in figure 4.8 refer to these simulations. The left hand side number represents the diffusion lengths for the pertinent simulated

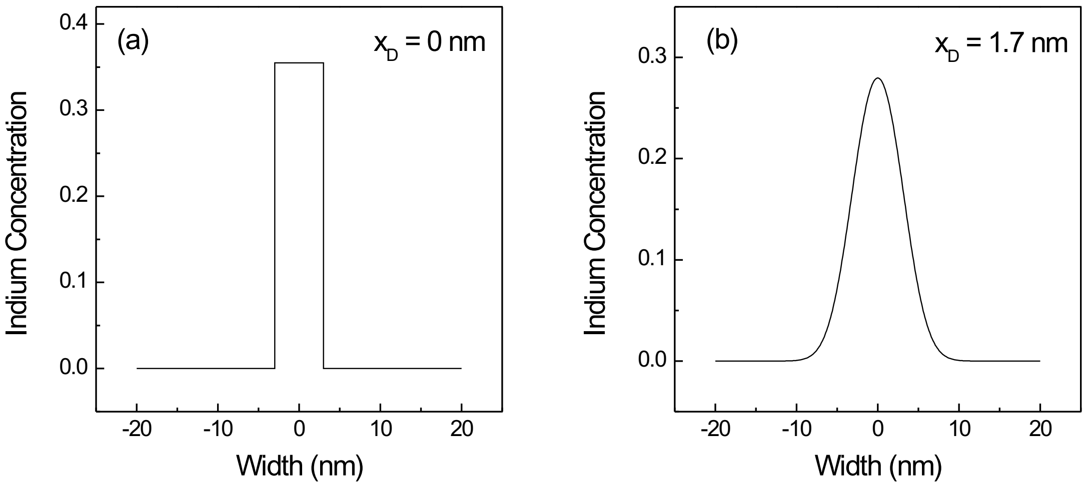

Figure 4.9: Two indium concentration profiles determined from equation (4.5). The diffusion length x_D amounts to 0 nm (a) and 1.7 nm (b).

XRD curves. Indeed, increasing the RTA temperature leads to larger diffusion lengths, hinting at a more pronounced indium interdiffusion for higher RTA temperatures.

Rapid thermal annealing of (In,Ga)(As,N) Figure 4.10 shows two PL spectra of the (In,Ga)(As,N)/GaAs MQW sample with 36% indium and 2.8% nitrogen (sample 5). In contrast to the (In,Ga)As samples, the as-grown (In,Ga)(As,N) sample scarcely emits a PL signal, whereas there is a substantial improvement of the PL in case of the annealed sample. As in case of Ga(As,N), this can be elucidated with a removal of growth-induced defects that are generated by the nitrogen plasma source.

In order to investigate RTA-induced structural changes, XRD measurements were carried out. Figure 4.11 shows XRD curves of three (In,Ga)(As,N)/GaAs MQWs (sample 3, 4, and 5). Apparently, sample 3 shows smeared out satellite peaks as well as a shift of the envelope function towards the GaAs substrate peak. In the previous paragraph, this observation has been explained by an RTA-induced indium interdiffusion. In contrast, the satellite peak broadening as well as the shift of the envelope function is less pronounced in case of sample 4. Concerning sample 5, no difference between the as-grown and the annealed XRD curves is ascertained. Apparently, the incorporation of nitrogen suppresses the RTA-induced indium interdiffusion.

Discussion It is well known that indium interdiffusion occurs via gallium vacancies[110]. Therefore, a lower gallium vacancy concentration impedes indium interdiffusion. Hence, the gallium vacancy reduction – induced by the incorporation of nitrogen – may be deemed the origin of the indium interdiffusion suppression. One can elucidate the annihilation of gallium vacancies by incorporating nitrogen in two ways. First, gallium vacancies are negatively charged. Consequently, a higher n-type background concentration shifts the Fermi level to higher values, thus promoting the formation of gallium vacancies during the growth[110]. Conversely, a higher p-type background concentration impedes the formation of gallium vacancies. Figure 4.12

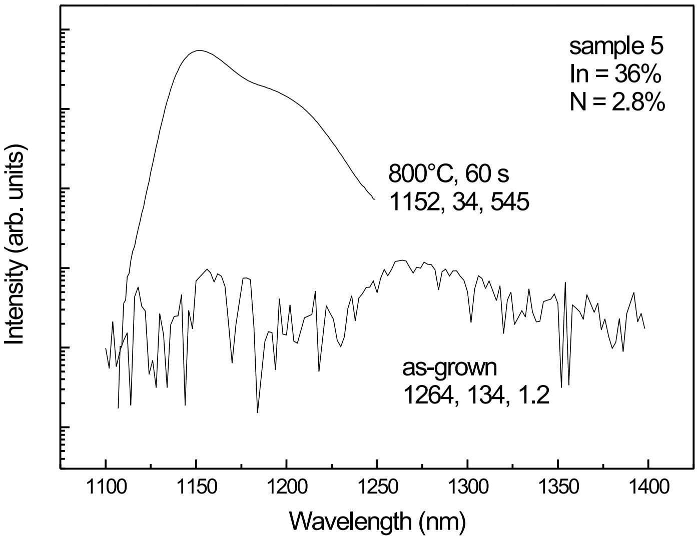

Figure 4.10: Two PL spectra of the as-grown and at 800°C for 60 s annealed (In,Ga)(As,N)/GaAs MQW with 36% indium and 2.8% nitrogen. Measurements were performed at 10 K. The numbers refer to the wavelength, and the FWHM value (in nm), as well as the intensity (arb. units).

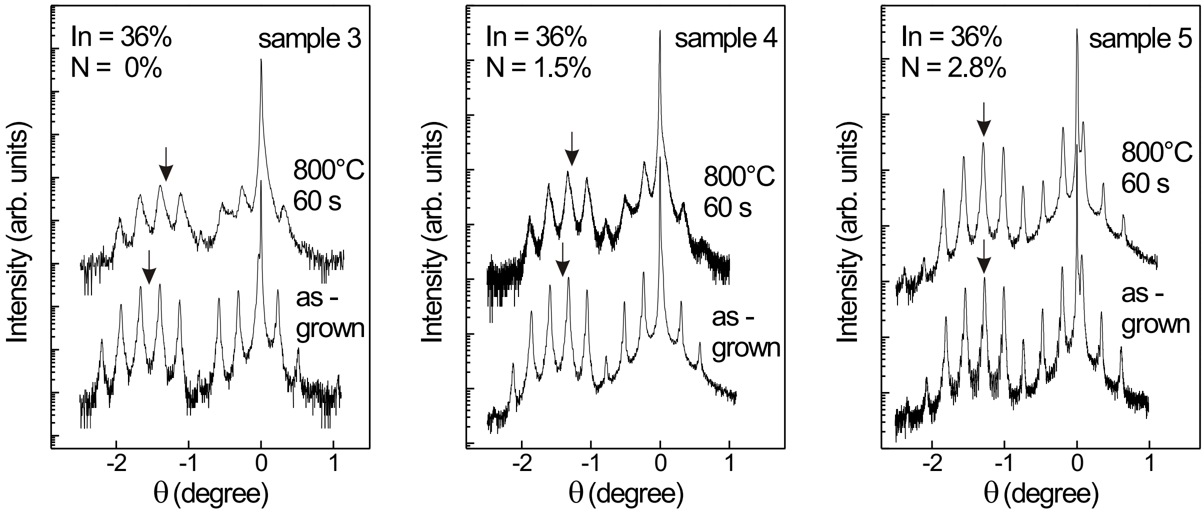

Figure 4.11: XRD curves of as-grown and at 800°C for 60 s annealed (In,Ga)(As,N) MWQs with 36% indium and 0%, 1.5%, and 2.8% nitrogen (sample 3, 4, and 5). The measurements were accomplished around the (004) reflection. The arrows denote the maxima of the envelope functions.

depicts as-grown and annealed XRD curves of sample 3. In addition, figure 4.12 shows two (In,Ga)As samples grown with identical parameters as sample 3 but comprise beryllium concentrations of 5×10^{17} cm^{-3} and 8×10^{18} cm^{-3}, respectively . Indeed, there is an indium interdiffusion suppression for higher p-type doping concentrations, as the RTA-induced shift of the envelope function is less pronounced for higher p-type concentrations. In case of the (In,Ga)As sample that comprises a beryllium concentration of 5×10^{17} cm^{-3}, there is a slight shift of the envelope function, whereas no shift is

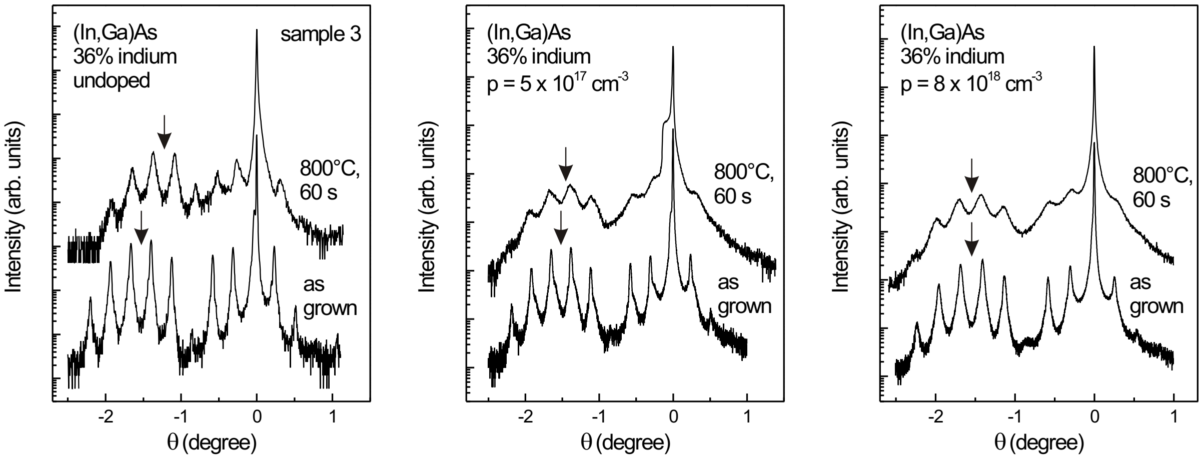

Figure 4.12: XRD curves of undoped and p-type doped (In,Ga)As/GaAs MQWs with 36% indium. XRD measurements were accomplished on as-grown and at 800°C for 60 s annealed samples around the (004) reflection. The arrows denote the maxima of the envelope functions.

ascertained for the (In,Ga)As sample that contains 8×10^{18} cm^{-3} beryllium. Hence, a p-type doping concentration of more than 5×10^{17} cm^{-3} is required to cease the indium interdiffusion. To explain the gallium vacancy reduction, one might think that the incorporation of nitrogen causes a higher p-type background concentration. Hall measurements have been carried out to determine the carrier concentration of undoped Ga(As,N). However, the background concentration is below the Hall measurement resolution limit. Thus, we estimate that the undoped Ga(As,N) carrier concentration is less than 2×10^{16} cm^{-3}. As a result, one cannot account the gallium vacancy reduction by a nitrogen-induced change of the carrier concentration because much higher p-type concentrations are required to suppress the indium interdiffusion.

Another way to explain the gallium vacancy reduction is to postulate the incorporation of nitrogen into gallium vacancies. From Raman spectroscopy of Ga(As,N), we have obtained experimental evidence of nitrogen split interstitials that incorporate into gallium vacancies (cf. figure 3.16). Hence, these nitrogen split interstitials fill out gallium vacancies leading to a reduction of the gallium vacancy concentration. The indium interdiffusion suppression may be attributed to a filling out of gallium vacancies by nitrogen split interstitials.

Summary Rapid thermal annealing of (In,Ga)As causes an indium interdiffusion owing to the presence of Ga vacancies. The incorporation of nitrogen into (In,Ga)As decreases the Ga vacancy concentration, thus ceasing the RTA-induced indium interdiffusion. The reduction of the Ga vacancy concentration cannot be exemplified with a nitrogen-induced change of the carrier background concentration but is possibly related to nitrogen split interstitials that incorporate into Ga vacancies.

Chapter 5

(In,Ga)(As,N) Light Emitting Devices

The aim of investigating (In,Ga)(As,N) is to harness this material system for light emitting devices. In the previous chapters, the growth and properties of Ga(As,N) and (In,Ga)(As,N) have been investigated. In this chapter, these findings are applied to develop and characterize (In,Ga)As and (In,Ga)(As,N) edge emitting lasers.

Figure 5.1 depicts the design of the edge emitting lasers that are investigated in the following sections. The main components are (In,Ga)(As,N) or (In,Ga)As QWs that constitute the active layers. For developing a laser, two aspects have to be taken into consideration: optical confinement and carrier confinement. Optical confinement is crucial to warrant the laser functionality as it provides a confinement of photons in growth direction. Consequently, photons exit the laser structure at the cleavage edges of the sample where they are coupled into a glass fibre. Optical confinement is accomplished by the (Al,Ga)As/GaAs interfaces owing to a large refractive index contrast between GaAs and (Al,Ga)As. Carrier confinement is another important issue as it assures that radiative recombination of electrons and holes takes place in the active layers. Thus, the wavelength of the emitted light is mainly determined by the band gap of the active layers. Carrier confinement in the active layers is accomplished by the (In,Ga)As/GaAs and (In,Ga)(As,N)/Ga(As,N) interfaces by virtue of a sizeable band alignment offset. Carrier injection into the active layers is mediated by applying an external voltage. Prerequisite of carrier injection is p-type and n-type doping as well as p-type and n-type contacts. The p-type and n-type doping has been accomplished by the incorporation of silicon and beryllium, respectively. Titanium-gold and gold-germanium were used for p-type and n-type contacts. The (In,Ga)As and the (In,Ga)(As,N) edge emitting lasers were grown at the a low substrate temperatures of 450°C. Both types of lasers were grown with a BEP ratio of 50. Some lasers have been annealed ex-situ in an RTA furnace. After contacting, the lasers were cleaved into laser bars with a nominal bar length of 1000 μm. For lasers that show a high threshold current density, the bar length values 600 μm. Each laser bar comprises 20 contacts.

In order to explain the working principle of lasers, one has to introduce two terms: spontaneous and stimulated emission. Spontaneous emission refers to the absorption of photons, resulting in a generation of electron-hole pairs. These electron-hole pairs radiatively recombine at the band edges under the emission of a photon. Apart from absorption, a photon can also induce the recombination of electrons and holes, generating another photon. This process is called stimulated emission. At a certain threshold current, stimulated emission becomes more likely than absorption. This leads to

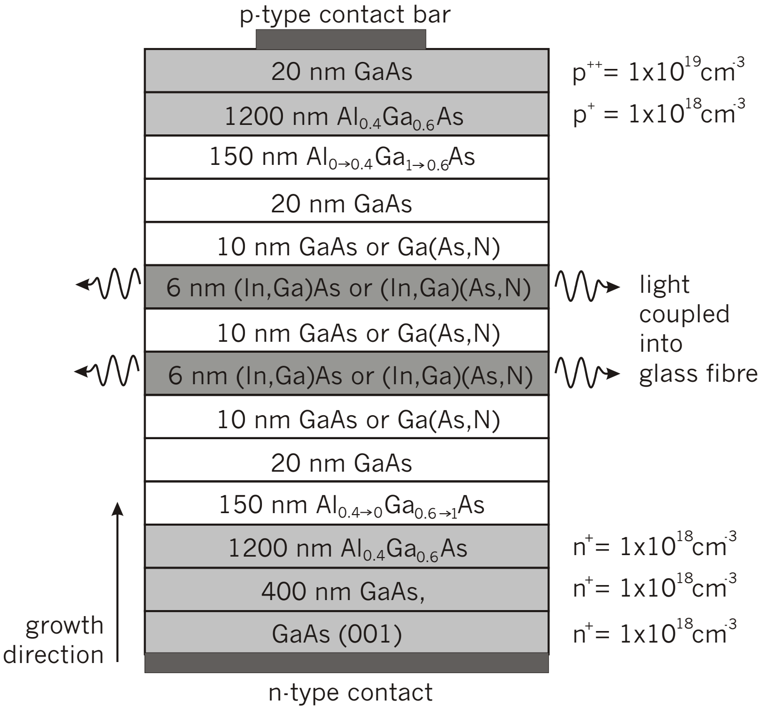

Figure 5.1: Layer sequence of the (In,Ga)As and (In,Ga(As,N) lasers that are discussed in this chapter.

a strong increase of the output power. Moreover, stimulated emission-generated photons have the same phase. Consequently, stimulated emission in an optical cavity leads to a wavelength-dependent amplification of the emitted light. Thus, the emission spectrum consists of ultranarrow laser modes. For edge emitting lasers, the optical cavity is accomplished by the refractive index contrast at the cleavage edges.

There are several figures of merit to assess the laser quality. Most important are the threshold current density and the slope efficiency. The threshold current density is determined by the threshold current divided by the area of the contact. The threshold current refers to the injected current when stimulated emission commences. The slope efficiency represents the stimulated emission-induced increase of the output power with respect to the current. Lasers of high quality are characterized by a low threshold current density and a high slope efficiency.

5.1 (In,Ga)As Edge Emitting Lasers

Four (In,Ga)As edge emitting laser structures have been grown, processed, and characterized. Laser 1, 2, 3, and 4 comprise two 6 nm (In,Ga)As QWs with 13%, 30%, 32%, and 38% indium, respectively. The characterization has been accomplished on the as-grown and the at 800°C for 60 s annealed lasers at RT. Figure 5.2 depicts the characteristics of the as-grown (In,Ga)As laser 1 that comprises 13% indium. Figure 5.2 (a) shows laser spectra for different currents. For low currents, the spectra have a low intensity and a high FWHM value, originating from spontaneous emission. Univocally, a transition from spontaneous to stimulated emission occurs at a threshold current of 150 mA. With higher currents, there is a strong stimulated emission-induced increase of the intensity. Moreover, the inset of figure 5.2 (a) shows a spectrum of high spectral resolution. Univocally, the spectrum comprises ultranarrow laser modes at 942 nm , resulting from stimulated emission in a cavity. Figure 5.2 (b) depicts the integrated intensity versus current. For low currents, the output power lies in the μW range, originating from spontaneous emission. When exceeding the threshold current of 150 mA, there is a substantial increase of the output power up to 80 mW, owing to stimulated emission. Considering the length of the stripe (1000 μm) as well as the width of the contact bar (50 μm), one can calculate a threshold current density of 300 A/cm^2. In order to obtain an ensemble of data from which statistical values are drawn, this analysis has been repeated for all 20 contacts.

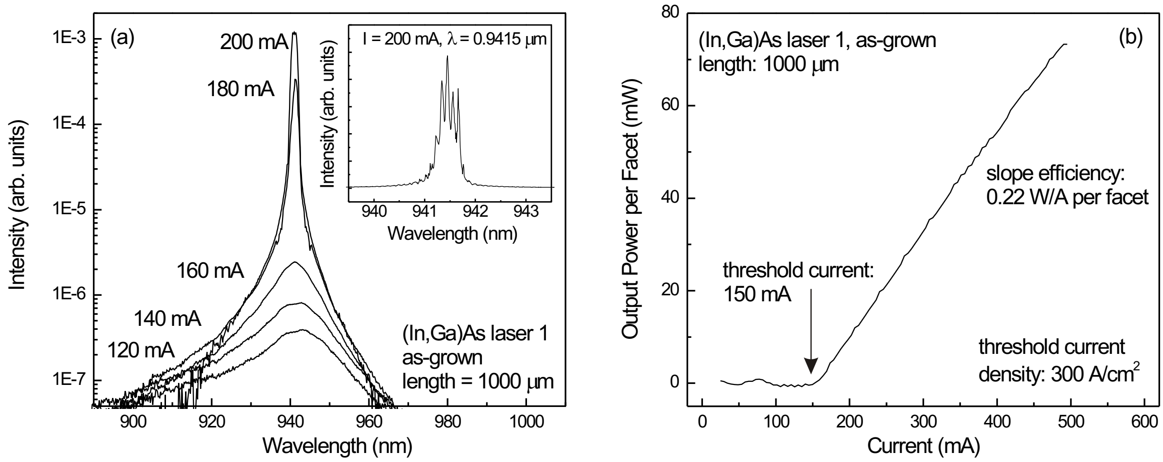

Figure 5.2: Spectra of the (In,Ga)As laser 1 for different currents (a). The inset shows a high-resolution spectrum of stimulated emission. Output power versus current characteristics (b). The measurements were accomplished in pulsed mode operation (2 kHz, 0.4% duty cycle) at RT.

Table 5.1 compiles the figures of merit obtained from the characterization of all as-grown and annealed (In,Ga)As lasers. Three observations are drawn. First, the emission wavelengths shift towards higher values with increasing indium concentration. This shift is consistent with the indium-induced band gap reduction. Second, no major change between as-grown and thermally annealed lasers is ascertained. There is a slight blueshift in case of the annealed samples. This blueshift is possibly due to indium interdiffusion (see chapter 4.2). Regarding the threshold current density as well as the slope efficiency, no major change between the as-grown and the annealed

(In,Ga)As laser is seen. For a very high indium concentration of 38% (laser 4), there is a strong increase of the threshold current density as well as a seizable decrease of the slope efficiency. This observation may be attributed to a strain-induced structural degradation of the active layers. This structural degradation can be understood in terms of exceeding the critical thickness of this strained layer system. Indeed, during the growth of the (In,Ga)As QWs, we observed a transition from a streaky to a spotty RHEED pattern when a certain (In,Ga)As thickness was exceeded. In addition, the XRD satellite peaks of laser 4 are substantially broadened. Elman *et al.* [111] have investigated the critical thickness of (In,Ga)As single quantum wells (SQWs) grown at low substrate temperature. According to their work, a thickness of 6 nm with an indium concentration of 38% is close to the critical thickness.

Table 5.1: Figures of merit regarding all as-grown and annealed (In,Ga)As lasers. The length of the laser bars amount to 1000 μm.

Label	Indium (%)	RTA (°C, s)	Wavelength (nm)	Threshold Current Density (A/cm^2)	Slope Efficiency per Facet (W/A)
Laser 1	13	–	942	340 ± 60	0.21 ± 0.03
Laser 1	13	800 , 60	939	420 ± 40	0.19 ± 0.03
Laser 2	30	–	1056	380 ± 40	0.19 ± 0.03
Laser 2	30	800 , 60	1046	360 ± 40	0.21 ± 0.03
Laser 3	32	–	1081	320 ± 40	0.19 ± 0.05
Laser 3	32	800 , 60	1077	460 ± 40	0.18 ± 0.05
Laser 4	38	–	1147	740 ± 140	0.13 ± 0.05
Laser 4	38	800 , 60	1132	720 ± 100	0.05 ± 0.02

Comparison with other works Highly strained (In,Ga)As edge emitting lasers with indium concentrations between 35 – 42% and emission wavelengths ranging from 1100 – 1215 nm have been reported by several authors [112, 113, 114, 115, 116, 117, 118, 119]. According to their works, lower threshold current densities in a range from 65 – 300 A/cm^2 were achieved. To explain the low threshold current density of theses lasers, two aspects have to be taken into account. First, the authors accomplished the growth at higher substrate temperatures between 510 – 530 °C that were optimized for the (In,Ga)As growth. The (In,Ga)As lasers of this work were grown at 450 °C to compare these lasers with (In,Ga)(As,N) lasers. Second, the authors report on (In,Ga)P strain mediating layers (SMLs) between (In,Ga)As and GaAs in order to increase the critical thickness of this strained layer system. Both factors are beneficial for the device performance. Nevertheless, the authors state a strong degradation of the (In,Ga)As laser performance for wavelengths above 1200 nm. The incorporation of nitrogen into (In,Ga)As is a conceivable avenue to accomplish light emitting devices for wavelengths above 1200 nm . (In,Ga)(As,N) light emitting devices will be discussed in the next section.

5.2 (In,Ga)(As,N) Edge Emitting Lasers

The aim of dealing with (In,Ga)(As,N) is to achieve laser diodes in the telecommunication range of 1.3 – 1.55 μm. Choosing the right indium and nitrogen concentration is of utter importance to succeed in accomplishing such devices. According to equation 2.1, one can reach an emission wavelength of 1.3 μm by incorporating 4.5% nitrogen into GaAs. Thus, one could think of accomplishing laser diodes emitting at 1.3 μm that are solely based upon Ga(As,N). However, there are three shortcomings of such devices. First, the incorporation of nitrogen is concomitant with an incorporation of point defects. With a higher nitrogen concentration, there is also a higher concentration of these defects. Second, there is a nitrogen-induced strong increase of the effective electron mass which is detrimental to the device performance. Thus, one should keep the nitrogen concentration as low as possible. Third, the nitrogen-induced band gap reduction mainly affects the conduction band. The valence band of Ga(As,N) remains mostly unchanged[43]. Consequently, the valence band offset between Ga(As,N) and GaAs is small, causing a detrimental effect upon the thermal stability of device operations. As discussed in the preceding section, one can accomplish (In,Ga)As lasers with low threshold current densities that comprise up to 35% indium. Thus, in order to achieve (In,Ga)(As,N) laser diodes emitting at 1.3 μm, the indium and nitrogen concentration should amount to approximately 35% and 2%, respectively.

In this section, three (In,Ga)(As,N) lasers will be presented. All lasers contain 35% indium. The nitrogen concentrations of laser 1, 2, and 3 amount to 1%, 1.5%, and 3% nitrogen, respectively. In contrast to the (In,Ga)As edge emitters, the (In,Ga)(As,N) layers are surrounded by Ga(As,N) layers with the same amount of nitrogen as the (In,Ga)(As,N) layers. Theses Ga(As,N) SML are beneficial for two reasons. First, the tensile-strained Ga(As,N) layers counteract the highly compressive strain in the (In,Ga)(As,N) active layers. Second, the height of the barriers that surround the (In,Ga)(As,N) active region is lower, owing to a smaller band gap of Ga(As,N) with respect to GaAs. Thus, the confinement energy of electrons and holes is reduced, resulting in longer emission wavelengths. Several authors have reported on the beneficial effect of SMLs[70, 120]. In fact, nowadays, Ga(As,N) SMLs are ubiquitous in (In,Ga)(As,N) lasers.

The in-situ annealing effect Figure 5.3 shows features of the as-grown and annealed (In,Ga)(As,N) laser 1. The annealing was accomplished at 800°C for 60 s. Figure 5.3 (a) depicts the output power versus current characteristics of the as-grown laser 1. Indeed, stimulated emission occurs for currents above 230 mA. From the slope of the curve, one can determine an efficiency of 0.22 W/A. In Figure 5.3 (b), the emission spectrum of the as-grown laser at a current of 240 mA is seen. The stimulated emission takes place at 1250 nm. Figure 5.3 (c) and (d) shows features of the annealed laser 1. The threshold current density amounts to 4 kA/cm^2, whereas the emission wavelength values 1252 nm. From the comparison of the as-grown and annealed laser features, one can observe a low threshold current density in case of the as-grown laser, whereas the annealed laser shows a substantially higher threshold current density. To explain this observation, one might think of an in-situ annealing effect owing to the top (Al,Ga)As cladding layer. The growth of the top (Al,Ga)As cladding layer takes place at 580°C for 90 minutes. Exposing the (In,Ga)(As,N) active layers to this elevated temperature for such a long time results in an in-situ removal of growth-induced defects. An additional post-growth thermal treatment may not be beneficial to remove growth-induced defects. Conversely, it may create RTA-induced defects that are detrimental to the device performance (see also section 3.3). Therefore, regarding the (In,Ga)(As,N) laser 2 and 3, solely the as-grown lasers were contacted and characterized. These lasers will be presented in the next paragraph.

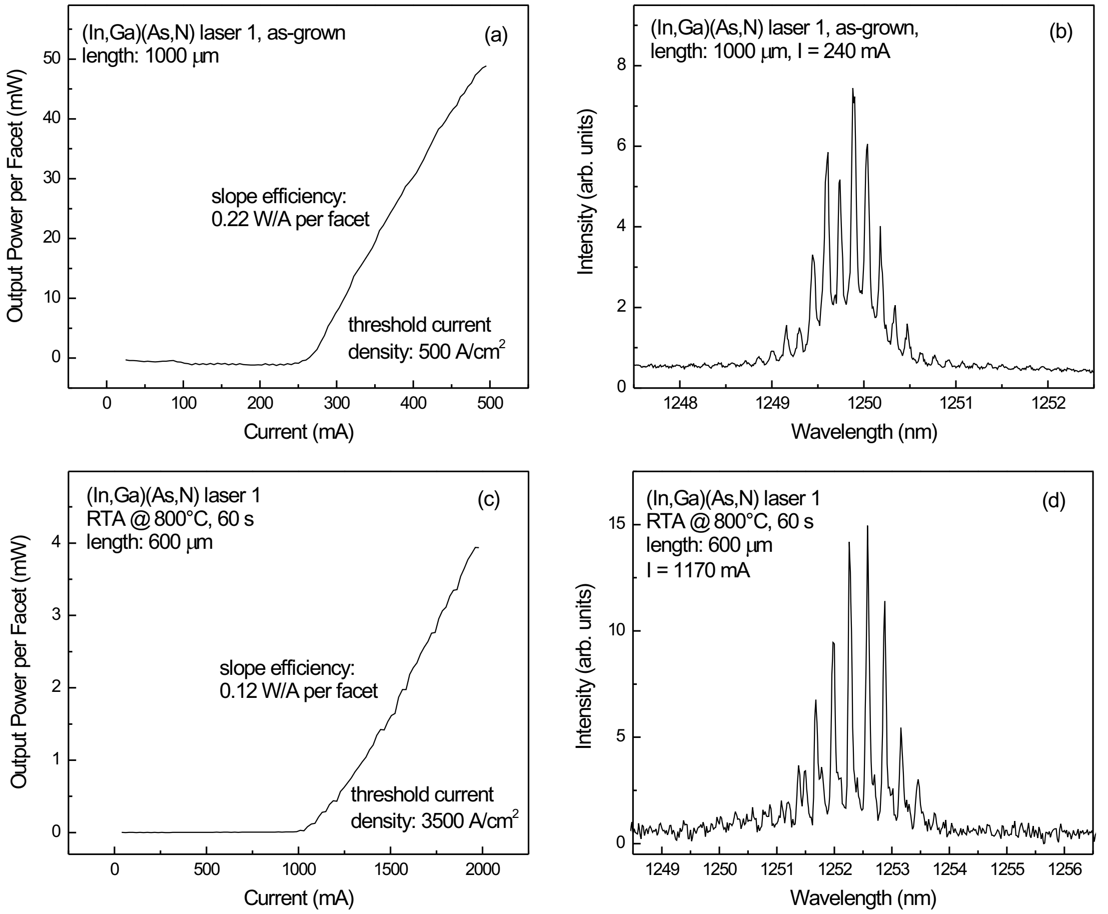

Figure 5.3: Output power versus current behavior and emission spectrum of the as-grown [(a) and (b)] as well as the annealed (In,Ga)(As,N) laser 1 [(c) and (d)]. The measurements were accomplished in pulsed mode operation (2 kHz, 0.4% duty cycle) at RT.

Aiming for longer wavelengths Figure 5.4 depicts emission spectra and the output power versus current behavior of the as-grown (In,Ga)(As,N) laser 2 and 3. The emission of laser 2 and 3 shifts towards longer wavelengths with respect to laser 1, having a value of 1266 nm and 1366 nm, respectively. Figure 5.4 also shows a substantial increase of the threshold current density and a conceivable decrease of the slope efficiency of laser 2 and 3 compared to laser 1. The threshold current density increases up to 2.8 kA/cm^2, whereas the slope efficiency goes down to approximately 1 mW/A. Still, figure 5.4 unambiguously shows that it is feasible to harness (In,Ga)(As,N) for accomplishing laser diodes in the desired wavelength range of 1.3 – 1.55 μm.

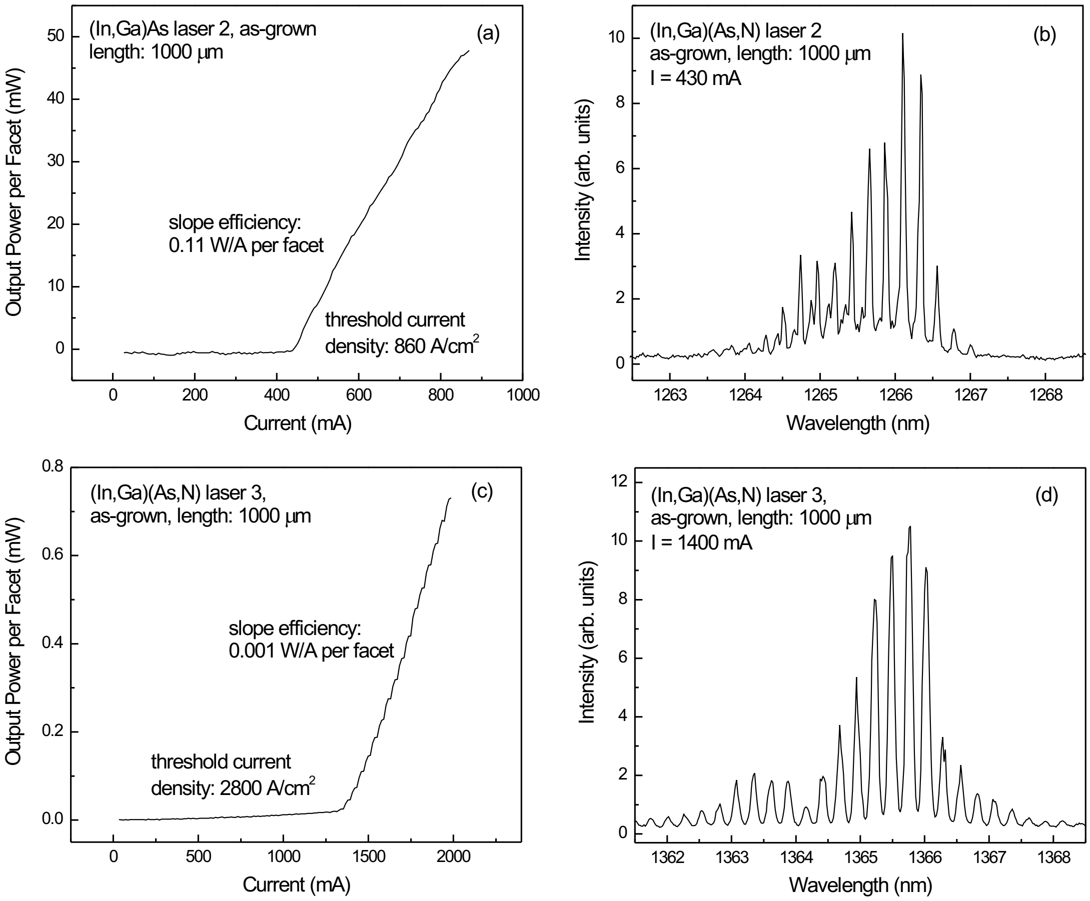

Figure 5.4: Output power versus current behavior and emission spectrum of the as-grown (In,Ga)(As,N) laser 2 [(a) and (b)] and the as-grown (In,Ga)(As,N) laser 3 [(c) and (d)]. The measurements were accomplished at RT in pulsed mode operation (2 kHz, 0.4% duty cycle).

Figures of merit and comparison with other works The analysis of all contacts on the laser bar yields an ensemble of data from which the figures of merit can be drawn. Table 5.2 compiles the figures of merit of all (In,Ga)(As,N) laser presented in this section.

Numerous authors have published figures of merit regarding (In,Ga)(As,N) lasers. Figure 5.5 depicts the threshold current density, taken from these publications, with respect to the emission wavelength. For (In,Ga)(As,N) lasers emitting around 1.3 μm, the threshold current density has a value of 0.3 – 10 kA/cm^2. Obviously, the threshold current densities of the lasers presented in this work – denoted by the filled squares – lie in the same range as the literature values. Figure 5.5 also displays (In,Ga)(As,N) lasers emitting up to 1.5 μm. Two strategies are employed to aim at longer emission wavelengths. First, there are authors who try to incorporate higher concentrations of nitrogen, up to 5% [6]. Second, several authors report on antimony incorporation[5, 74, 121, 122] for two reasons. First, antimony serves as a surfactant, thus inhibiting a structural degradation for high indium and nitrogen concentrations. Second, the incorporation of antimony causes a further band gap reduction (see figure 2.1). Still, accomplishing (In,Ga)(As,N) laser diodes that emit above 1.3 μm poses quite a challenge as there is a strong increase of the threshold current densities for these

Table 5.2: Figures of merit regarding the (In,Ga)(As,N) lasers. The cavity lengths of the as-grown and annealed laser 1 amount to 1000 μm and 600 μm. The cavity lengths of laser 2 and 3 value 1000 μm.

Label	In, N (%)	RTA (°C, s)	Wavelength (nm)	Threshold Current Density (kA/cm^2)	Slope Efficiency per Facet (W/A)
Laser 1	35, 1.0	–	1250	0.5 ± 0.1	0.22 ± 0.03
Laser 1	35, 1.0	800, 60	1252	4.0 ± 0.5	0.11 ± 0.04
Laser 2	35, 1.5	–	1266	0.9 ± 0.1	0.13 ± 0.02
Laser 3	35, 3.0	–	1366	2.8 ± 0.2	0.001 ± 0.0002

lasers.

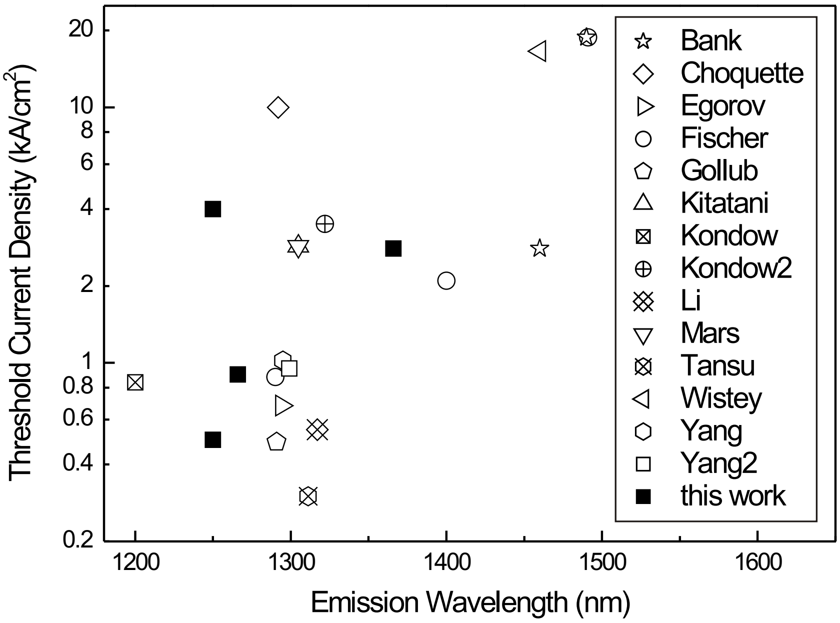

Figure 5.5: Reported threshold current densities of (In,Ga)(As,N) lasers with respect to the emission wavelength. The filled squares denote the lasers presented in this work. The authors in the legend refer to the following citations: Bank[74], Choquette[123], Egorov[7], Fischer[6], Gollub[124], Kitatani[125], Kondow[4], Kondow2[126], Li[8], Mars[127], Tansu[128], Wistey[5], Yang[122], Yang2[121]

Summary (In,Ga)As edge emitting lasers with indium concentrations in a range from 13 to 38% show stimulated emission at wavelengths between 939 and 1147 nm. There is a structural degradation for high indium concentrations, limiting the emission wavelength to 1150 nm. (In,Ga)(As,N) edge emitting lasers comprising 35% indium and nitrogen concentrations between 1 and 3% show stimulated emission in a wavelength range from 1250 to 1366 nm. The incorporation of nitrogen is concomitant with a strong increase of the threshold current density and a decrease of the output power.

Chapter 6

Conclusions and Outlook

Even though quite a number of papers related to Ga(As,N) and (In,Ga)(As,N) have already been published, this dissertation comprises several novel findings. First, the RTA parameters for optimizing optical properties of Ga(As,N) differ remarkably. To the best of our knowledge, no study on the optimum RTA temperature of Ga(As,N) with respect to the nitrogen concentration has ever been accomplished. Second, as far as we know, no direct experimental evidence of RTA-induced nitrogen diffusion in Ga(As,N) has been carried out. Thus, the nitrogen concentration profiles presented in this work provide – for the first time – an accurate insight into nitrogen diffusion processes of Ga(As,N). Third, no investigations on the roughening thickness of Ga(As,N) for such high nitrogen concentrations has been done. As far as we know, no report on a coherently strained Ga(As,N)/GaAs MQW sample with a nitrogen concentration of 7.4% has been published so far. Fourth, no survey on a suppression of indium interdiffusion owing to the incorporation of nitrogen into (In,Ga)As has been carried out up to date.
These novel findings are helpful to gain an insight into Ga(As,N) and (In,Ga)(As,N). The underlying goal is the realization of long wavelength (In,Ga)(As,N) lasers. In this thesis, we have demonstrated the viability of (In,Ga)(As,N) lasers that emit in the vital telecommunication wavelength range of 1.3 – 1.55 μm. However, there is a strong degradation of the performance in case of (In,Ga)(As,N) lasers above 1.3 μm. In this work, we have shown that this degradation is mainly attributed to point defects that are induced by the plasma source. Therefore reducing the amount of ions that impinge on the sample surface offers a great potential to enhance the (In,Ga)(As,N) laser performance. Several strategies are conceivable to achieve this aim.
First, the use of ion deflection plates in front of rf-plasma sources might have a significant influence upon reducing point defects induced by these ions. An external magnet deflects a part of these ions. Unfortunately, such external magnetic field does not prevent all ions from impinging on the sample because it is infeasible to mount the magnet close to the plasma source aperture where the ion deflection effect is most significant. Moreover, there is an interaction between the external magnetic field and the electromagnetic wave coupled into the microwave cavity. This interaction is detrimental to the plasma source functionality. Deflection plates, on the contrary, solve both problems. They are mounted in front of the aperture, thus causing the most significant impact upon deflecting the ions. The deflection plates are also far away from the plasma source. So the interaction between deflection plates and plasma source is low, causing no adverse effect upon the plasma source functionality.

Second, further studies on a thermal treatment of Ga(As,N) and (In,Ga)(As,N) may result in an improvement of the (In,Ga)(As,N) laser performance. Throughout this work, extensive studies regarding ex-situ annealing procedures on Ga(As,N) and (In,Ga)(As,N) have been accomplished. These RTA procedures have been carried out in a nitrogen atmosphere. Several authors report on a hydrogen-assisted passivation of point defects in Ga(As,N) and (In,Ga)(As,N)[129, 130]. Hence, performing RTA in a hydrogen atmosphere may lead to an improvement of the (In,Ga)(As,N) laser performance. In case of the (In,Ga)(As,N) lasers presented in this work, we have shown that there is an inevitable in-situ annealing effect, owing to the growth of the top (Al,Ga)As cladding layer. Thus, studies on the optimization of this in-situ annealing treatment might also help to enhance the performance of (In,Ga)(As,N) lasers.

Third, one may contemplate to harness the pentanary (In,Ga)(As,N,Sb) material system for realizing long wavelength infrared lasers. There is a strong degradation of (In,Ga)(As,N) laser features for emissions above 1.3 μm (i.e. for nitrogen concentrations above 2%). Instead of incorporating higher amounts of nitrogen, one may consider to incorporate antimony. The incorporation of antimony into (In,Ga)(As,N) results in a further band gap reduction. Thus, for accomplishing lasers emitting above 1.3 μm, one can partly compensate the nitrogen-induced band gap reduction by the incorporation of antimony. As a result, one may reduce the nitrogen concentration of (In,Ga)(As,N,Sb) lasers which may lead to a better laser performance. Solely a few studies about this issue have been accomplished[5, 74, 121, 122, 131, 132].

Fourth, a conceivable avenue to avoid ion-induced point defects is the use of gases as a nitrogen supply. These gases may be dimethylhydrazine[133, 134, 135] or ammonia[136] – most common in MOCVD systems. Even though Ga(As,N) and (In,Ga)(As,N) samples grown with these nitrogen sources show poor optical properties with respect to samples grown with the use of a rf-plasma source, these gases do not generate ions. The degradation of optical properties is attributed to a higher impurity concentration in these samples[10]. Still, if one can reduce the amount of impurities incorporated into Ga(As,N) and (In,Ga)(As,N), these gases may be an alternative nitrogen source for accomplishing (In,Ga)(As,N) infrared lasers.

Apart from laser applications, these material systems offer great possibilities to study questions of fundamental physics due to their unique properties. The change of the energy structure of GaAs and (In,Ga)As – induced by the incorporation of nitrogen – is not fully understood yet. There are several experimental observations related to this issue. As discussed in section 2.1, some of these experiments can be explained by the BAC model only, whereas other experiments can solely be elucidated by ab-initio calculations. Thus, a possible aim is to find a model that explains all experimental observations. This model may also be beneficial to understand the energy structure of other nitrogen-containing III-V semiconductors, such as Ga(P,N). Apart from that, point defects may also be a subject of study, as they are prevalent in these material systems. These defects may serve as a basis for fundamental research on properties of semiconductors, e.g. the electronic structure of point defects or RTA-induced processes that result in a healing out of these defects. Hence, Ga(As,N) and (In,Ga)(As,N) offer great potentials in two ways. First, these material systems allow to accomplish laser diodes in the important telecommunication wavelength range. Second, they also serve as a basis for fundamental research.

Bibliography

[1] Y. U. S. Sakai and Y. Terauchi, Jpn. J. Appl. Phys. **32**, 4413 (1993). 9

[2] M. Kondow, K. Uomi, A. Niwa, T. Kitatani, S. Watahiki, and Y. Yazawa, Jpn. J. Appl. Phys. **35**, 1273 (1996). 9

[3] M. Weyers, M. Sato, and H. Ando, Jpn. J. Appl. Phys. **31**, 853 (1992). 9, 33

[4] M. Kondow, S. Nakatsuka, T. Kitatani, Y. Yazawa, and M. Okai, Jpn. J. Appl. Phys. **35**, 5711 (1996). 9, 76

[5] M. A. Wistey, S. R. Bank, H. B. Yuen, L. L. Goddard, and J. S. Harris, J. Vac. Sci. Technol. B **22**, 1562 (2004). 9, 75, 76, 78

[6] M. Fischer, D. Gollub, M. Reinhard, M. Kamp, and A. Forchel, J. Cryst. Growth **251**, 353 (2003). 9, 75, 76

[7] A. Y. Egorov, D. Bernklau, D. Livshits, V. Ustinov, Z. I. Alferov, and H. Riechert, Electron. Lett. **35**, 1643 (1999). 9, 76

[8] W. Li, T. Jouhti, C. S. Peng, J. Konttinen, P. Laukkanen, E.-M. Pavelescu, M. Dumitrescu, and M. Pessa, Appl. Phys. Lett. **79**, 3386 (2001). 9, 76

[9] S. Kurtz, J. F. Geisz, B. M. Keyes, W. K. Metzger, D. J. Friedman, J. M. Olson, and A. J. Ptak, Appl. Phys. Lett. **82**, 2634 (2003). 10

[10] A. J. Ptak, S. W. Johnston, S. Kurtz, D. J. Friedman, and W. K. Metzger, J. Cryst. Growth **251**, 392 (2003). 10, 78

[11] X. Liu, M.-E. Pistol, L. Samuelson, S. Schwetlick, and W. Seifert, Appl. Phys. Lett. **56**, 1451 (1990). 10

[12] P. R. C. Kent and A. Zunger, Phys. Rev. Lett. **86**, 2613 (2001). 10

[13] F. Masia, A. Polimeni, G. B. H. von Högersthal, M. Bissiri, and M. Capizzi, Appl. Phys. Lett. **82**, 4474 (2003). 10

[14] C. Skierbiszewski, S. P. Łepowski, P. Perlin, T. Suski, W. Jantsch, and J. Geisz, Physica E **13**, 1078 (2002). 10, 13

[15] P. N. Hai, W. M. Chen, I. A. Buyanova, H. P. Xin, and C. W. Tu, Appl. Phys. Lett. **77**, 1843 (2000). 10

[16] I. Suemune, K. Uesugi, and W. Walukiewicz, Appl. Phys. Lett. **77**, 3021 (2000). 10, 13

[17] R. Chtourou, F. Bousbih, S. B. Bouzid, F. F. Charfi, J. C. Harmand, G. Ungaro, and L. Largeau, Appl. Phys. Lett. **80**, 2075 (2002). 10, 13, 33, 39

[18] K. Uesugi, I. Suemune, T. Hasegawa, T. Akutagawa, and T. Nakamura, Appl. Phys. Lett. **76**, 1285 (2000). 10

[19] W. Shan, W. Walukiewicz, J. W. Ager III, E. E. Haller, J. F. Geisz, D. J. Friedman, J. M. Olson, and S. R. Kurtz, Phys. Rev. Lett. **82**, 1221 (1999). 12, 33

[20] J. Wu, W. Shan, W. Walukiewicz, K. M. Yu, J. W. Ager III, E. E. Haller, H. P. Xin, and C. W. Tu, Phys. Rev. B **64**, 085320 (2001). 12

[21] W. Shan, W. Walukiewicz, J. W. Ager III, E. E. Haller, J. F. Geisz, D. J. Friedman, J. M. Olson, and S. R. Kurtz, J. Appl. Phys. **86**, 2349 (1999). 12

[22] F. Bousbih, S. B. Bouzid, R. Chtourou, F. F. Charfi, J. C. Harmand, and G. Ungaro, Mat. Sci. Eng. C **21**, 251 (2002). 12

[23] T. Mattila, S.-H. Wei, and A. Zunger, Phys. Rev. B **60**, 11245 (1999). 12

[24] P. R. C. Kent and A. Zunger, Phys. Rev. B **64**, 115208 (2001). 12

[25] S.-H. Wei and A. Zunger, Phys. Rev. Lett. **76**, 664 (1996). 12

[26] L.-W. Wang, Appl. Phys. Lett. **78**, 1565 (2001). 12

[27] L. Bellaiche, S.-H. Wei, and A. Zunger, Appl. Phys. Lett. **70**, 3558 (1997). 12

[28] C. Skierbiszewski, P. Perlin, P. Wiesniewski, W. Knap, T. Suski, W. Walukiewicz, W. Shan, K. M. Yu, Y. W. Ager III, E. E. Haller, J. F. Geisz, and J. M. Olson, Appl. Phys. Lett. **76**, 2409 (2000). 13, 33

[29] O. Brandt, Ph.D. thesis, Max-Planck-Institut für Festkörperforschung Stuttgart, 1991. 15

[30] C. Gourdon and P. Lavallard, phys. stat. sol. (b) **153**, 641 (1989). 15

[31] J. Singh, *Physics of Semiconductors and their Heterostructures* (McGraw-Hill, Inc., New York, 1993). 15

[32] S. G. Spruytte, C. W. Coldren, J. S. Harris, W. Wampler, P. Krispin, K. Ploog, and M. C. Larson, J. Appl. Phys. **89**, 4401 (2001). 17, 44

[33] S. G. Spruytte, M. C. Larson, W. Wampler, C. W. Coldren, H. E. Petersen, and J. S. Harris, J. Cryst. Growth **227-228**, 506 (2001). 17, 31, 39, 44

[34] W. Li, M. Pessa, and J. Likonen, Appl. Phys. Lett. **78**, 2864 (2001). 17

[35] K. Uesugi, N. Morooka, and I. Suemune, Appl. Phys. Lett. **74**, 1254 (1999). 17, 33

[36] *Properties of GaAs, Third Edition*, edited by M. R. Brozel and G. E. Stillman (EMIS Datareview INSPEC, London, 1996). 18, 23

[37] G. Bauer and W. Richter, *Optical Characterization of Epitaxial Semiconductor Layers* (Spinger Verlag, Berlin, 1996). 21

[38] O. Brandt, P. Waltereit, and K. H. Ploog, J. Phys. D **35**, 577 (2002). 21

[39] T. Van Buuren, M. K. Weilmeier, I. Athwal, K. M. Colbow, J. A. Mackenzie, T. Tiedje, P. C. Wong, and K. A. R. Mitchell, Appl. Phys. Lett. **59**, 465 (1991). 23

[40] I.-H. Ho and G. B. Stringfellow, J. Cryst. Growth **178**, 1 (1997). 25

[41] M. Adamcyk, S. Tixier, B. J. Ruck, J. H. Schmid, T. Tiedje, V. Fink, M. Jeffries, D. Karaiskaj, K. L. Kavanagh, and M. Thewalt, J. Vac. Sci. Technol. B **19**, 1417 (2001). 26, 38

[42] L. H. Li, Z. Pan, Y. W. Lin, X. Y. Wang, and R. H. Wu, J. Cryst. Growth **227-228**, 527 (2001). 26, 41

[43] P. Krispin, S. G. Spruytte, J. S. Harris, and K. H. Ploog, J. Appl. Phys. **88**, 4153 (2000). 28, 73

[44] G. Apostolopoulos, J. Herfort, W. Ulrici, L. Däweritz, and K. H. Ploog, Phys. Rev. B **60**, 5145 (1999). 28

[45] M. O. Manasreh, D. C. Look, K. R. Evans, and C. E. Stutz, Phys. Rev. B **41**, 10272 (1990). 28

[46] X. Liu, A. Prasad, J. Nishio, E. R. Weber, Z. Lilienthal-Weber, and W. Walukiewicz, Appl. Phys. Lett. **67**, 279 (1995). 28

[47] Z. Pan, L. Li, W. Zhang, X. Wang, Y. Lin, and R. Wu, J. Cryst. Growth **227-228**, 516 (2001). 31

[48] Z. Pan, L. H. Li, W. Zhang, Y. W. Lin, and R. H. Wu, Appl. Phys. Lett. **77**, 214 (2000). 31

[49] S. Zhongzhe, Y. S. Fatt, Y.-K. Chuin, L. W. Khai, F. Weijun, W. Shanzhong, and N. T. Khee, J. Appl. Phys. **94**, 1069 (2003). 31

[50] T. Kitatani, M. Kondow, K. Nakahara, M. C. Larson, Y. Yazawa, M. Okai, and K. Uomi, J. Cryst. Growth **201-202**, 351 (1999). 31

[51] S. Govindaraju and A. Holmes, Jr, J. Vac. Sci. Technol. B **20**, 1167 (2002). 31

[52] P. Gilet, L. G. P. Duvaut, P. Ballet, G. Rolland, C. Vannuffel, and A. Million, J. Vac. Sci. Technol. B **19**, 1422 (2001). 31, 39

[53] Z. Pan, L. H. Li, Z. Q. Zhou, W. Zhang, Y. T. Wang, and R. H. Wu, J. Cryst. Growth **209**, 648 (2000). 31

[54] R. Bhat, C. Caneau, L. Salamanca-Riba, W. Bi, and C. Tu, J. Cryst. Growth **195**, 427 (1998). 33

[55] B. M. Keyes, J. F. Geisz, P. C. Dippo, R. Reedy, C. Kramer, D. J. Friedman, S. R. Kurtz, and J. M. Olson, AIP Proceedings of the 15th Conference **462**, 511 (1999). 33

[56] M. Kondow, K. Uomi, K. Hosomi, and T. Mozume, Jpn. J. Appl. Phys. **33**, 1056 (1994). 33

[57] L. Malikova, F. H. Pollak, and R. Bhat, J. Electron. Mat. **27**, 484 (1998). 33

[58] J. W. Matthews and A. E. Blakeslee, J. Cryst. Growth **27**, 118 (1974). 35, 36

[59] N. Piffault, E. Gil, J. Leymarie, C. Monier, S. A. Clark, M. Anderson, R. Cadoret, V. Vasson, and A. M. Vasson, J. Cryst. Growth **135**, 11 (1994). 36

[60] S. F. Yoon, H. M. Li, K. Radhadkrishnan, and Z. Y. Han, J. Cryst. Growth **134**, 240 (1993). 36

[61] S. A. Clark, J. E. Macdonald, D. I. Westwood, and R. H. Williams, J. Cryst. Growth **121**, 743 (1992). 36

[62] I. Suemune, N. Morooka, K. Uesugi, Y.-W. Ok, and T.-Y. Seong, J. Cryst. Growth **221**, 546 (2000). 38

[63] I. Suemune, K. Uesugi, and T.-Y. Seong, Semicond. Si. Technol. **17**, 755 (2002). 38

[64] M. Adamcyk, J. H. Schmid, and T. Tiedje, Appl. Phys. Lett. **80**, 4357 (2002). 38

[65] M. Albrecht, V. Grillo, T. Remmele, H. P. Strunk, A. Y. Egorov, G. Dumitras, H. Riechert, A. Kaschner, R. Heitz, and A. Hoffmann, Appl. Phys. Lett. **81**, 2719 (2002). 39

[66] P. Gilet, A. Chenevas-Paule, P. Duvaut, L. Grenouillet, P. Holliger, A. Million, G. Rolland, and C. Vannuffel, phys. stat. sol (a) **176**, 279 (1999). 39

[67] P. J. Klar, H. Grünning, J. Koch, S. Schäfer, K. Volz, W. Stolz, W. Heimbrodt, A. M. K. Saadi, A. Lindsay, and E. P. O'Reilly, Phys. Rev. B **64**, 121203 (2001). 39

[68] L. Grenouillet, C. Bru-Chevallier, G. Guillot, P. Gilet, P. Duvaut, C. Vannuffel, A. Million, and A. Chenevas-Paule, Appl. Phys. Lett. **76**, 2241 (2000). 39, 62

[69] R. A. Mair, J. Y. Lin, H. X. Jiang, E. D. Jones, A. A. Allerman, and S. R. Kurtz, Appl. Phys. Lett. **76**, 188 (2000). 39

[70] E.-M. Pavelescu, T. Jouhti, C. S. Peng, W. Li, J. Konttinen, M. Dumitrescu, P. Laukkanen, and M. Pessa, J. Cryst. Growth **241**, 31 (2002). 39, 73

[71] E. Tournié, M.-A. Pinault, M. Laügt, J.-M. Chauveau, A. Trampert, and K. H. Ploog, Appl. Phys. Lett. **82**, 1845 (2003). 39

[72] J. Toivonen, T. Tuomi, J. Riikonen, L. Knuuttila, T. Hakkarainen, M. Sopanen, H. Lipsanen, P. J. Mcnally, W. Chen, and D. Lowney, Journal of Material Science: Materials in Electronics **14**, 267 (2003). 39

[73] E. Tournié, M.-A. Pinault, and A. Guzmán, Appl. Phys. Lett. **80**, 4148 (2002). 39, 57

[74] S. Bank, W. Ha, V. Gambin, M. Wistey, H. Yuen, L. Goddard, S. Kim, and J. S. Harris, J. Cryst. Growth **251**, 367 (2003). 39, 75, 76, 78

[75] V. Gambin, V. Lordi, W. Ha, M. Wistey, T. Takizawa, K. Uno, S. Friedrich, and J. Harris, J. Cryst. Growth **251**, 408 (2003). 39

[76] S. R. Kurtz, J. F. Klem, A. A. Allerman, R. M. Sieg, C. H. Seager, and E. D. Jones, Appl. Phys. Lett. **80**, 1379 (2002). 39

[77] D. Jiang, X. Liang, B. Sun, L. Bian, L. Li, Z. Pan, and R. Wu, phys. stat. sol. (c) **1**, 382 (2002). 39

[78] S. Shirakata, M. Kondow, and T. Kitatani, Appl. Phys. Lett. **80**, 2087 (2002). 39

[79] H. D. Sun, R. Macaluso, M. D. Dawson, F. Robert, A. C. Bryce, J. H. Marsh, P. Gilet, L. Grenouillet, A. Million, K. B. Nam, J. Y. Lin, and H. X. Jiang, J. Appl. Phys. **94**, 7581 (2003). 39

[80] R. Kudrawiec, G. Sęk, J. Misiewicz, D. Gollub, and A. Forchel, Appl. Phys. Lett. **83**, 2772 (2003). 39

[81] H. P. Xin, K. L. Kavanagh, and C. W. Tu, J. Cryst. Growth **208**, 145 (2000). 39

[82] X. D. Luo, P. H. Tan, Z. Y. Xu, and W. K. Ge, J. Appl. Phys. **94**, 4863 (2003). 39

[83] T. K. Ng, S. F. Yoon, W. J. Fan, W. K. Loke, S. Z. Wang, and S. T. Ng, J. Vac. Sci. Technol. B **21**, 2324 (2003). 39

[84] J. Toivonen, T. Hakkarainen, M. Sopanen, and H. Lipsanen, J. Cryst. Growth **221**, 456 (2000). 39

[85] A. Moto, S. Tanaka, N. Ikoma, T. Tanabe, S. Takagishi, M. Takahashi, and T. Katsuyama, Jpn. J. Appl. Phys. **38**, 1015 (1999). 39

[86] L. H. Li, Z. Pan, Y. W. Lin, X. Y. Wang, R. H. Wu, and W. K. We, J. Cryst. Growth **223**, 140 (2001). 41

[87] J. Miguel-Sánchez, A. Guzmán, and E. Muñoz, Appl. Phys. Lett. **85**, 1940 (2004). 41

[88] Z. Pan, L. H. Li, W. Zhang, Y. W. Lin, and R. H. Wu, Appl. Phys. Lett. **77**, 1280 (2000). 41

[89] H. Carrère, A. Arnoult, A. Ricard, and E. Bedel-Pereira, J. Cryst. Growth **243**, 295 (2002). 42

[90] T. Achtnich, G. Burri, M. A. Py, and M. Ilegems, Appl. Phys. Lett. **50**, 1730 (1987). 43

[91] R. A. Stall, R. J. Wunder, and V. Swaminathan, Appl. Phys. Lett. **47**, 519 (1985). 43

[92] N. Chand, A. S. Jordan, and S. N. G. Chu, Appl. Phys. Lett. **59**, 3270 (1991). 43

[93] W. T. Tsang, Appl. Phys. Lett. **33**, 245 (1978). 43

[94] M. Ramsteiner, D. S. Jiang, J. S. Harris, and K. H. Ploog, Appl. Phys. Lett. **84**, 1859 (2004). 43

[95] J. Toivonen, T. Hakkarainen, M. Sopanen, H. Lipsanen, J. Oila, and K. Saarinen, Appl. Phys. Lett. **82**, 40 (2003). 44

[96] T. Ahlgren, E. Vainonen-Ahlgren, J. Likonen, W. Li, and M. Pessa, Appl. Phys. Lett. **80**, 2314 (2002). 44

[97] P. Krispin, S. G. Spruytte, J. S. Harris, and K. H. Ploog, Appl. Phys. Lett. **80**, 2120 (2002). 44

[98] P. Krispin, V. Gambin, J. S. Harris, and K. H. Ploog, J. Appl. Phys. **93**, 6095 (2003). 44

[99] E. G. Bithell and W. M. Stobbs, Philos. Mag. A **60**, 39 (1989). 45

[100] K. Matsuda, T. Saiki, M. Takahashi, A. Moto, and S. Takagishi, Appl. Phys. Lett. **78**, 1508 (2001). 49

[101] A. M. Mintairov, T. H. Kosel, J. L. Merz, P. A. Blagnov, A. S. Vlasov, V. M. Ustinov, and R. E. Cook, Phys. Rev. B **87**, 277401 (2001). 49, 52

[102] A. M. Mintairov, P. A. Blagnov, J. L. Merz, V. M. Ustinov, A. S. Vlasov, A. R. Kovsh, J. S. Wang, L. Wei, and J. Y. Chi, Physica E **21**, 385 (2004). 49, 52

[103] Y. P. Varshni, Physica **34**, 149 (1967). 50

[104] J.-M. Chauveau, A. Trampert, K. H. Ploog, M.-A. Pinault, and E. Tournié, Appl. Phys. Lett. **82**, 3451 (2003). 57

[105] D. González, G. Arágon, D. Araújo, and R. García, Appl. Phys. Lett. **76**, 3236 (2000). 58

[106] *Semiconductors – Basic Data*, edited by O. Madelung (Springer Verlag, Berlin, 1996). 61

[107] R. Colombelli, V. Piazza, A. Badolato, M. Lazzarino, F. Beltram, W. Schoenfeld, and P. Petroff, Appl. Phys. Lett. **76**, 1146 (2000). 61

[108] E. Tournié, M.-A. Pinault, S. Vézian, J. Massies, and O. Tottereau, Appl. Phys. Lett. **77**, 2189 (2000). 62

[109] C. S. Peng, E.-M. Pavelescu, T. Jouhti, J. Konttinen, I. M. Fodchuk, Y. Kyslovsky, and M. Pessa, Appl. Phys. Lett. **80**, 4720 (2002). 64

[110] W. M. Li, R. M. Cohen, D. S. Simons, and P. H. Chi, Appl. Phys. Lett. **70**, 3392 (1997). 66

[111] B. Elman, E. S. Koteles, P. Melman, K. Ostreicher, and C. Sung, J. Appl. Phys. **70**, 2634 (1991). 72

[112] M. Wassermeier, R. Hey, M. Höricke, and E. Wiebicke, Semicond. Sci. Technol. **16**, 40 (2001). 72

[113] N. Tansu and L. J. Mawst, IEEE Photon. Technol. Lett. **13**, 179 (2001). 72

[114] W. J. Choi, P. D. Dapkus, and J. J. Jewell, IEEE Photon. Technol. Lett. **11**, 1572 (1999). 72

[115] F. Bugge, U. Zeimer, S. Gramlich, I. Rechenberg, J. Sebastian, G. Ebert, and M. Weyers, J. Cryst. Growth **221**, 496 (2000). 72

[116] S. Mogg, N. Chitica, R. Schatz, and M. Hammar, Appl. Phys. Lett. **81**, 2334 (2002). 72

[117] T. Takeuchi, Y.-L. Chang, A. Tandon, D. Bour, S. Corzine, R. Twist, M. Tan, and H.-C. Luan, Appl. Phys. Lett. **80**, 2445 (2002). 72

[118] F. Bugge, G. Ebert, J. Fricke, S. Gramlich, R. Staske, H. Wenzel, U. Zeimer, and M. Weyers, Appl. Phys. Lett. **79**, 1965 (2001). 72

[119] S. Sato and S. Satoh, Jpn. J. Appl. Phys. **38**, 990 (1999). 72

[120] T. Miyamoto, K. Takeuchi, and F. Koyoma, IEEE Photon. Technol. Lett. **9**, 1448 (1997). 73

[121] X. Yang, J. B. Heroux, M. J. Jurkovic, and W. I. Wang, Appl. Phys. Lett. **76**, 795 (2000). 75, 76, 78

[122] X. Yang, J. B. Heroux, M. J. Jurkovic, and W. I. Wang, IEEE Photon. Technol. Lett. **12**, 128 (2000). 75, 76, 78

[123] K. D. Choquette, J. F. Klem, A. J. Fischer, O. Blum, A. A. Allerman, I. J. Fritz, S. R. Kurtz, W. G. Breiland, R. Sieg, K. M. Geib, J. W. Scott, and R. L. Naone, Electron. Lett. **36**, 16 (2000). 76

[124] D. Gollub, M. Fischer, M. Kamp, and A. Forchel, Appl. Phys. Lett. **81**, 4330 (2002). 76

[125] T. Kitatani, K. Nakahara, M. Kondow, K. Uomi, and T. Tanaka, Jpn. J. Appl. Phys. **39**, 86 (2000). 76

[126] M. Kondow, T. Kitatani, K. Nakahara, and T. Tanaka, Jpn. J. Appl. Phys. **38**, 1355 (1999). 76

[127] D. E. Mars, D. I. Babic, Y. Kaneko, Y.-L. Chang, S. Subramamanya, J. Kruger, P. Perlin, and E. R. Weber, J. Vac. Sci. Technol. B **17**, 1272 (1999). 76

[128] N. Tansu, J.-Y. Yeh, and L. J. Mawst, Appl. Phys. Lett. **83**, 2512 (2003). 76

[129] I. A. Buyanova, M. Izadifard, W. M. Chen, A. Polimeni, M. Caipizzi, H. P. Xin, and C. W. Tu, Appl. Phys. Lett. **82**, 3662 (2003). 78

[130] L. Geelhaar, M. Galluppi, G. Jaschke, R. Averbeck, H. Riechert, T. Remmele, M. Albrecht, and H. P. Strunk, Proceedings of the 2004 International Conference on Molecular Beam Epitaxy, to be published in Journal of Crystal Growth. 78

[131] J. C. Harmand, G. Ungaro, L. Largeau, and G. Le Roux, Appl. Phys. Lett. **77**, 2482 (2000). 78

[132] K. Volz, V. Gambin, W. Ha, M. A. Wistey, H. Yuen, S. Bank, and J. S. Harris, J. Cryst. Growth **251**, 360 (2003). 78

[133] T. Miyamoto, S. Sato, Z. Pan, D. Schlenker, F. Koyama, and K. Iga, J. Cryst. Growth **195**, 421 (1998). 78

[134] F. Höhnsdorf, J. Koch, C. Agert, and W. Stolz, J. Cryst. Growth **195**, 391 (1998). 78

[135] S. Sato and S. Satoh, J. Cryst. Growth **192**, 381 (1998). 78

[136] T. Takahashi, Y. Tomomura, H. Ikeda, and H. Kawanishi, Appl. Phys. Lett. **78**, 1364 (2001). 78

Danksagung

Es bereitet mir große Freude, auf den letzten Seiten dieser Arbeit all denen zu danken, die mich bei der Erstellung meiner Dissertation unterstützt haben. Insbesondere bedanke ich mich bei ...

... Prof. Dr. Klaus H. Ploog, weil er mir die Möglichkeit gab, diese Dissertation am Paul-Drude-Institut anzufertigen. Prof. Ploog war stets am Thema der Dissertation interessiert und hat durch seine fachliche und moralische Unterstützung sehr zum Gelingen dieser Arbeit beigetragen.

... Dr. Lutz Däweritz, der als mein Betreuer durch sein gründliches Hinterfragen vieler Details zur Verbesserung dieser Arbeit beigetragen hat. Seine Bereitschaft zum Korrekturlesen, sowie zur finanziellen Unterstützung mehrerer Konferenzreisen und Forschungsvorhaben war ein wesentlicher Faktor für das Gelingen dieser Dissertation.

... Karin Hagenstein und Hans-Peter Schönherr für die technische Unterstützung und die Wartung der MBE-Anlage. Durch ihre umgängliche Art haben beide für ein positives Klima gesorgt, in dem ich gern gearbeitet habe.

... Dr. Rudolf Hey und Dr. Oliver Brandt für die ergiebigen wissenschaftlichen Diskussionen, die ich mit ihnen führen durfte. Beide haben durch ihr kritisches Korrekturlesen einen wichtigen Beitrag zur Verbesserung der Dissertation geleistet. Bei Oliver bedanke ich mich außerdem für die Hilfe bei Computerproblemen und Tipps bezüglich $\LaTeX$.

... Edith Wiebicke und Dr. Helmar Kostial für ihr unermüdliches Engagement beim Kontaktieren der Laserstrukturen.

... Dr. Manfred Ramsteiner und Dr. Lutz Schrottke für die Hilfe bei den unzähligen PL-, μPL- und Raman-Messungen.

... Dr. Achim Trampert, Jingli Chen und Dr. Jean-Michel Chauveau für die TEM-Aufnahmen und Diskussionen bezüglich der Defekte.

... Prof. Dr. De-Sheng Jiang und Prof. Dr. James Merz für ergiebige Diskussionen während ihrer Forschungsaufenthalte am Paul-Drude-Institut.

... Ilka Schuster für die Hilfe beim Ausdrucken diverser Poster und Folien für Konferenzen.

... Gerd Paris für die Wartung der PL-Anlage, sowie für die Unterstützung bei technischen Problemen bezüglich des Lasermessplatz.

... Dr. Matthias Wassermeier für den zweimonatigen Schnellkurs zum Bedienen der MBE-Anlage und zum Beherrschen diverser Charakterisierungsmethoden.

... Dr. Bernd Jenichen für die Hilfe beim Erstellen von RSM-Karten.

... Dr. Jens W. Tomm, Dr. Vadim Talalaev und Viktor Malyarchuk für die TR-PL und SNOM-Messungen am Max-Born-Institut, sowie wertvollen Diskussionen.

... Tommy Ive, Pranob Misra, Yue-Jun Sun und allen anderen Doktoranden, mit denen ich eine schöne Zeit innerhalb und außerhalb des Instituts verbringen durfte.

Lebenslauf

Gregor Mußler, geboren am 18. Oktober 1974 in Berlin

1981 – 1990: Besuch der Polytechnischen Oberschule in Berlin-Wilhelmshagen
1990 – 1995: Besuch des Gymnasiums in Berlin-Friedrichshagen
1995 – 1996: Zivildienst
1996 – 2001: Physikstudium an der Humboldt-Universität zu Berlin
2000 – 2001: Diplomarbeit am Lehrstuhl von Prof. Dr. Ted W. Masselink über Indiumphosphid-Quantenpunkte in einer Galliumphosphid-Matrix
2002 – 2005: Anfertigung dieser Dissertation am Paul-Drude-Institut Berlin

Selbstständigkeitserklärung

Hiermit erkläre ich, die vorliegende Dissertation *„Growth and Characterization of Ga(As,N) and (In,Ga)(As,N)"* selbstständig und ohne unerlaubte Hilfe angefertigt zu haben.

Ich habe mich anderwärts nicht um einen Doktorgrad beworben und besitze einen entsprechenden Doktorgrad nicht.

Ich erkläre die Kenntnisnahme der dem Verfahren zugrunde liegenden Promotionsordnung der Mathematisch-Naturwissenschaftlichen Fakultät I der Humboldt-Universität zu Berlin.

Gregor Mußler